UNIVERSITY OF SILESIA IN KATOWICE

FACULTY OF NATURAL SCIENCES

INSTITUTE OF BIOLOGY, BIOTECHNOLOGY

AND ENVIRONMENTAL PROTECTION

JOANNA NINA SKRZYDEŁ

DOCTORAL DISSERTATION

DYNAMICS OF COMPOSITION AND STRUCTURE OF ARABIDOPSIS THALIANA CELL WALLS IN SEPAL EPIDERMIS

THESIS SUPERVISORS:

Prof. dr. hab. Dorota Kwiatkowska
University of Silesia in Katowice

Dr. hab. Roman Wrzalik, prof. UŚ
University of Silesia in Katowice

Katowice 2025

Keywords: *Arabidopsis thaliana*, sepal epidermis, primary cell wall, cell wall composition, structural anisotropy, cuticular pattern formation, cell wall growth, cell surface geometry, Raman spectroscopy, *in vivo* Confocal Laser Scanning Microscopy

This work was supported by the research grant ERA-CAPS *"Unravelling how the mechanical regulation of local variability shapes reproducible plant organs"* (grant no. UMO-2017/24/Z/NZ3/00548) from the National Science Centre, Poland.

Podziękowania (Acknowledgements)

W sposób szczególny pragnę wyrazić moją głęboką wdzięczność
Pani Prof. dr hab. Dorocie Kwiatkowskiej *za opiekę naukową,*
nieocenioną pomoc, cenne uwagi merytoryczne oraz wsparcie,
bez którego powstanie niniejszej rozprawy byłoby niemożliwe.

Serdeczne podziękowania składam
Panu Prof. dr hab. Romanowi Wrzalikowi *za wszystkie sugestie,*
wsparcie merytoryczne oraz pomoc w przygotowaniu rozprawy.

Pragnę również podziękować mojej ***rodzinie*** *oraz* ***mężowi*** *za cierpliwość,*
wyrozumiałość, nieustające wsparcie i motywację
w trakcie powstawania niniejszej pracy.

Na koniec chciałabym podziękować wszystkim pracownikom oraz współpracownikom
Zespołu Biofizyki i Morfogenezy Roślin *Uniwersytetu Śląskiego w Katowicach za*
okazaną życzliwość, pomoc i inspirującą atmosferę pracy.

Contents:

1. INTRODUCTION

1.1 Structure and composition of primary cell wall

Protoplasts of plant cells are encapsulated in the cell wall. Thin and elastic walls of growing cells are called primary cell walls. Their composition and structure are not uniform and undergo constant modifications, which are crucial for development. After growth cessation the primary cell wall often changes due to incrustation, and new layers, called secondary cell wall, are deposited on the primary wall surface facing the protoplast. The secondary cell wall is thicker and stiffer than the primary wall, while its composition and structure are more stable in time to maintain the tissue stiffness and strength (Cosgrove and Jarvis 2012, Cosgrove 2022).

1.1.1 Components of primary cell wall

Primary cell walls are composed mainly of polysaccharides, like cellulose, pectins, and hemicelluloses, with only a small contribution of proteins. The polysaccharides account for 86% of the cell wall dry mass of *Arabidopsis thaliana* leaves (Zablackis et al. 1995). Structural proteins, immobilised within the wall, contribute approximately 5-10%, the remaining proteins include many enzymes (Lee et al. 2004).

Cellulose

One of the most important cell wall components, which plays a crucial role in the determination of mechanical properties of plant tissues, is cellulose (Cosgrove 2022). Cellulose has six polymorphic forms among which cellulose Iβ dominates in higher plants (Rongpipi et al. 2019). The cellulose chains, which consist of β-1,4-linked D-glucose units, are synthesised by large cellulose synthase complexes (CSCs) embedded in the plasma membrane **(Fig. 1.2A** and **B)**. Major elements of CSC are cellulose synthase glycosyltransferases (CESA). The CSC has six lobes, each containing three CESAs (a trimer), which form a hexagonal rosette-like structure (Juraniec and Gajda 2020, Allen et al. 2021). CESAs in Arabidopsis are encoded by 6 gene clusters (Juraniec and Gajda 2020). In Arabidopsis primary cell wall, cellulose is synthesised by CESA1, CESA3, and CESA6-like (**Fig. 1.2C**) (Juraniec and Gajda 2020). Multiple parallel β-

1,4-glucan chains are bundled in a 3 nm-wide microfibril (Cosgrove 2024A). The glucan chains can be highly ordered (crystalline) providing excellent mechanical stiffness in the secondary cell walls while in primary cell walls the chains are less ordered (Jarvis 2018). In primary cell walls, cellulose constitutes 14% of dry wall mass (Zablackis et al. 1995).

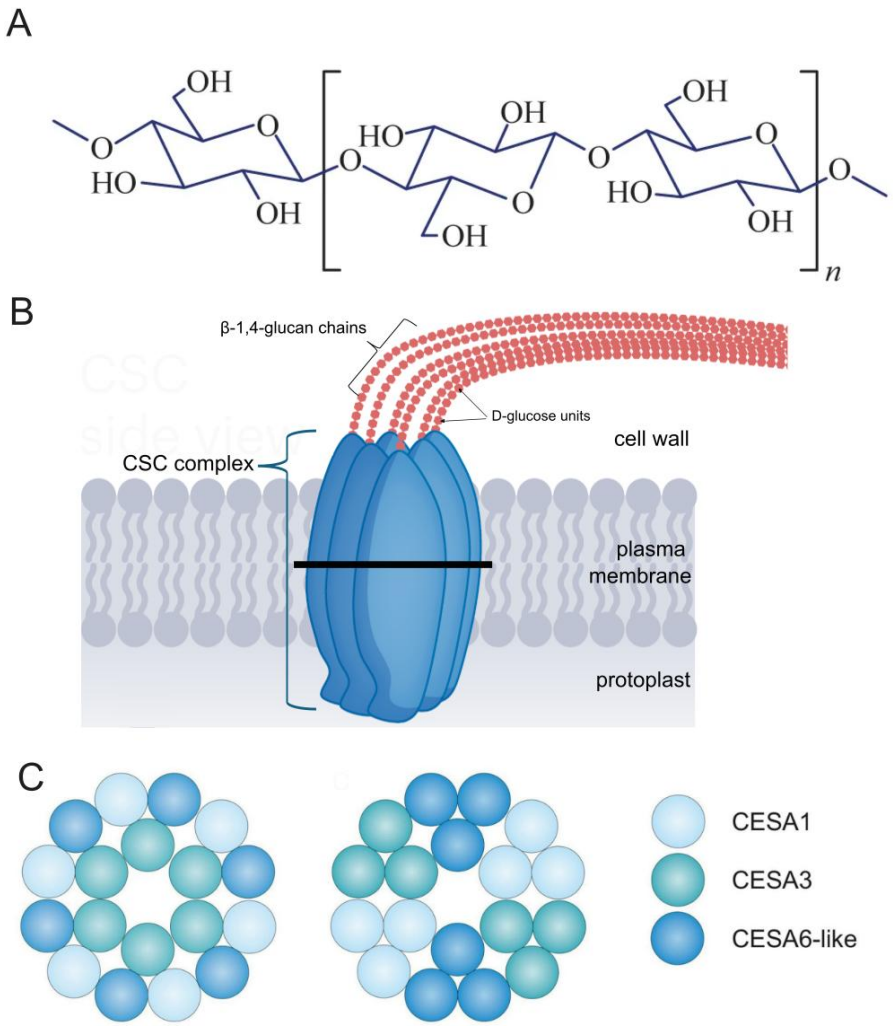

Fig. 1.1 Cellulose and its formation in the primary cell wall. (A) Fragment of a single cellulose chain composed of β-1,4-linked D-glucose monomers. (B) Scheme of CSC, embedded in the plasma membrane, with newly formed glucan chains. The black line marks cross-section of CSC presented in (C) that shows possible arrangements of CESA proteins (B: Cosgrove 2024, changed; C: Juraniec and Gajda 2020, changed).

Pectins

These polysaccharides are regarded as the most complex cell wall components (Carpita and Gibeaut 1993) creating a matrix in which cellulose microfibrils are embedded. Primary cell wall pectins constitute 35% of the wall dry mass (Zablackis et al. 1995). Within pectins three main groups are distinguished: the most abundant homogalacturonan (HG), rhamnogalacturonan-I (RGI), and the least abundant rhamnogalacturonan-II (RGII) (**Fig. 1.2**) (Zablackis et al. 1995, Ralet et al. 2005). Pectins belonging to all three groups are synthesised in Golgi apparatus and are composed mainly of α-1,4-linked D-galacturonic acid units (**Fig. 1.2A**) (Lund et al. 2020). HG, the major and the most abundant unbranched pectin is secreted into the cell wall in a fully methylesterified form. Once in the wall, HG can be deesterified at the C-6 carboxyl by cell wall enzymes called pectin methylesterases (PMEs) and/or acetylated at the O-2 or O-3 residues (**Fig. 1.2B**) (Sterling et al. 2001, Ralet et al. 2005, Mouille et al. 2007). This pectin is found in many cell wall types and during many developmental stages, most often in primary cell walls and the middle lamellae (Kaczmarska et al. 2022). RGI is composed of repeated units of galacturonic acid and rhamnose. RGI has numerous side chains, branched and/or unbranched, which are mainly linked to the O-4 rhamnose units, and contain neutral monosaccharide residues like arabinans (**Fig. 1.2C**, blue parentheses), galactans (**Fig. 1.2C**, red parentheses) and/or arabinogalactans (Yapo et al. 2007). RGII has a highly conserved structure with the same backbone as HG. However, unlike HG it has four complex side chains, containing more than ten different monosaccharide residues (**Fig. 1.2D)** (Kaczmarska et al. 2022). Due to the abundance of pectins in the middle lamellae they were initially considered to function primarily in the intercellular adhesion (Caffal and Mohnen 2009). However, it has been shown that they are involved in multiple processes including morphogenesis, intercellular communication and environmental sensing (Jonsson et al. 2021, Haas et al. 2020).

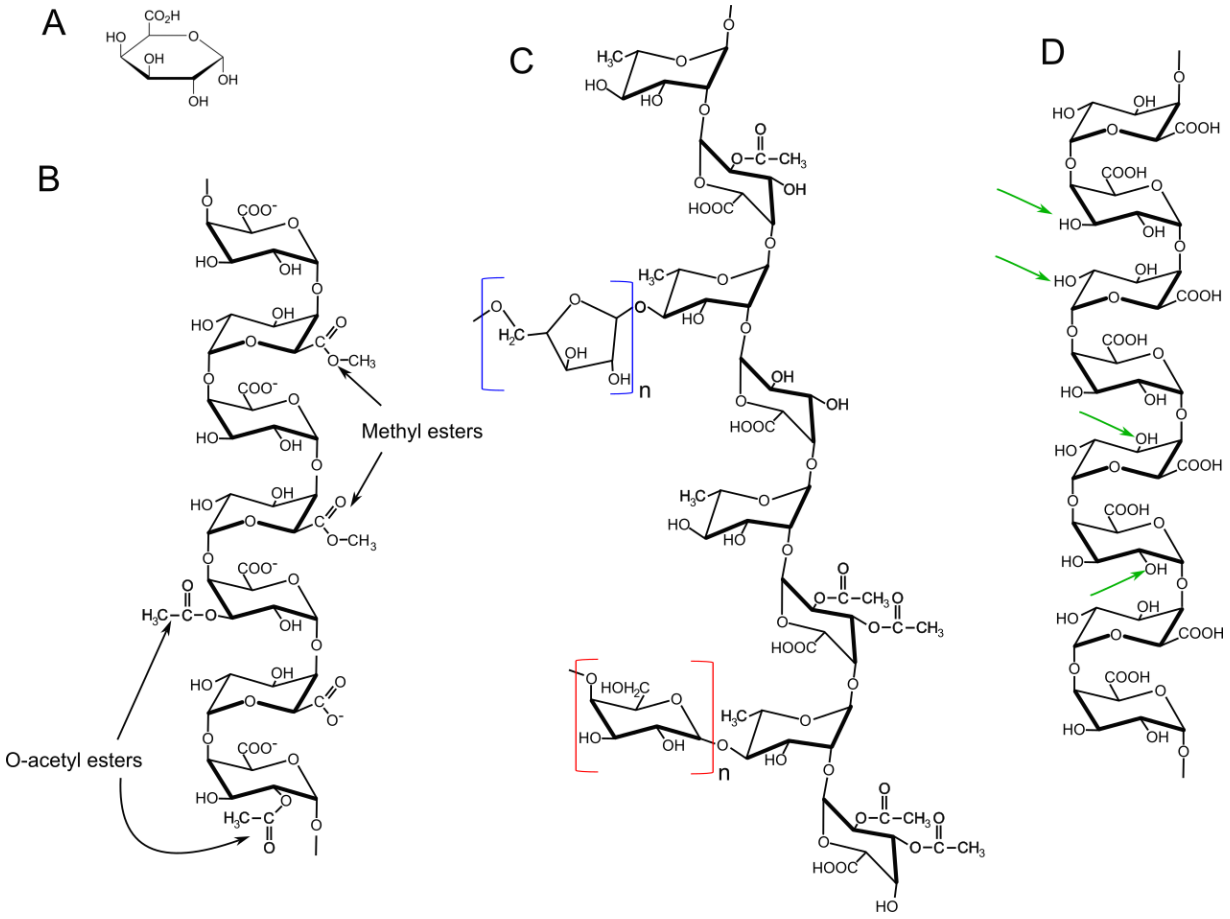

Fig. 1.2 Pectins constituting the primary cell wall: (**A**) galacturonic acid monomer, (**B**) HG with marked groups that undergo acetylation and methyl esterification, (**C**) RHI with main backbone of repeated disaccharide unit of α-(1,2)-D-galacturonic acid-α-(1,4)-L-rhamnose and possible residues like α-L-arabinose in blue and/or β-D-galactose in red, both red and blue residue can create long chains that are branched or unbranched, (**D**) RHII composed of galacturonic acid monomers, which can have different side chains in places pointed by green arrows (after Ochoa-Villarreal et al. 2012; changed).

Hemicelluloses

Hemicelluloses are a chemically heterogeneous group of polysaccharides, which can be built by several types of monosaccharides including xylose, mannose, galactose, and arabinose. Hemicelluloses are synthesised in Golgi apparatus and transported via vesicles toward the plasma membrane where vesicles are fused releasing their content to the cell wall (Bauer et al. 1973). The most common group of hemicelluloses of primary cell walls of land plants are xyloglucans (Cosgrove 2022). Xyloglucan (XyG) chain is built of β-1,4-linked glucosyl units decorated by various heterogeneous side

chains (Pieczywek et al. 2023). In many plants, the backbone of glucosyl residues is substituted with xylosyl residues (**Fig. 1.3**) (Zablackis et al. 1995). Hemicelluloses, such as XyG, associate with the surfaces of cellulose microfibrils and may influence microfibril organisation. While their branched structures could sterically hinder close packing of adjacent microfibrils, XyG does not act as direct tethers between microfibrils but rather exists in a minor, tightly bound fraction intertwined with cellulose (Park and Cosgrove 2012).

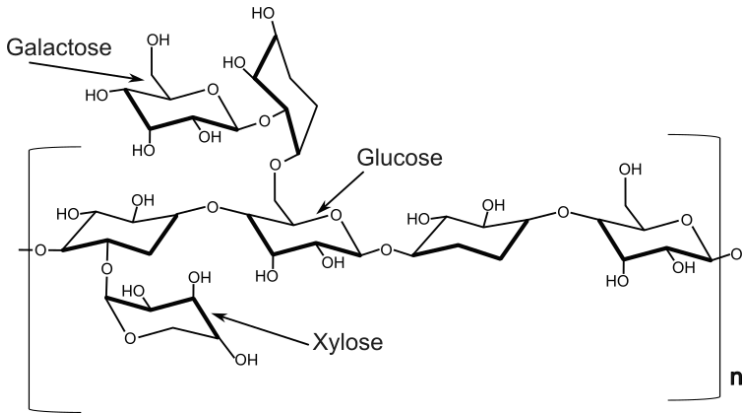

Fig. 1.3 Chemical structure of XyG.

Cell wall proteins

There is a variety of proteins in primary cell walls that contribute to the wall structure, participate in wall remodelling and growth. Structural proteins and enzymes are usually distinguished.

Structural proteins include (Showalter 2001, Cosgrove 2024A):

- extensins, which are hydroxyproline-rich glycoproteins that cross-link pectin and other cell wall polysaccharides reinforcing the cell wall,
- arabinogalactan proteins that interact with polysaccharides and affect the cell wall elasticity and extensibility,
- proline-rich proteins that contribute to mechanical strength by cross-linking the wall matrix polymers
- mannan-binding proteins which bind to mannan (hemicellulose) to help stabilise the wall matrix.

Cell wall enzymes include (Bethke et al. 2014, Wolf 2022, Cosgrove 2024A):

- xyloglucan endotransglucosylase/hydrolases which modify and/or degrade hemicelluloses and can be involved in the reaction to pathogen attack,
- pectin methylesterases (PMEs) which modify pectins by removing methyl groups thereby altering their physical properties.

The activity of PMEs is tightly regulated by pectin methylesterase inhibitors (PMEIs), non-enzymatic cell wall proteins that regulate activity of PMEs and influence formation of gel-like structure and mechanical properties of cell wall.

An important group of wall proteins that cannot be classified as either structural proteins or enzymes, are expansins. They play a crucial role by directly mediating cell wall loosening during growth: they disrupt non-covalent interactions between cellulose and hemicelluloses, enabling controlled wall extension (Cosgrove 2024B).

1.1.2 Structure of primary cell wall

Organisation of primary cell wall components and their interactions are crucial for expansion and mechanical properties of the walls. Cellulose microfibrils aggregate to 2D networks and create lamellae with specific microfibril orientations. For example, the primary cell wall of onion abaxial epidermis has lamellae with different microfibril orientation in each lamella (Cosgrove 2018, Natonik-Białoń et al. 2019, Nicolas et al. 2022). Moreover, cellulose microfibrils organisation is influenced by matrix polysaccharides like hemicellulose (Bauer et al. 1973, Cosgrove 2022). Hemicelluloses are connected with cellulose microfibrils via non-covalent interactions (hydrogen bonds) contributing to the cell wall mechanical strength while allowing it to be flexible.

Pectins, mainly HG, surround all other wall components and act as a matrix. It is documented that deesterified pectins are cross-linked by calcium, which strengthens cellulose-pectin and pectin-pectin contacts and leads to formation of an interconnected network where up to 50% of the cellulose fibril surface is in contact with pectins (Nicolas et al. 2022). Composition, methylation state, and calcium levels of pectins have been shown to change the mechanical properties of the wall by altering the level of cross-linking (Wang and Hong 2016, Phyo et al. 2018). Calcium ions promote the formation

of so-called egg-box structure and create supramolecular pectic gels (Bethke et al. 2014). Egg-box structure is a result of low degree of methylesterification of pectin or high degree of methylesterification accompanied by the unmethylesterifed (charged) regions (Williams 2020). For example, egg-box structure is formed by demethylated HG (C6 carboxyl group), which can create negatively charged groups and ionically interact with Ca^{2+} forming a stable gel (**Fig. 1.4**). However, recent investigations on Arabidopsis leaf epidermal peels and simulations of molecular dynamics revealed that HG within primary cell wall may be better represented by a zipper model (**Fig. 1.4B**) than egg-box model (**Fig. 1.4A**) (Obomighie et al. 2025). This may be a reason why in Arabidopsis, unlike other species, regions rich in deesterified HG are characterized by reduced stiffness, as demonstrated for the apical meristem (Peaucelle et al. 2011) and hypocotyls (Peaucelle et al. 2015).

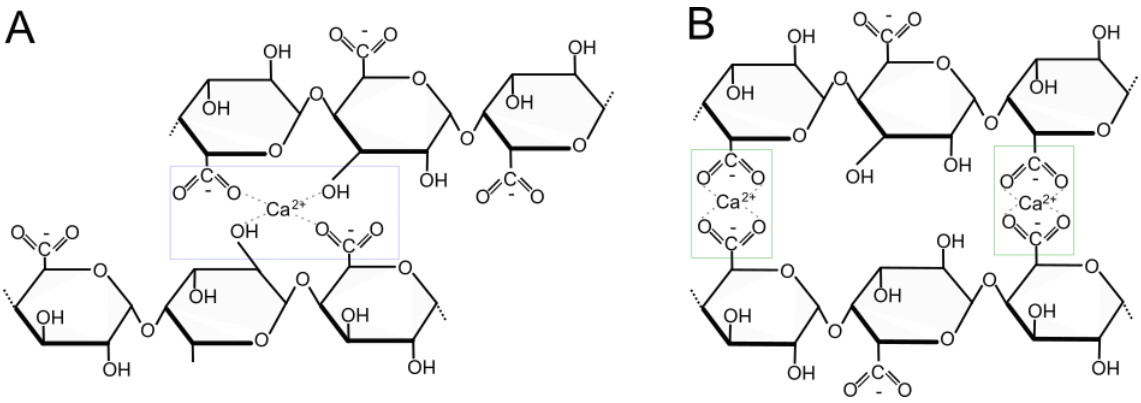

Fig. 1.4 Models of calcium crosslinking of HG: (**A**) the egg-box model, (**B**) zipper model. Rectangle outlines point to interactions between the carbonyl groups and Ca^{2+} (after Obomighie et al. 2025; changed).

Pectin molecules of different types interact with each other in the cell wall matrix, which can be controlled by availability of water in the cell wall environment. Highly branched RGI disables cross-linking of neighbouring HG chains within the cell walls because of steric hindrance, while less branched arabinose side chains in RGI facilitate interactions of neighbouring HGs in water deficient environment resulting in more gel-like cell wall matrix (**Fig. 1.5**) (Kaczmarska et al. 2022).

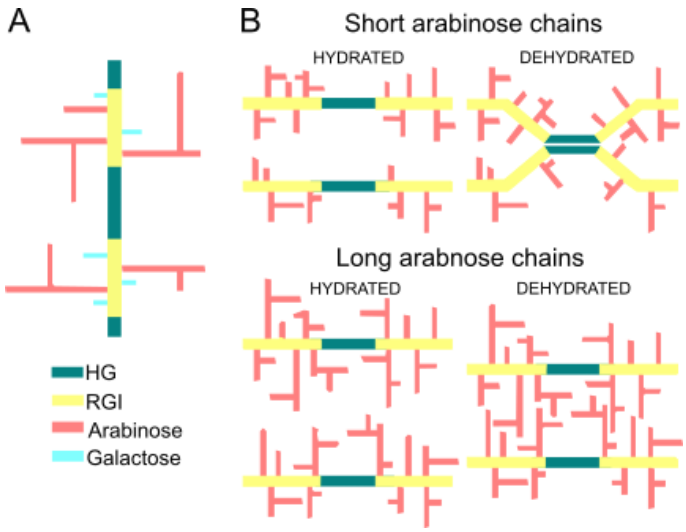

Fig. 1.5 Schematic representation of major models of HG and RGI linkage and interactions: (A) linear contiguous model of pectic polysaccharides; (B) hypothesised effect of the branching of arabinan side chains as a limiting factor in the HG binding process (Kaczmarska et al. 2022; changed).

1.1.3 Models of components organisation within primary cell walls

The previous sections outlined the main molecular components of the primary cell wall, including pectins (such as HG and RHI), cellulose, hemicelluloses like XyG, and structural proteins. While understanding their individual structures and interactions is essential, these details alone do not explain how the wall functions as a unified mechanical structure. To address this, various models have been proposed that integrate polymer organisation and crosslinking to explain the emergent physical behaviour of the wall during growth and morphogenesis.

Primary cell walls undergo continuous dynamic changes. Mutual interactions between wall polysaccharides have been the subject of research for many years and several models of the primary cell wall organisation have been developed (Pieczywek et al. 2023). These models are based mainly on interactions between cellulose-hemicellulose and cellulose-cellulose, and aim to explain how the primary cell wall maintains its integrity while allowing for cell growth.

The first model, proposed by Probine and Barber in 1966, described *Nitella* cell walls as a non-crystalline matrix of pectic substances supplemented by proteins and hemicelluloses and reinforced with cellulose microfibrils of a preferred orientation, which changes during the cell growth (Probine and Barber 1966). Cellulose microfibrils were regarded as organised in a multinet and bundled not directly with each other but

via hemicelluloses. Moreover, matrix polysaccharides, called non-cellulose components, were considered as partly immobilised and arranged in fibrils (Roelofsen 1958). Next concept, proposed by Keegstra et al. in 1973, assumed that the ends of XyG, the hemicellulose which coated cellulose, interacted covalently with pectic polysaccharides (RGI) (**Fig. 1.6A)**. Because of the lack of evidence of other important connections, such as extended XyG tethers spanning between adjacent cellulose microfibrils, this model was rejected. Further investigations led to formulation of a so-called multi-coat cell wall model, assuming that cellulose fibrils were covered by XyG (non-covalent interactions) and separated by layers of pectic polysaccharides (Talbott and Ray 1992) (**Fig. 1.6B**). This model was modified over the years and simplified to the model of tethered cellulose fibrils, which were separated from each other by XyG chains. Cellulose microfibrils, cross-linked into a load-bearing network, and XyG chains were regarded as the main components responsible for mechanical strength and integrity of the primary wall (Fry et al. 1992) and it was assumed that XyG backbone transmits tensile forces between microfibrils (Carpita and Gibiraut 1993) (**Fig. 1.6C**). According to this model cell wall growth requires cutting or shifting of XyG tethers (Fry et al. 1992).

Investigations on Arabidopsis double mutant *xxt1 xxt2* (*xyloglucan xylosyltransferases 1* and *2* code enzymes necessary for XyG synthesis) showed only weak phenotype of plants devoid of XyG. Park and Cosgrove (2012) tested tethered model of primary cell wall using this double mutant. Stretching tests performed on Arabidopsis petioles showed that *xxt1 xxt2* mutant cell walls were less stiff in comparison to wild type (Park and Cosgrove 2012) and revealed that lack of XyG resulted in an increase in cellulose microfibrils alignment and microfibril orientation nearly transverse to the long axis of the cell. This suggests that cellulose tethering is related more to cellulose organisation by itself than to XyG involvement in this process (Cosgrove 2022). Therefore, the existence of two independent polymer networks in the cell wall was proposed: cellulose–XyG network linked by hydrogen bonds, and pectins network with Ca^{2+} bridges. Investigations suggest that there is a communication between these two networks and that pectin linkage to XyG may play a role in the primary cell wall architecture. For example epicotyls of pea (*Pisum sativum* L.) exhibited links between galactan (one of the side chains of RGI) and XyG (Abdel-Masih et al. 2003). However, the amount of XyG-pectin complex was found to be very small (Park and Cosgrove 2015). Based on

this evidence the new model was conceived where cross-linking tethers between cellulose microfibrils and XyG are not so important for cell wall mechanics. Instead, XyG is located close to two adjacent cellulose fibrils that form a load bearing junctions called biomechanical hotspots. Such cellulose-cellulose interactions are attributed the crucial role in mechanical properties of the wall (Park and Cosgrove 2012, Cosgrove 2018) **(Fig 1.6D)**.

The most recent model of primary cell wall was proposed by Cosgrove in 2024 (**Fig. 1.6E**). It represents the three most abundant polysaccharides: cellulose, XyG and HG, by bead-and-spring models of polymers. The model shows the structure of a single cell wall lamella built of fully synthesised polymers that are arranged in a balanced low-energy configuration, i.e. in an equilibrium state. The cellulose microfibrils become bundled and form a cohesive network with XyG, which appears in different configurations: extended, coiled, or trapped between cellulose microfibrils in bundles, and tethers connecting cellulose microfibrils. Pectin in turn forms a soft network with extensive but weak contacts to cellulose and XyG (Cosgrove 2022, Cosgrove 2024A).

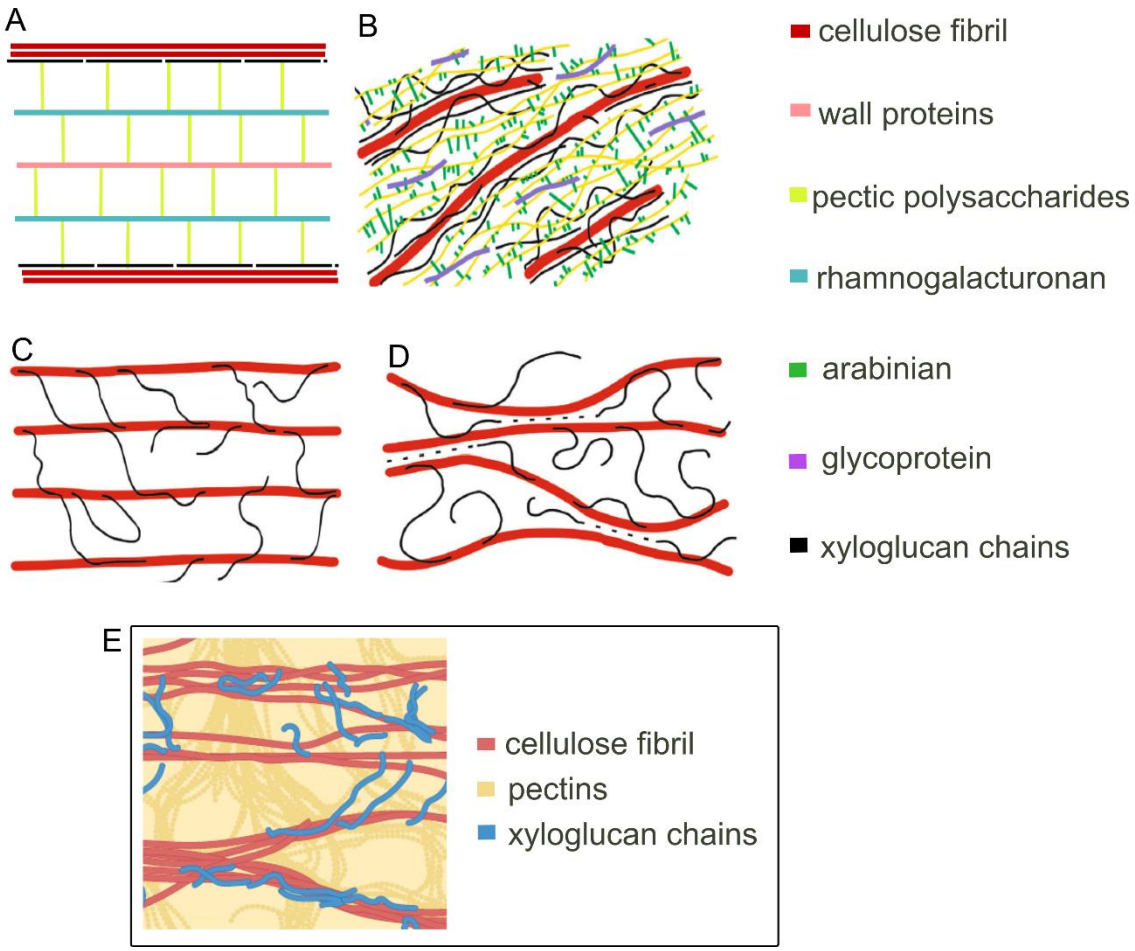

Fig. 1.6 Successive models of primary cell wall components organisation. (**A**) model proposed by Keestra et al. (1973) with covalently linked matrix and non-covalently linked cellulose microfibrils, (**B**) model proposed by Talbott and Ray in 1992, with cell wall represented as a multi-coat, (**C**) model proposed by Carpita and Gibeaut in 1993: tethered network of cellulose and hemicelluloses, (**D**) model proposed by Park and Cogrove in 2012: biochemical hotspots marked as black dotted lines, (**E**) the most recent model proposed by Cosgrove including interactions between the most abundant cell wall components (source of cell wall models: A-D: Pieczywek et al. 2023; changed, E: Cosgrove 2024A; changed).

1.1.4 Cell wall as a composite material

Composite material is made of two or more materials with different physical and chemical properties. Within the primary cell wall, both soft and stiff components can be distinguished, therefore the primary cell wall can be considered as a composite material (Vincent 1992). Pectins are soft cell wall components, which form a gel-like, viscous matrix that may contribute to cell wall stiffness during rapid deformation (Cosgrove 2016). Cellulose with glucan chains assembled into microfibrils provides tensile strength. Microfibrils are embedded in a matrix and create a composite structure where

cellulose microfibrils resist stretching forces, hemicelluloses such as XyG tether microfibrils while the surrounding matrix contributes to flexibility, porosity, and dynamic remodelling capacity during growth (Cosgrove and Jarvis 2012). The experiments on onion (*Allium sativum* L.) bulb scales and kalanchoe (*Kalanchoe blossfeldiana* Poelln.) leaves showed that the cellulose microfibrils orientation is crucial for mechanical properties of the cells (Kerstens et al. 2001). Mechanical tests on onion epidermis, which is composed of strongly elongated cells, revealed that stiffness of the sample is higher along the long cell axis, i.e. the direction along which cellulose microfibrils are aligned, as compared to the transverse direction. This indicates that the tissue is mechanically anisotropic. In contrast, when the same tests were performed for epidermis of kalanchoe leaves, where epidermal cells are not elongated and cellulose microfibrils are not aligned, similar stiffness values were obtained for directions parallel and perpendicular to the leaf midrib. These results show that the primary cell wall behaves as a composite material with a matrix and fibre phase, with anisotropic mechanical properties depending mainly on the fibre phase. The fibre phase is important to the reinforcement efficiency, however, the reinforcement is not only in one direction, because cell wall matrix, as well as cellulose, have a complex nature with many cross-links (Kerstens et al. 2001).

A similar composite behaviour is also observed during cell growth, when the orientation of cellulose microfibrils strongly influences the directionality and extent of cell wall expansion. Growing cells display anisotropic deformation when cellulose microfibrils are aligned, supporting the idea that the fibre-matrix architecture of the primary cell wall plays a key role not only in mechanics of mature tissue but also in regulation of growth patterns (Cosgrove 2018).

1.1.5 Expansins and expansion of primary cell walls

Growth of plant cells means the irreversible expansion of cell walls. It is driven primarily by turgor pressure, which stretches the cell wall when it is sufficiently loosened by enzymatic and biochemical modifications. The wall expansion is related to the wall capacity of the stress relaxation (loosening) (Cosgrove 1993) and is dynamically controlled (Cosgrove 2018). Change of apoplastic pH is involved in the wall loosening (Hager 2013). The pH of the cell wall is controlled by the plasma membrane proton

pomp H^+-ATPase, which is involved in cell wall acidification (Samalova et al. 2024). Expansins activity is pH dependent; they are the most active in acidic pH and their activity decreases in neutral pH, when cell wall loosening is more difficult and stretching is less easy (McQueen-Mason et al. 1992). Thus, acidification activates expansins, which disrupt non-covalent bonds between cellulose and surrounding components of cell wall matrix and selective sites where cellulose microfibrils make close contact with one another (Cosgrove 2015). This process relaxes cell wall stress and enables turgor-driven expansion (Cosgrove 2005, Park and Cosgrove 2012).

Effectiveness of cell wall loosening depends on the concentration and saturation of expansins within the cell wall. Experiments with the addition of exogenous expansins, limited by the rate of protein diffusion into the wall, show that cell wall loosening is progressing fast, peaks, then slows down and remains at a constant level (or slightly decreases) (Cosgrove 2024B). Expansins work only when the cell wall is in tension.

Expansins are coded by multiple genes (partially redundant) in plants, so interpretation of the single mutation and its phenotypic effect and complex expression patterns are difficult (Cosgrove 2024B). However, some genetic studies support the role of expansins in growth regulation. In Arabidopsis, for instance, loss of *AtEXP10* expression results in smaller leaves and shorter petioles, whereas overexpression promotes increased leaf size (Cho and Cosgrove 2000). Additional evidence highlights the broader influence of expansins on plant development. Although mutation of *AtEXPA15* was initially thought to lack phenotypic effects (Armezzani et al. 2018), later work showed that it impairs petal and fruit development (Bernal-Gallardo et al. 2024). Moreover, overexpression of expansins in Arabidopsis roots induced major transcriptomic changes, with over 600 genes altered within 3 hours (Samalova et al. 2023). This may be due to activation of wall integrity signalling pathways via receptor-like kinases that restrict growth upon detecting wall disturbances (Gigli-Bisceglia et al. 2020, Wolf 2022). Notably, such responses vary by tissue, possibly reflecting differences in the susceptibility of cell walls to expansin-induced disruption.

A recent conceptional model proposes that expansins slide along cellulose microfibrils, loosening their contacts progressively, and offers a distinct mechanism compared to the traditional viscoelastic matrix flow (**Fig. 1.7**) (Cosgrove 2024B). However, the precise

mechanism of expansins-dependent wall loosening remains unsolved and will require further development of both experimental and computational tools.

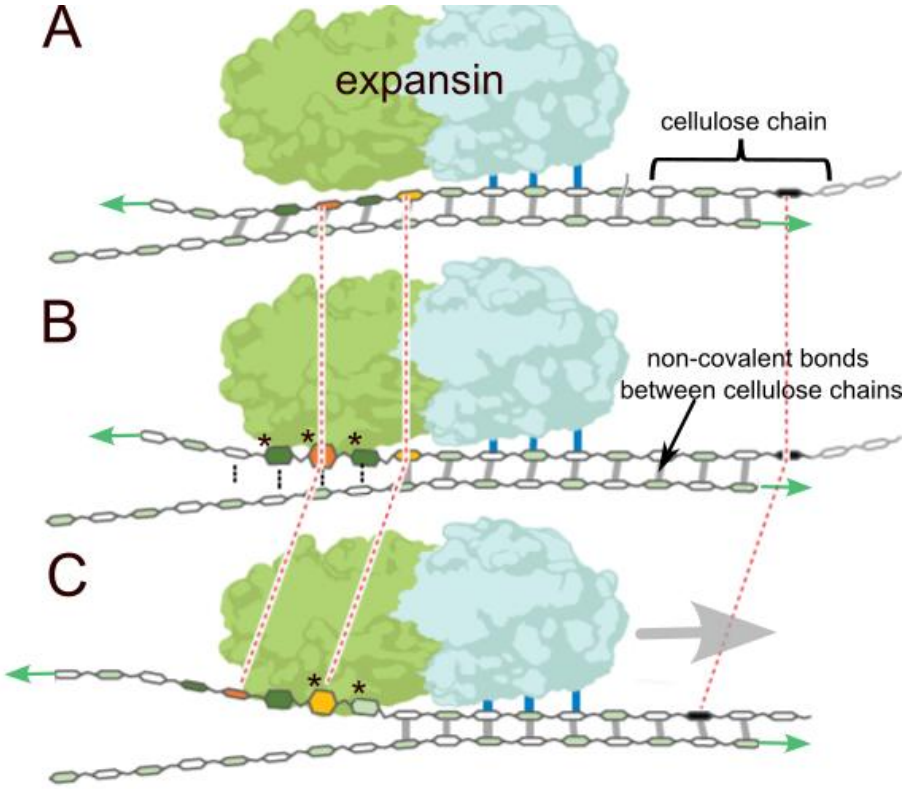

Fig. 1.7 Model of interactions between expansins and cellulose chains. (A) initial state, expansin is non covalently bound to cellulose chains in tension in the direction marked by green arrows, (B) expansin interacts with cellulose chain twisting glucose residues, (C) expansin slides along the cellulose chain and binds with new glucose residues (Cosgrove 2024B changed)

1.1.6 Cell wall mutants in investigations of primary cell wall mechanics and expansion

Mutations in genes involved in biosynthesis of cell wall components, regulation of the wall structure, or those encoding the apoplastic enzymes can significantly alter the content or arrangement of key wall components such as cellulose, hemicellulose, and pectins, leading to modification of mechanical properties of cell wall and developmental defects. Understanding these defects is crucial for elucidation how genetic variation shapes cell wall mechanics and impacts plant growth and development. The number of genes, which mutants have been identified as affecting the cell wall composition and

structure, is vast. Therefore, below the focus is on those genes that were chosen for the present analysis of how mutation affect the primary cell walls.

Pectins

The distribution of methyl groups within HG, the major pectin of primary cell wall, can affect the mechanical properties of cell wall. It is regulated by PMEs enzymes, the family of which in Arabidopsis consists of 66 members (Pelloux et al. 2007). Removal of methyl groups from HG, the main function of PMEs, results in free carboxyl groups with which the Ca^{2+} interacts to create a pectic gel (Wormit and Usadel 2018; see also Chapter **1.1.2 Structure of primary cell wall**). In accordance with this phenomenon, blockage of pectin demethylesterification in walls of Arabidopsis inflorescence shoot apex was shown to induce tissue softening (Braybrook and Peaucelle 2013). Another example is *pme35* mutation effect on inflorescence stems of Arabidopsis. The mutant has a rather weak phenotype but differs from Col-0 in mechanical properties. Bending and compression tests of the mutant and wild type stems showed that the same applied force caused bigger deformation in *pme35* than in Col-0, indicating that stiffness of mutant cell walls is decreased (Hongo et al. 2012). The reduced stiffness observed in *pme35*, which lacks demethylesterification and thus cannot form calcium cross-links, explains the softening effect.

Hemicelluloses

While pectins contribute to the flexibility of the cell wall by forming a gel-like matrix, hemicelluloses play a role in cross-linking of cellulose microfibrils, enhancing the structural integrity and providing a framework that accommodates controlled changes during growth. XyG and its metabolism play a crucial role in rapid cell elongation. Xylosyl residues from XyG oligosaccharides can be released by the apoplastic glycoside hydrolase (α-xylosidase) in the process known as XyG maturation (Günl and Pauly 2011). When the apoplastic glycoside hydrolase (α-xylosidase) is damaged in the *xyl1* mutant, the lack of enzyme activity is manifested in reduction of XyG content in hypocotyls. This has an indirect impact on pectin demethylesterification and contributes to softening of cell wall matrix (Sechet et al. 2016). However, mechanism of formation of XyG-pectin hybrid molecules within cell wall is unclear (Stratilová et al. 2020, Cosgrove 2022). The excess of xylose subunits in XyG leads to shorter siliques and reduced fitness of the mutant plants (Günl and Pauly 2011). In the Arabidopsis sepal

epidermis, changes in XyG structure may contribute to local variation in mechanical stiffness, influencing anisotropic growth patterns.

Cellulose

Cellulose microfibrils are the stiffest element of the primary cell wall (see chapter **1.1.1 Components of primary cell wall: Cellulose)**. Cortical microtubules guide CSC movement and thus the most recently deposited cellulose microfibrils are usually oriented parallel to the microtubules. If this guidance is affected the most recently deposited microfibrils are aligned and oriented in the same direction as the previous, i.e. earlier deposited layer (Baskin 2001). Mutation of the gene encoding Cellulose Synthase-Interacting 1 protein (CSI1), an important element of the CSC, disrupts the linkage between plasma membrane-located CESA proteins and cortical microtubules. It thus has an indirect impact on cellulose microfibrils arrangement in the primary cell wall and affects the shape and size of organs. The lack of CESA guidance by cortical microtubules leads to reduction in cell elongation and growth of hypocotyl, root and floral organs including sepals (Bringmann et al. 2012, Mollier et al. 2023). Organ size and morphology are also affected in *mad5* mutant (*microRNA action deficient 5*), which has smaller leaves and the whole plants than wild type. This mutation affects KATANIN, the microtubule-severing enzyme, crucial for orientation of cell division planes and for establishing cell growth anisotropy (Baskin 2001, Brodersen et al. 2008, Uyttewaal et al. 2012, Luptovčiak et al. 2017).

In many studies on cell wall mutants, the focus is on assessing the direct impact of the disrupted biosynthesis or structure of a cell wall component of interest on the mutant plant phenotype. However, it is important to elucidate what are the indirect mutation effects on other cell wall components, as the absence or modification of one component frequently does not lead to distinct phenotype. This may be due to a so-called compensatory mechanism involving other wall components, whose contributions are not always examined.

1.1.7 Raman spectroscopy in investigation of structure and composition of cell wall

To elucidate composition changes within the primary cell wall, multiple techniques have been applied over the years. One of the most effective techniques used to study structure and dynamics of biomolecules, including cell wall components, is Raman spectroscopy which combined with microscopy permits data acquisition with high spatial resolution (Borowska-Wykręt and Dulski 2019, Saletnik et al. 2021). Raman spectroscopy is a vibrational technique that does not utilise markers and is designed to measure the frequency shift of inelastic scattered light when a photon of incident light hits a particle and produces a scattered photon (Xu et al. 2018). As a result, a Raman spectrum is obtained that consists of bands where every functional group has a characteristic vibration frequency visualized in the form of a peak (Gierlinger and Schwanninger 2007).

Raman spectroscopy has often been used in investigations of secondary cell wall, especially of cellulose microfibrils organisation. For example, investigations on secondary xylem of spruce (*Picea abies* (L.) H.Karst.) branches allowed to determine the main orientation of the cellulose fibrils within the softwood and to predict orientation of the cellulose microfibrils in the newly formed secondary cell wall layer (Gierlinger et al. 2010). Investigations on the secondary cell wall demonstrated a strategy to measure microfibrils orientation within secondary cell walls of secondary xylem, where the intensity of the peaks related to cellulose changes with the applied polariser angle (Zhang and al. 2023).

Beyond its application in secondary wall studies, Raman imaging has also been used to assess the chemical architecture of the plant epidermis. In *Kalmia procumbens* (*Loiseleuria procumbens* (L.) Desv.), it revealed distinct cuticle layers enriched in cutin, triterpenoids, phenolics, alkanes, and cinnamic acids (Tiloca et al. 2025). This demonstrates Raman spectroscopy sensitivity to chemical and structural variation and highlights its potential for analysing primary cell walls, including epidermal walls and their cuticles at the interface with the environment. In the case of Arabidopsis, primary walls are relatively thin (from approximately 150 nm up to 500 nm of outer periclinal walls of epidermal cells) (Tolleter et al. 2024, Skrzydeł et al. 2021). Nevertheless, their remodelling, including interactions between cuticular and other wall components, could

be examined using Raman spectroscopy. Raman spectroscopy was already used for investigations on Arabidopsis stems and showed that tissues present chemical heterogeneity such as different aromatic components and carbohydrates (differences in hemicelluloses were detected) (Morel and Gierlinger 2023). However, possibility of examining all the components in individual primary cell walls has not been fully explored yet.

Raman spectroscopy has also been used to assess primary cell wall organisation at the subcellular level. In Arabidopsis sepals, it has been used to measure the orientation of cellulose microfibrils by detecting changes in signal depending on the polarisation plane, revealing how cellulose is organised within the cell wall of wild type and *csi1* mutant (Mollier et al. 2023). While other techniques were needed to link these patterns to tissue-level growth, the study showed that Raman is a valuable tool for local analysis of cell wall structure. It highlights the strength of Raman spectroscopy in visualising cellulose organisation with high spatial resolution and the importance of combining such data with mechanical and developmental studies to better understand coordinated anisotropic growth of epidermal cells.

1.2 Arabidopsis sepal as a model organ to study cell wall composition and its changes during development

Arabidopsis flower has been studied for decades and landmarks of flower developmental stages were described by Smyth et al. in 1990, including time duration starting from flower buttress formation till silique opening. Sepal is the outermost flower organ. In Arabidopsis, four sepals form the whorl surrounding the petals and generative organs of the flower. Arabidopsis sepal is regarded as a model system for studies of morphogenesis because of its simplicity, accessibility and reproducibility of morphogenesis (Roeder 2021). The mature sepal is a slightly curved, green photosynthetic organ with size of about 1 mm^2 so the entire morphogenesis can be imaged in confocal microscopy (Zhu et al. 2020). Moreover, each flower bud has four sepals and one inflorescence often has over 100 flowers, which gives up to 400 sepals on each plant. In the wild type, the size and shape of the sepals is robust, especially for flowers number 10 to 25 of the main inflorescence shoot (Hong et al. 2016). Structurally, the sepal consists of approximately 5 layers of cells: abaxial (outer) epidermis (comprising pavement cells, stomata guard

cells and unicellular trichomes), three layers of mesophyll cells with embedded vascular bundles, and adaxial (inner) epidermis facing the petal (Roeder 2021). Abaxial epidermal cells have primary walls. The outer periclinal wall is covered by a cuticle, which influences the wall mechanics and can form distinct surface patterns. Pavement cells of the sepal epidermis exhibit a large variety of sizes and have been divided into two cell types: small pavement cells and giant cells (Roeder 2010, Mollier et al. 2023). The giant cells are present only in the abaxial epidermis (Roeder et al. 2010). They are on average 360 μm (±150 μm standard deviation) long and their presence is used as a marker for sepal organ identity, distinguishing sepals from other floral organs (Pelaz et al. 2000).

Arabidopsis sepal has been an object of a number of fundamental studies on plant development (Roeder 2021, Kierzkowski et al. 2012, Routier-Kierzkowska and Runions 2018, Echevin et al. 2019, Roeder 2021, Le Gloanec et al. 2022), including the role of cell wall mechanics in this process (Hervieux et al. 2016, Tsugawa et al. 2017). Sepal development takes about 13 days from primordium till open flower with mature sepals (Smyth et al. 1990). *In vivo* studies showed that at the beginning of the development, the entire sepal primordium grows quite intensively, including the sepal tip. Later on growth rates at the tip slow down and the growth gradient with growth rates increasing basipetally becomes apparent. The slow growth region gradually expands towards the base as development progresses (Hong et al. 2016, Hervieux et al. 2016, Tsugawa et al. 2017). These changes are accompanied by changes in cell division frequency. During early developmental stages, cells at the sepal tip undergo frequent divisions. As development progresses, cell divisions cease at the tip while they continue to occur at the basal part. Moreover, individual epidermal cells exhibit heterogeneous growth patterns, varying in expansion rate and directionality (different growth anisotropy) (Tauriello et al. 205, Hong et al. 2016, Hervieux et al. 2017). These processes together contribute to sepal elongation and help evolve its initially curved shape to a flattened leaf-like shape at the end of development (Roeder 2021). The cells differ in ploidy, which is related to the final cell size. Larger polyploid cells, the giant cells, formed by endoreduplication affect tissue properties and help to maintain the shape of the organ (Robinson et al. 2018).

In vivo studies of Arabidopsis sepal development have been applied also to investigate how its shape is maintained and how growth directions of cells are coordinated.

Investigations on sepal epidermis revealed that CSI1 protein, the CSC element at contact with cortical microtubules, is essential for maintaining consistent growth directions among neighbouring cells. The *csi1* mutant displays less coordinated cell expansion, suggesting that proper arrangement of cellulose fibrils is crucial for organ elongation (Mollier et al. 2023). The mechanical simulation model based on microtubule observations showed that accumulation of stress on the tip of the sepal where microtubules are resisting tangential tension, hinders further transverse expansion of the sepal and arrests growth at the tip (Hervieux et al. 2016). These studies revealed that cortical microtubules are necessary to maintain proper shape and size of the sepal. This is further supported by the observation that loss of microtubule guidance in cellulose deposition for the newly formed cell wall layer results in shorter sepals and modification in pavement cells shape as described for *csi1* mutant. Giant cells which are approximately straight in the wild type were bent to form snaky shapes in the mutant (Mollier et al. 2023). This suggests that cellulose alignment guided by microtubules is necessary to maintain shape of cells and the whole organ.

Arabidopsis sepal epidermis was also an object to develop a protocol for quantifying elasticity of cell wall by osmotic treatment. The extent of shrinkage resulting from osmotic treatment (plasmolysis) can be used to estimate the cell wall elasticity. In this way, one can compare sepals of mutants, and in combination with mechanical simulations provide quantitative estimates of the cell wall Young's modulus (Sapala and Smith 2020).

The epidermis of Arabidopsis sepals has also been used to study the formation of cuticle and cuticular pattern on the epidermis surface during the late stages of sepal development. The pattern formation has been shown to be influenced by genes such as *CUTIN SYNTHASE 1* (*CUS1*) and *CUTIN SYNTHASE 2* (*CUS2*), which play key roles in cuticle biosynthesis and organisation (Hong et al. 2017, Shi et al. 2011). However, the process of cuticular pattern formation on individual cell surface was not yet examined.

1.3 Cuticle as the interface between shoot and environment: structure, function and pattern formation

Cuticle is the outermost layer of outer periclinal cell walls of the shoot epidermis that separates plant organs from the environment. It covers leaves (Cheng et al. 2019, Jenks et al. 2002), flower organs (Huang et al. 2017, Mazurek et al. 2013) and stems (Jenks et al. 2002). The main components of cuticle are cutin, waxes and polysaccharides, which all together form a heterogeneous lipidized outer region of the cell wall (Fernández et al. 2017). Also small amounts of phenolic acids and flavonoids are often present in cuticle (Reynoud et al. 2021). Cutin is a polymer that forms a three-dimensional network (scaffold) built by fatty acids (C_{18}, C_{16} and C_{22}) connected with intermolecular ester bonds (Kunst and Samuels 2003, Samuels et al. 2008, Kunst and Samuels 2009). This network is impregnated with intracuticular waxes (hydrophobic mixture of aliphatic long-chain fatty acids and their derivatives) and sometimes also with wall polysaccharides. Cuticle precursors, i.e. cutin monomers (carbonic acids) and components of wax, are synthesised in the protoplast, secreted as droplets and released to the cell wall where they move to the outer wall regions. The final assembly of cutin takes place *in muro* (in the cell wall or on its surface) via esterification of mono- or oligomers (Hejnowicz 2002, Skrzydeł et al. 2021). Esterification of cutin is executed by enzymes, however, it has also been postulated that cutin can self-assemble as has been shown *in vitro* on mica surface for one of the cutin monomers. This monomer created a multilayer pattern where parallel, nearly vertical molecules were arranged in layers (Heredia-Guerrero et al. 2009). It is thus likely that if cutin were built of regularly arranged monomer molecules *in vivo*, the cutin-made scaffold of the cuticle would be structurally anisotropic (Skrzydel et al. 2021). Some authors postulate the existence of nanoparticles, called cutinsomes, which are formed by self-assembly of cutin monomers *in muro*. In the cutinsomes, cutin and wax precursors are transported from lipid bodies in the cytoplasm to the cell wall (Stępiński et al. 2020) and thus cutinsomes are involved in cuticle formation as described for tomato fruit (Segado et al. 2020). However, the role and behaviour of cutinsomes require further investigations.

Cuticle forms early in organ development and consists initially of a thin layer to which the new material is continuously added (Skrzydel et al. 2021). The cuticle thickness is extremely variable among different plant species, organs, developmental stages and even within parts of the same shoot, ranging from less than 1 up to 100 μm. The

composition of cuticle also varies among species and organs, especially in the contribution of different carbonic acids (Hejnowicz 2002). For example, in Arabidopsis cuticle on the leaf and stem is electron-opaque, while petals have an amorphous electron-lucent cuticle suggesting that the composition of carbonic acids of cuticle of these two organs is different (Mazurek et al. 2017).

Three layers can be often distinguished in the cuticle: (i) epicuticular waxes, which contact the external environment; (ii) cuticle proper; (iii) cuticular layer, which overlays the non-cutinised primary cell wall. The outermost layer of epicuticular waxes consists of long-chain fatty acids and derivatives, such as alkanes, alcohols, and aldehydes. Waxes, due to their physicochemical properties can spontaneously create crystals. The morphology of epicuticular waxes depends on their chemical composition and is affected by the physicochemical characteristics of the underlying cuticle layers (Koch and Ensikat 2008). The cuticle proper is built of cutin scaffold impregnated with intracuticular waxes. The innermost cuticular layer is in turn built of cutin and wax along with cellulose and other wall polysaccharides (Skrzydeł et al. 2021). The three layers can be distinguished in the cuticles covering the Arabidopsis shoot epidermis, including the cuticle on sepal surface.

The cuticle plays a crucial role as the interface between the growing and mature epidermis and the external environment, mediating stress transmission and protecting the organ surface. It acts as a strong barrier against mechanical injury, water loss, and pathogen attack (Skrzydeł et al. 2021). Since the cuticle overlays the outer periclinal walls, its properties and remodelling can influence mechanical behaviour of the organ surface walls during development. The cuticle resists deformation, prevents desiccation, and interacts structurally with the cell wall located beneath. These functions become especially important during organ growth. To accommodate these mechanical demands and facilitate performance of other cuticle functions, the cuticle may develop specific surface patterns known as cuticular ridges.

Elaborate pattern of cuticular ridges covers the surface of petal and sepal epidermis in Arabidopsis, similar to many other plant species (Hong et al. 2017, Fernández et al. 2017, Skrzydeł et al. 2021). The function of ridges in general depends on the type of organ. For example, in petals their regular spacing may act like a diffraction grating and may thus serve to attract pollinators (Whitney et al. 2009). The ridges may prevent water

loss (Buschhaus and Jetter 2011) or wetting of epidermis surface by promoting water droplet formation (Whitney et al. 2009). However, for sepals their function is not fully understood. One possibility is that ridge formation reflects the mechanical role of the cuticle. This idea is supported by models suggesting that growth-induced mechanical stresses can drive ridge formation (Kourounioti et al. 2013). Cuticular ridges may develop as a structural adaptation that helps to support the outer surface during rapid or uneven growth. In this context, ridge formation may help to maintain epidermal integrity by reinforcing the cuticle and modulating stress distribution across the organ surface.

Patterns of cuticular ridges differ between species (Kourounioti et al. 2013), organs (Nawrath et al. 2013) and even between epidermal cells of various shapes (Nawrath et al. 2013). For example, conically-shaped cells of Arabidopsis petal epidermis are covered by wavy cuticular ridges at the top of the cell and straight ridges on cell sides (Nawrath et al. 2013). In Arabidopsis sepals in turn, the ridges are wavy and usually directed along the long axis of the organ in the case of elongated epidermal cells (Hong et al. 2017) while ridges on the surface of non-elongated cells are aligned to the lower extent. Relating of this variation of the cuticular pattern to cell morphogenesis (cell wall growth and changes in the surface curvature) may shed a light on the mechanism of ridges formation. Investigation of such relationships is aided by cuticle autofluorescence that is attributed to cutin (Donaldson 2020) and facilitates tracking of pattern formation *in vivo* without staining. The exact origin of cutin autofluorescence remains unclear.

1.4 Theories explaining cuticular pattern formation

The earliest theory explaining formation of cuticular pattern was proposed by Martens in 1933. He postulated that ridges appear on the epidermal surface as a result of mechanical imbalance between the expanding cell wall and the overlying cuticle. New cutin precursors are added in the space between existing cutin network in the wall of an elongating plant cell in the places where cutin cannot expand at the same rate as underlying cell wall. If new cutin precursors are secreted and accumulate in excess at the outer surface of elongating epidermal cells (an effect often described as oversecretion), the cuticle, being relatively stiff compared to the expanding wall, undergoes mechanical buckling, leading to the formation of ridges (Martens 1933).

Recent studies of the abaxial epidermis of Arabidopsis sepal support the role of cutin oversecretion in the cuticle ridges formation (Hong et al. 2017, Smyth 2017). Cuticle ridges are formed first on the top of the sepal and then spread basipetally on the sepal surface. The frontier of cuticle ridges precedes slightly the frontier of slowing down of cell expansion, which moves in the same direction, indicating that ridges formation starts when growth of the underlying cell wall slows down. Ridges initiation follows the expression of *CUS1* in early sepal development. The *CUS2* is in turn expressed later and is required for ridges maintenance. Both the genes encode an enzyme involved in cutin polymerisation *in muro*. When the *CUS2* and *CUS1* are silenced, there appear places on the cell surface where ridges are not formed (Hong et al. 2017). Studies on *cdr* (*defective in cuticular ridges*) mutant, in which the gene encoding enzyme involved in synthesis of one of the most abundant flower cutin monomers is affected, also showed that cutin production is necessary for cuticle ridges formation. Lack of the cutin monomers resulted in smooth cuticle on the sepal epidermis surface (Panikashvili et al. 2009).

It has been postulated that the oversecretion of cutin induces mechanical instability of the cuticle layer, which leads to buckling. However, buckling requires compressive in-plane stress acting in the smooth cuticle prior to the buckling, a condition that is not fully understood in the case of ridges formation and requires further study. Buckling could occur if cuticle proper expansion were restricted. Then the incorporation of new cutin precursors into the existing cuticle layer would generate compressive stress that causes cuticle to buckle (Skrzydeł et al. 2021).

Kourounioti et al. (2013) modelled cuticle as an incompressible, nonlinearly elastic material, which adheres tightly to the stiffer underlying cell wall. In this model of cuticular ridges formation, the patterns of cuticular ridges reflect features of the stress field within the cuticle layer. Very regular patterns of ridges that are correlated over long distances arise via compression in the direction orthogonal to ridges and tension parallel to them. Disordered patterns of ridges reflect biaxial compression, whereas a smooth cuticle is likely to be under biaxial tension. The in-plane compressive stress may arise from anisotropic cell growth combined with restricted expansion of the cuticle proper and continued cutin deposition. Ridge formation is thus a consequence of mechanical instability in the cuticle due to this compressive stress (Kourounioti et al. 2013).

More recent research on the *Hibiscus trionum* L. petals highlighted that changes in the stiffness of cuticle layers over time are an important input to the model of cuticular pattern formation and measurements of the stiffness are necessary for understanding how cuticular patterns form (Lugo et al. 2023, Airoldi et al. 2024). Based on these ideas, Lugo et al. (2023) built a three-dimensional model that accounts for turgor-induced bulging of outer cell walls, on which cuticular pattern is formed, and regards the cuticle as comprising two layers with different mechanical properties: soft cuticular layer and stiff film of cuticle proper. Their simulations were able to reproduce appearance of new ridges and their growth, suggesting that cuticle expansion alone can create the compressive forces needed to form these patterns. Moreover, pioneering measurements of stiffness of cuticle layers of *Hibiscus trionum* petals over time showed that both the cuticle proper and the underlying cuticular layer change their stiffness during development, with the biggest drop in stiffness in the cuticle layer at the open flower stage (Airoldi et al. 2024). This softening may affect not only how the ridges are formed but also the overall shape and size of the petal. However, despite this progress, the model remains theoretical and does not yet account for the full biological complexity. For instance, the stress distribution at the interface between the primary cell wall and the cuticle remains poorly characterized, although it may indirectly affect ridge formation. Moreover, the cell wall itself is a mechanically heterogeneous structure, and the in-plane tensile stress resulting from internal turgor pressure varies between wall layers (Lipowczan et al. 2018), adding further complexity to the system. Mechanical stresses arise not only within individual epidermal cells but also at the organ scale, due to structural and mechanical differences between inner and outer organ tissues (Hejnowicz and Sievers 1997, Wojtaszek et al. 2007, Hejnowicz 2012). Verger et al. (2018) demonstrated that cell–cell adhesion coordinates tensile stress patterns throughout the epidermis, maintaining mechanical continuity. Disruption of adhesion can have an impact on stress distribution, which may indirectly influence the cuticle pattern as it modifies the mechanical environment in the cell wall and cuticle. These insights underscore the necessity of considering the mechanical complexity of the epidermis when studying its structure and function. The models may overlook such critical aspects, while quantitative analyses of the relationships between cuticle ridges pattern, growth anisotropy of epidermal cell walls, and accompanying cutin and wax deposition in individual cells may shed a new light on the mechanism of the cuticle ridges formation.

Despite extensive knowledge about the cell wall composition and structure there is currently no comprehensive study integrating the dynamics of local wall composition, structural anisotropy, and anisotropic growth with surface patterning. Therefore, the present thesis addresses this gap by investigating the *Arabidopsis thaliana* sepal epidermis during the maturation stage, combining Raman imaging with detailed structural and growth analyses.

2. OBJECTIVES

The primary cell wall on the surface of abaxial epidermis of *Arabidopsis thaliana* sepal, the main object of this investigation, is easily accessible because it is the outermost cell wall of the flower bud. It can thus be examined *in vivo* without flower damage and samples required to examine the wall components are relatively easy to obtain. Therefore, the outer periclinal cell wall of Arabidopsis sepals at late stages of development was chosen to investigate the cell wall composition and cuticular pattern formation in wild type and cell wall mutants. Raman spectroscopy was used in these investigations because it facilitates assessment of overall cell wall composition during single measurements. *In vivo* imaging of the primary cell wall surface during sepal maturation provided complementary information about the dynamics of the cell wall structure, with focus on the formation of the cuticular pattern.

The objectives of the present investigations were to verify the following hypotheses:

Hypothesis 1: Primary cell wall composition of Arabidopsis sepal epidermis changes during the sepal development and is affected by *csi1, mad5, pme32,* and *xyl1* mutations.

Hypothesis 2: Primary cell wall of Arabidopsis sepal epidermis exhibits structural anisotropy resulting from alignment of its components.

Hypothesis 3: Deficiency of one cell wall component in Arabidopsis mutants activates a compensatory mechanism.

Hypothesis 4: The initial pattern of cuticular ridges appearing on the outer periclinal walls of Arabidopsis sepal is influenced by cell growth and geometry at the time of pattern formation.

Hypothesis 5: The pattern of cuticular ridges is changing during the expansion of sepal surface.

3. MATERIALS AND METHODS

3.1 Plant material and growth conditions

Arabidopsis thaliana L. (Heynh.) lines used for Raman imaging were: Col-0, *csi1-3* (AT2G22125), *pme32-2* (AT3G43270), *xyl1-4* (AT1G68560), *mad5* (AT1G80350). All the mutant seeds, on the Col-0 background, were graciously provided by Profs Arezki Boudaoud and Olivier Hamant from École Normale Supérieure de Lyon, France. Plants were grown in soil in a growth room, under long day conditions (16 h light / 8 h darkness), illumination 78 µmol m^{-2} s^{-1}, temperature of 22±0.5°C and 60-70% relative humidity.

Arabidopsis Col-0 and *mad5* mutant (AT1G80350) were only used for confocal live imaging. Seeds were stratified for 2 days at 4°C in the dark to induce synchronous germination. Plants were grown in soil in a growth room, under long day conditions (16 h light / 8 h darkness), illumination 95 µmol m^{-2} s^{-1}, at a temperature of 22±1°C and 60-70% relative humidity. The plants were used for live imaging and electron microscopy analysis of flower buds at developmental stages 8-12 (Smyth et al. 1990).

3.2 Raman Spectroscopy

3.2.1 Plant dissection and sample preparation for Raman spectroscopy

Inflorescences were cut off from the plants, and abaxial sepals were dissected from the buds in stage 10 or 12 of flower development (Smyth et al. 1990). Samples of cell wall surface were prepared for Raman spectroscopy measurements using a modified protocol of Wuyts et al. (Wuyts et al. 2010). Briefly, the sepals were fixed in 70% ethanol (first kept under vacuum for one hour at room temperature, then fixed at 4°C for at least 24 h). Afterwards, they were treated with absolute chloroform for 10 min (to remove membranes and partially epicuticular waxes), rehydrated in decreasing ethanol series (70%, 50%, 30%) followed by deionized water (5 min in each medium), placed in protoplast lysis buffer of sodium dodecyl sulphate and sodium hydroxide (1% SDS in 0.2M NaOH) for 3 h, treated with 0.01% α-amylase (Sigma-Aldrich; from *Bacillus licheniformis*) in PBS (Phosphate Buffered Saline, pH 7.0) in 37°C overnight (to remove

residual starch), moved to over-saturated water solution of chloral hydrate (200 g / 50 ml) for 4 h (to remove protoplast remnants), and rinsed in water (3 x 15 min).

Such prepared sepal samples were placed on glass slides (1 mm thick) with the adaxial epidermis facing the slide, immersed in pure deionized water to preserve environmental conditions during Raman imaging, and covered by CaF_2 coverslips, 0.15-0.18 mm thick (CAMS1602, Laser Optex).

3.2.2 Raman imaging

Raman data were collected using WITec confocal Raman microscope alpha300R, equipped with a linear polarised laser (air-cooled solid-state laser, λ = 532 nm, P = 30 mW), a thermoelectrically cooled CCD camera, and Zeiss C-Apochromat (100x/1.25 NA) water immersion objective. The excitation laser radiation was coupled to the microscope through a polarisation-maintaining single-mode optical fibre (50 µm diameter). Raman scattered light was focused onto a multi-mode fibre (50 µm diameter) and a monochromator with a 600-line mm^{-1} grating providing 3 cm^{-1} spectral resolution. The spectrometer monochromator was calibrated with the emission lines of the Ne lamp, and before each measurement series, the silicon Raman band (520.7 cm^{-1}) was used as a reference value for checking the spectra. The precision of the horizontal movement of the sample during measurements was ± 0.2 µm. The lateral resolution (LR) was estimated according to the Rayleigh criterion (LR = 0.61λ/NA) as LR = 259 nm. All spectra gathered during Raman imaging ranged from 120-4000 cm^{-1}.

Surface Raman imaging was employed to collect the signal from outer periclinal walls of abaxial sepal epidermal cells in two ways: along transects within individual cell walls (see **3.2.3 Transect Raman measurements and data analysis using Multivariate Curve Resolution–Alternating Least Squares toolbox**); and for square-shaped portions of cell walls, further referred to as maps (see **3.2.4 Cell wall maps**).

3.2.3 Transect Raman measurements and data analysis using Multivariate Curve Resolution – Alternating Least Squares toolbox

First, a low-resolution image of the whole sepal was obtained to choose the region of interest (**Fig. 3.1A**), such that it was located in the basal part of the sepal, the chosen cells were not adjacent to stomata and were not giant cells. On this basis, 10 cells were selected from each sepal. Five measurements were performed along the long axis of each of these cells (which was also the long axis of the sepal), further referred to as transect measurements (**Fig. 3.1B**). For every measurement, an integration time of 1 s and 20 accumulations were applied. Four sepals in stage 10 and four in stage 12 of flower development were analysed in such way for each genotype (Col-0 and cell wall mutants).

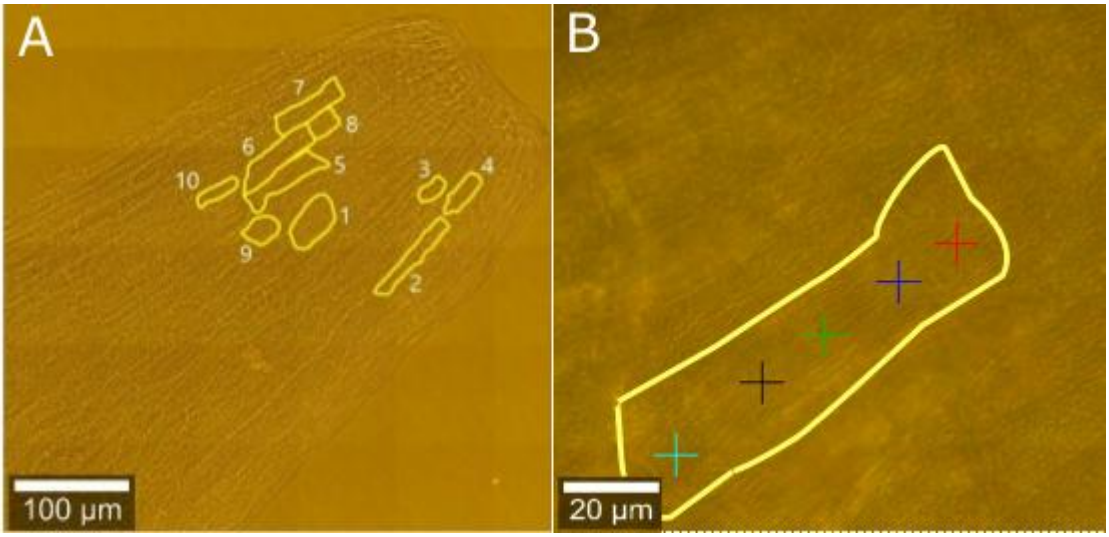

Fig. 3.1 (**A**) Exemplary image of the basal part of Col-0 sepal in stage 12 with 10 cells selected for measurements. (**B**) Zoomed image of cell number 7 shown in A, with a transect of 5 measurement points labelled by crosses.

Analysis of transect measurements was performed using the Multivariate Curve Resolution – Alternating Least Squares (MCR-ALS) toolbox of MATLAB (MathWorks, Natick, MA, USA) (Felten et al. 2015). Obtained spectra were cut to the range 750-1800 cm^{-1}, and baseline correction, smoothing with the Savitzky-Golay filter, and normalisation by total area were performed for this range. Such prepared spectra were subject to further MCR-ALS analysis aiming at the identification of so-called Component spectra (Felten et al. 2015). For each set of 200 transect measurements (4 sepals x 10 cells x 5 measurement points = 200 measurements), obtained for stage 10 or

12 sepals of a given genotype, two Component spectra (further referred to as Component 1 and 2) were distinguished with a minimum number of iterations performed to reach the convergence (minimum 98% fit). Then, based on the concentration profiles of the two Components, the Component with the greater contribution in each spectrum was recognised for the two developmental stages (**Table 3.1**), and all the spectra were divided into those more similar either to Component 1 or to Component 2. Second, the Component spectra obtained for Col-0 sepals were used as references, and Components 1 and 2 recognised for each developmental stage of mutants were compared to the Col-0 reference spectra using Euclidean distance calculation.

Spectrum number	CONCENTRATION	
	Component 1	Component 2
…	…	…
15	0.051	0.036
16	0.023	0.059
17	0.043	0.045
18	0.016	0.063
19	0.024	0.057
20	0.034	0.049
21	0.032	0.054
22	0.022	0.059
23	0.063	0.031
24	0.059	0.033
25	0.039	0.048
26	0.062	0.031
27	0.089	0.012
28	0.082	0.016
29	0.071	0.024
30	0.064	0.029
...	…	…
200	0.090	0.008

Table 3.1 Fragment of the table showing concentration profiles of Components 1 and 2 for every spectrum obtained in transect measurements (in this case Col-0 stage 10). Spectra with a higher concentration of Component 1 are marked in blue, Component 2 in red.

3.2.4 Cell wall maps

In order to choose the best region for the analysis, the cell surface was first visualised as 40 μm × 40 μm Raman images, further referred to as large maps (square outline in

Fig. 3.2A). Then, data were acquired from a small map, 10 μm × 10 μm, i.e. the region located in a central part of the chosen cell, with an integration time of 40 ms per spectrum, using a step size of ~0.33 μm in both X and Y directions (resulting in a 30 × 30 grid and 900 spectra in total). The central part of the cell wall was chosen to minimise distortion due to the surface convexity. In such wall parts, the wall is nearly perpendicular to the laser beam (**Fig. 3.2B**). The procedure has been applied to 10 sepals of stage 12 for each genotype. From each sepal, one non-giant pavement cell located in the basal part of the sepal was selected for imaging.

The imaging was performed for motionless samples while the polariser orientation was changing from 0° to 90°, with a 15° step, in order to identify the orientation with the maximum signal for the orientation-dependent cellulose band around 1098 cm^{-1}. Further analyses were performed for orientations 0° to 90°, with a 30° step, where the new 0° referred to the maximum intensity of the band at 1098 cm^{-1}. In other words, the first 7 maps were collected for each 10 μm × 10 μm region at different polariser orientations, and after the orientation with the maximum intensity was identified, 4 of them were used for further analyses. The same procedure of selection of the 4 maps to be further analysed was performed for orientation-dependent cuticle-specific bands at 1500-1700 cm^{-1}. Crystalline and amorphous celluloses from *Halocynthia roretzi* (Ruel et al. 2012) were used as reference samples for cellulose. Raman measurements for the reference samples were performed for single points at different polariser angles as explained above.

The Raman output data were initially post-processed in WITecProject FIVE 5.1.2 software (Oxford Instruments, Abingdon, Oxfordshire, England) by performing the auto baseline correction using a polynomial function of degree 3, then submitted to a cosmic ray removal procedure (comparing each pixel to its adjacent pixels' signal), and finally smoothed by the Savitzky–Golay filter. Chemical images were then created by integrating the CH and CH_2 stretching-related bands from the 2898-2940 cm^{-1} region (Gierlinger and Schwanninger 2007, Bock et al. 2021) (**Fig. 3.2A**) to visualize variation in signal intensity of the epidermal cell wall. Next, for each 10 μm × 10 μm cell wall map (**Fig. 3.2B),** K-means cluster analysis using the Manhattan distance was applied to distinguish averaged spectra for the cell wall portions located between cuticular ridges (non-ridged cluster) and for the ridges with underlying cell walls (ridged cluster). Every averaged spectrum obtained from the cluster analysis was normalised by dividing the raw signal by the total integrated intensity of all bands. An alternative method was also

tried to visualise differences between averaged cluster spectra using the demixer procedure, involving subtraction of the ridged cluster spectrum from the non-ridged cluster spectrum, and vice versa (see **4.1.2 Assignment of spectrum peaks to primary cell wall components of ridged and non-ridged portions of primary cell wall**).

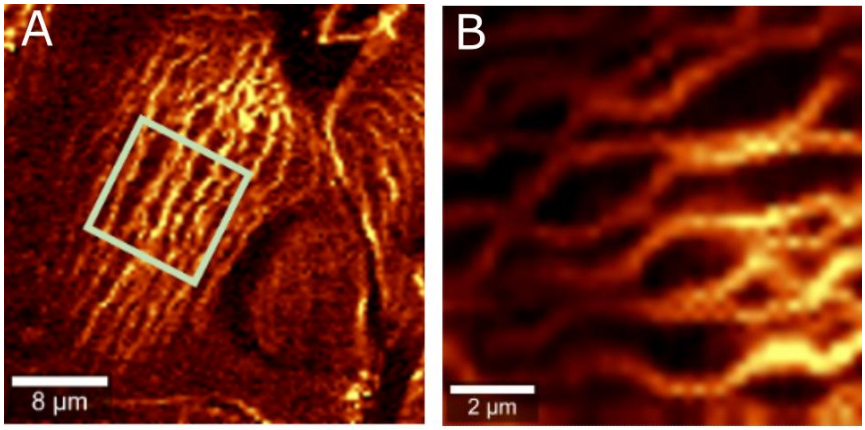

Fig. 3.2 Raman maps of the superficial cell walls of Arabidopsis Col-0 sepal epidermis obtained by integrating bands from 2737-2858 cm^{-1} range (CH band; Gierlinger and Schwanninger 2007, Bock et al. 2021) characteristic for all cell wall components. **(A)** An exemplary large map (40 µm x 40 µm) on which a region selected for further analysis (a small map) is outlined by the white square. **(B)** Exemplary small map (10 µm x 10 µm) obtained from a nearly flat portion of the sepal surface, which was used for further analysis.

The band fitting analysis was performed for every averaged cluster spectrum using GRAMS/AI 9.2 software (ThermoFisher, Waltham, MA, USA) by the Voigt function with the minimum number of components necessary to reproduce the observed band arrangement in the experimental data. This analysis facilitated the determination of band parameters, including the position and integrated intensity of the individual bands. By employing this approach, a comprehensive analysis of the spectral characteristics was done to separate cellulose-specific symmetric (sym) and asymmetric (asym) vibrations related to the bands, e.g. 1098 cm^{-1} $(C\text{-}O\text{-}C)_{asym}$ and 1122 cm^{-1} $(C\text{-}O\text{-}C)_{sym}$ (see **Table 4.3**), from non-cellulose bands originating from vibrations related to the specific functional groups of other polysaccharides present in the cell wall. The calculation of the integrated intensity ratio for cellulose-related bands (1098 cm^{-1} and 1122 cm^{-1}) was used to follow the polarisation angle-dependent character of the cellulose signal, facilitating the investigation of the microfibrils alignment. The values of the integrated intensity ratios estimated for cellulose-related bands were calculated for four different polariser angles (every 30° from 0° to 90°) and normalised by the sum of these values.

The same procedure with calculation of the ratio 1500-1700 cm^{-1}/1737 cm^{-1} was used to analyse cuticle-specific bands, related to: (C=C) ring (Ramirez et al. 1992, Heredia-Guerrero et al. 2014); (C=C) phenolic acid (Heredia-Guerrero et al. 2014); (C=C) conjugated ring of coniferyl alcohol (Gierlinger and Schwanninger 2006); (C=O) coniferyl aldehyde; (C=O···H) (Gierlinger and Schwanninger 2006); and (C=O) ester (Ramirez et al. 1992, Séné et al. 1994, Gierlinger and Schwanninger 2007, Heredia-Guerrero et al. 2014, Mateu et al. 2016). The integrated intensity ratio for cuticle-specific bands was calculated to follow the polarisation angle-dependent changes (from 0° to 90°) and estimate the extent of cuticle component alignment.

Polarisation angle-dependent changes were visualised using MATLAB as polar plots based on signals of the above-described specific regions of the spectra associated with cellulose or cuticle components. The range of 0° to 90° was repeated to 360°, for the visualization of periodicity. Least Squares fitting method (Miller 2006) (LS fitting function in MATLAB) was applied to assess the similarity between cellulose-specific bands with reference samples of crystalline and amorphous cellulose, i.e. to find the best fitted coefficients to represent the polar plot for the wall sample by the sum of reference plots multiplied by the coefficients.

Putative compensation effect was analysed using the relative contribution of signals from pectin, cellulose and hemicellulose in averaged spectra of non-ridged cluster obtained at the maximum intensity of the polarisation-sensitive cellulose band 1098 cm^{-1}. For this purpose, selected bands specific to individual components were chosen for pectins (856 cm^{-1}), cellulose (1098 cm^{-1}), and hemicelluloses (1313 cm^{-1}) (**Fig. 3.3A** and **B**). To better visualise the relative contribution of signals originating from different cell wall components, values of Col-0 were subtracted from those of mutants. Data analysis and visualization were performed using MATLAB. Additionally, STATISTICA 13 (TIBCO Software) software was employed for statistical analyses. Because of non-normal data distribution, the non-parametric test of Mann-Whitney was used to assess the statistical significance of observed differences between Col-0 and mutants.

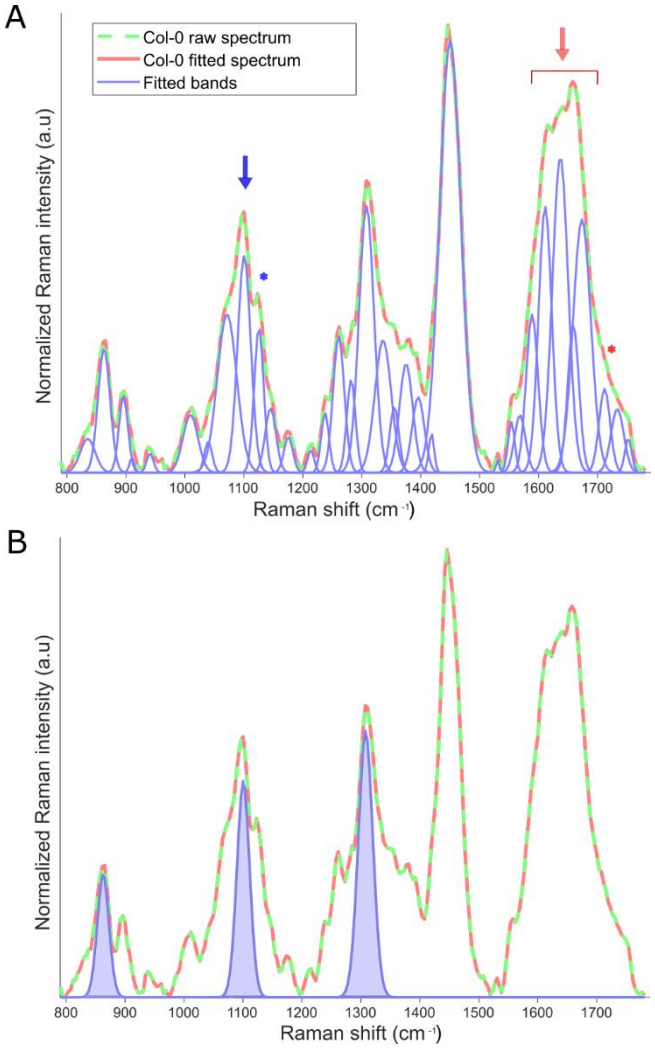

Fig. 3.3 (**A)** Exemplary Col-0 cell wall spectrum obtained for the sample at the orientation of the polarisation plane where the intensity of the cellulose-related band at 1098 cm^{-1} was the highest. Curves representing selected bands obtained in GRAMS were used for signal intensity assessment and are plotted together with the resulting fitted spectrum. The blue arrow points to the orientation-sensitive band for cellulose (1098 cm^{-1}, $(C\text{-}O\text{-}C)_{asym}$), and the blue asterisk labels the non-sensitive band (1122 cm^{-1}, $(C\text{-}O\text{-}C)_{sym}$) (See **Table 4.3**); the red arrow points to the region including orientation-sensitive bands for cutin and waxes (1639 cm^{-1}, 1660 cm^{-1}, 1678 cm^{-1}); red asterisk labels the non-sensitive band related to cutin, pectins, and hemicellulose (1739 cm^{-1}). (**B)** The same spectrum with selected bands specific for cell wall polysaccharides used for comparison of their relative signal contribution: for pectins around 856 cm^{-1}, for cellulose around 1098 cm^{-1}, and for hemicelluloses around 1313 cm^{-1}.

3.3 Confocal live imaging

3.3.1 Plant dissection and sample preparation

Apical portions of inflorescence, including about 10 mm long stems, were isolated from four-week-old plants and dissected with fine tweezers in order to remove floral buds

older than stage 8 (Smyth et al. 1990), such that abaxial sepals were exposed in the stage 8 floral buds. The inflorescence portions with the undamaged sepal and remaining buds were used for growth tracking. They were transferred onto Petri dishes (Ø60 mm) filled with ½ MS medium supplemented with 1.5% agar, 1% sucrose and 0.1% Plant Protective Medium (PPM, Plant Cell Technology), by placing and immobilisation of the sample in the incision made in the medium. Sepals were imaged every 24 h for up to 4 days. If needed, isolated inflorescence portions were repositioned before the confocal scan such that the same side of the sample was always observed. Between consecutive imaging, samples were transferred to the growth chamber and cultured *in vitro* under long day conditions (16 h illumination, 80 µmol m^{-2} s^{-1}).

3.3.2 Confocal laser microscopy

Confocal imaging was performed with two upright confocal microscopes equipped with a long working distance water immersion 40× objectives (1 NA, Apochromat):

- Zeiss LSM800 (to follow the cuticular ridges formation and changes of ridges pattern);

- Zeiss LSM700 (to follow changes of ridges pattern).

For both microscopes excitation was performed using a diode laser at 488 nm for YFP, and the signal was collected between 500 and 600 nm. Confocal stacks were acquired at 1024×1024 resolution (170 µm x 170 µm) with 0.7 µm distance in the z-dimension.

3.3.3 Confocal stacks analysis

Stacks of confocal images were processed with the 3D image analysis software MorphoGraphX (Barbier de Reuille et al. 2015, Strauss et al. 2022). The surface of each sepal was detected using the *edge detect* tool with a threshold of 1800-6000, followed by the *edge detect angle* tool with a threshold of 1800-5000. The surface was extracted using the *marching cube* tool (size 1 µm) and an initial mesh representing the sample surface was created. The mesh was subdivided three times and smoothed to eliminate local irregularities and to obtain a good fit to the sample surface. The autofluorescence signal of the epidermal cell surface (from +2 µm above to -2 µm below the mesh) was then projected on the reconstructed surface to visualize cuticular ridges. The manual

segmentation in MorphoGraphX was performed to segment cells at every time point. The same cells were identified at each time point.

3.3.4 Assessment of cell expansion, shape and alignment of cuticular ridges

Cell expansion was represented by growth ratio in area (GR) computed as:

$$\mathrm{GR} = \frac{\mathrm{CA}_{T_{n+1}}}{\mathrm{CA}_{T_n}}$$

where CA_{T_n} - cell surface area at the beginning of time interval, $\mathrm{CA}_{T_{n+1}}$ - cell surface area at the end of time interval.

Colourmaps representing growth ratio for every cell between two time points were displayed as overlaid on the first time point.

Cell principal growth directions (PDGs) were assessed for polygons defined by three-way wall junctions of each cell (Barbier de Reuille et al. 2015). This way direction of maximal and minimal growth and corresponding growth ratios in length (computed analogously to GR) were assessed. Cell growth anisotropy (Ani) was computed as:

$$\mathrm{Ani} = \frac{\mathrm{PDG}_{\mathrm{max}}}{\mathrm{PDG}_{\mathrm{min}}}$$

where $\mathrm{PDG}_{\mathrm{max}}$ and $\mathrm{PDG}_{\mathrm{min}}$ are growth ratios in the direction of maximal and minimal growth, respectively.

Local PDGs, i.e. PDGs of small fragments of an individual cell wall, were computed using MorphoGraphX 2.0 *deformation* tool. The *deformation* tool predicts how the surface fragment at t=0 h would deform to achieve the shape observed at t=24 h, based on a continuous mapping of the displacement of user-defined landmarks. In order to compute local PDGs the following landmarks were defined: cell centre, three-way cell wall junctions, manually specified points in the middle between each two neighbouring cell junctions, additional landmarks manually added on the wall surface, which were identified based on the ridges pattern. The local PDGs were visualised as overlaid on the first timepoint map and were projected using the *product stretches* tool in MorphoGraphX 2.0.

Curvature was computed for the surface of each cell at a given time point and visualised using *project mesh curvature* tool. Curvature colourmaps showing local minimum, local maximum or local mean curvature were prepared using Radius = 10 μm (the spatial extent within which neighbouring points are considered for curvature computation; in the case of big *mad5* cells Radius = 25 μm) and Neighbouring = 3 μm (parameter of smoothing procedure to remove noise). Curvature directions, represented by crosses, were assessed for the entire periclinal wall of each analysed cell.

For each cell a shape parameter was computed as the ratio of the maximum length to the minimum length of the cell. The minimum and maximum lengths were computed using MorphoGraphX tool *length minor axis* and *length major axis*. The tool uses PCA on the mesh triangle positions weighted by their area in order to recognise the longer and shorter axes of the cell. All the cells were divided into 3 groups taking into account the shape parameter. In group 1, the shape parameter ranged from 1 to 2, group 2: 2.01 - 2.5, and group 3: more than 2.5 (**Fig. 3.4**).

For each cell also lobeyness parameter was computed using MorphoGraphX tool *lobeyness* that describes the degree of lobing or protrusions along the boundaries of a cell. Its values close to 1 are characteristic of smooth cell outlines, and bigger values are characteristic of cells with lobed outlines.

The above protocols were applied for 3 sepals of Col-0 and 3 sepals of *mad5*.

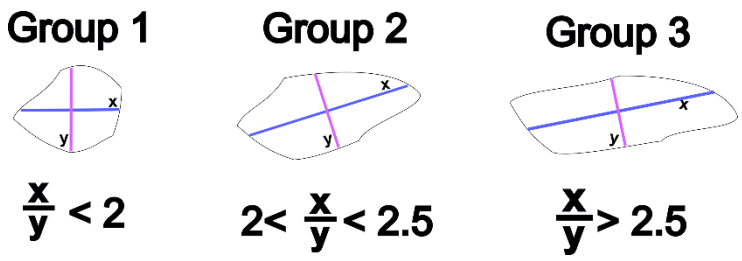

Fig. 3.4 Scheme showing shape parameter of cells belonging to the three shape groups.

Confocal images of sepal surface, on which cuticular ridges were well visible already at the beginning of observation, were used to analyse changes in ridges pattern. To measure anisotropy of cuticular ridges pattern the FibrilTool plugin of ImageJ was used

(Boudaoud et al. 2014). First, Z-stack projection with maximum intensity was obtained in ImageJ, which showed the surface with a clearly visible cuticular pattern on the cell surface, excluding fluorescence signal originating from internal cell layers (parenchyma cells). Such images of the sepal surface fragments were all prepared in the same way following the steps: (i) enhance contrast with saturation of pixels 10%, (ii) adjust contrast and brightness to remove noise between the ridges. Then, the anisotropy was measured using FibrilTool and visualised as red line segments for selected cells that exhibited the cuticular pattern and were present in three consecutive time points. The line segments represent the main direction of ridges while their length is proportional to the extent of ridges alignment (anisotropy).

A similar analysis was performed on a subcellular scale where the cell surface was divided into portions, the surface area of which was between 50 μm^2 and 300 μm^2. The endings of ridges were used as landmarks to identify the surface portions in consecutive time points. For each cell two to four portions were analysed as shown in **Fig. 3.5**. For every such portion its surface area and ridges anisotropy were noted. FibrilTool was used also for analysis of single ridges, during which selected ridges were followed individually at three time points.

All the computations were performed for 21 cells of 3 sepals of Col-0 and 25 cells of 3 sepals of *mad5*.

Statistical analyses were performed in STATISTICA 13 (TIBCO Software). Because of non-normal data distribution the non-parametric test of Mann-Whitney was used to assess the statistical significance of observed differences between Col-0 and *mad5*.

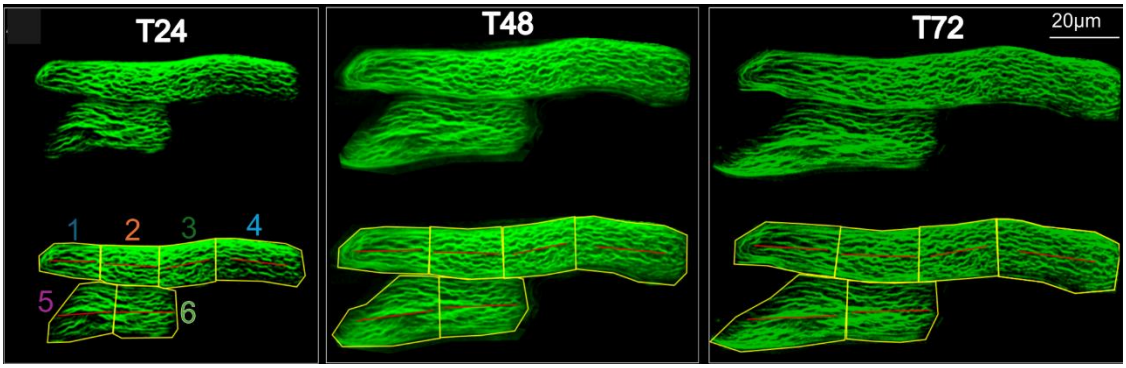

Fig. 3.5 Exemplary Col-0 cells (upper row) with cell portions selected for analysis of pattern of cuticular ridges using FibrilTool (lower row).

3.4 Sample preparation for electron microscopy

For transmission electron microscopy (TEM), sepals covered with cuticular ridges were dissected from floral buds from 4-week-old plants and fixed in 2.5% glutaraldehyde (pH 7.0) overnight. The samples were rinsed with 50 mM phosphate buffer (pH 7.0), post-fixed with 1% osmium tetroxide (OsO_4) for 2 h, rinsed in water, and dehydrated in a graded ethanol series. After dehydration, the samples were embedded in Epon resin. Ultrathin cross sections (90 nm thick) were mounted on 200-mesh copper grids, double-stained with uranyl acetate and lead citrate, and examined with a TEM (Hitachi H500).

For scanning electron microscopy (SEM), fresh floral buds were used. Images of sepals were acquired with a HIROX SH3000 tabletop microscope. The chamber was precooled to -20°C for at least 30 min before sample observation. Whole floral buds were mounted on conductive carbon double-sided tape on a sample holder, inserted into the chamber, sealed, vacuumed, and imaged at an accelerating voltage of 5 kV. Imaging was performed at magnifications: 500× to visualize the entire sepal, 1000× to examine the frontier of cuticular ridges on the sepal, 2000× to visualize cuticular ridges on individual epidermal cells while capturing groups of neighbouring cells, using default acquisition settings.

4. RESULTS

4.1 Composition and structural anisotropy of primary cell walls in Col-0 and selected mutants

4.1.1 Changes in primary cell wall composition during sepal maturation in wild type and mutants

Raman spectroscopy was first used to detect changes in the composition of primary cell walls during the late stages of sepal development in wild type and the selected cell wall mutants. This was addressed by comparing sepals in developmental stages 10 and 12 in plants of five different genotypes: Col-0 as a wild type, *csi1* and *mad5* in which cellulose fibril arrangement is affected, *pme32* with altered pectin methylesterification, and *xyl1* with altered XyG. In stage 10, the sepal is still growing, and cuticular ridges have not covered the whole sepal surface yet. Sepals in stage 12 are no longer growing, and their entire surface is covered with distinct cuticular ridges.

The composition of primary cell walls was assessed for the least convex fragments of cell walls. Five measurements were performed within each wall fragment, along the long axis of the cell, and are further referred to as transect measurements. The transect measurements were used to compare cell wall composition at the two developmental stages and to compare mutants with the wild type. Raman spectra obtained from transect measurements show only small differences between sepals in stages 10 and 12 or between the wild type and mutants. They are mainly manifested by small changes in band intensities (**Fig. 4.1**). Therefore, to perform a more detailed analysis of spectral diversity, we used the MCR-ALS toolbox in MATLAB to distinguish so-called Component spectra for all the transect measurements. Based on the evaluation of eigenvalues, the number of Component spectra was set to two.

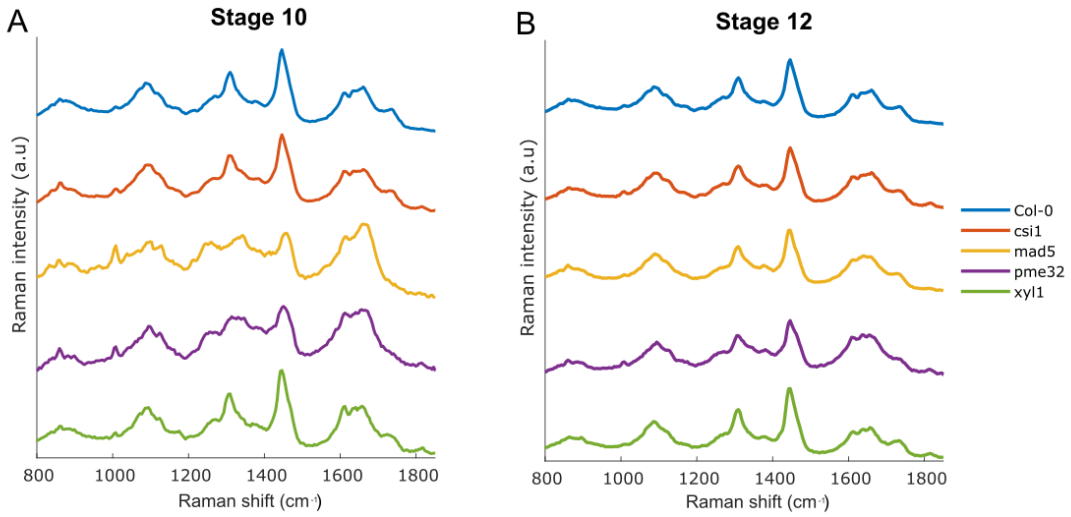

Fig. 4.1 Averaged Raman spectra of transect measurements for Col-0 and mutant sepals in developmental stages 10 **(A)** and 12 **(B)**.

Comparison of the Component spectra obtained using MCR-ALS reveals subtle differences between the examined cell walls. In both the wild type (**Fig. 4.2A-C**) and the mutants (**Fig. 4.3**), Component spectrum 1 identified for stage 10 is similar to that of stage 12, and the same applies to Component spectrum 2. For example, in Col-0, the Component spectra for stages 10 and 12 overlap by 98% for Component 1 and 96% for Component 2 (**Fig. 4.2C**). In the case of both stages, the difference between the Component spectra 1 and 2 is manifested by the presence in Component spectrum 1, of a band with a frequency of approximately 1740 cm^{-1}, associated with the stretching vibrations of the C=O bond (band XII marked with an asterisk in **Fig. 4.2**). These bonds occur in esters and can be attributed to pectins, hemicellulose and cutin (see **Table 4.3** in **4.1.2 Assignment of spectrum peaks to primary cell wall components of ridged and non-ridged portions of primary cell wall**). A difference between the two Components was also in different signal intensities, especially the intensity of the band at 1447 cm^{-1} (band VII in **Fig. 4.2A** and **B**), characteristic for deformation vibrations of the CH, stretching vibrations of C=C aromatic and deformation vibrations of CH_2 in esters (cutin) and esterified pectins (**Table 4.3**).

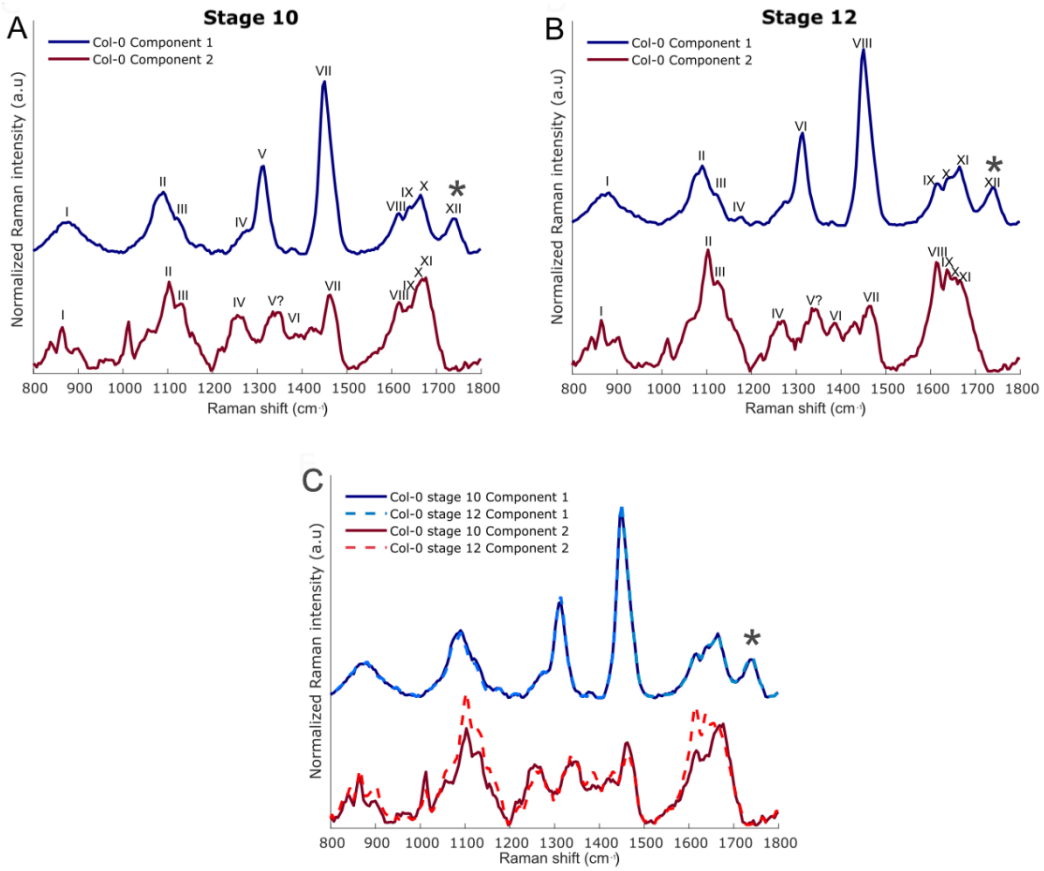

Fig. 4.2 Col-0 Component spectra obtained with MCR-ALS for sepals in stage 10 **(A)** and 12 **(B)**. The blue spectrum corresponds to Component 1; red represents Component 2, to which a smaller group of spectra are similar. The spectra are not overlaid in order to visualise potential differences between the two Component spectra in the same developmental stage. **(C)** shows overlaid spectra for Components of the two stages. An asterisk mark the Raman peak characteristic for Component 1. Roman numerals are used for band assignment; their wavenumbers and band identities are given in **Table 4.3**.

Despite the high similarity between the Component spectra of the two developmental stages, both in Col-0 and in mutants, the stages differ in the contribution of Components 1 and 2 to individual spectra (so-called component concentration profiles, see **Material and Methods**). Based on this information, we divided all the spectra of a given stage of each genotype into those that are more similar to Component 1 and those that are more similar to Component 2 (**Table 4.1**). Such analysis shows that in stage 10, in all the genotypes except for *xyl1*, the number of spectra similar to Component 1 and 2 are nearly the same. In *xyl1*, the spectra similar to Component 1 dominate at stage 10. In all the genotypes, the contribution of Component 1 increases in stage 12, while at the same time, the contribution of Component 2 decreases. This tendency is the strongest in Col-0 (Component 1 contribution increases from 101 to 159) and the weakest in *csi1*

(from 101 to 125). In *xyl1*, at stage 12, the domination of spectra similar to Component 1 is even higher than at stage 10.

Genotype	Stage 10		Stage 12	
	number of spectra similar to:			
	Component 1	Component 2	Component 1	Component 2
Col-0	101	99	159	41
csi1	101	99	125	75
mad5	101	99	154	46
pme32	102	98	150	50
xyl1	131	69	169	31

Table 4.1 Contribution of spectra similar to Component 1 or 2 identified using concentration profiles generated by MCR-ALS.

Next, we attempted to compare mutant Component spectra to wild type, using the Col-0 component spectra recognized in the two stages (**Fig. 4.2A** and **B**) as reference spectra (**Table 4.2; Fig. 4.3**). We then compared the mutant Component spectra with those of the wild type, using the Col-0 Component spectra identified at stages 10 and 12 (**Fig. 4.2A** and **B**) as reference spectra (**Table 4.2**; **Fig. 4.3**). The analysis shows that the Component spectra identified for mutant sepals of both the developmental stages are very similar to corresponding reference spectra of wild type. Except for the Component spectrum 2 of stage 12 *xyl1* sepals, there is at least 95% similarity between mutant and Col-0.

Genotype	Matching to Col-0 reference			
	Stage 10		Stage 12	
	Component 1	Component 2	Component 1	Component 2
csi1	98%	97%	99%	97%
mad5	97%	95%	97%	97%
pme32	98%	97%	99%	98%
xyl1	97%	97%	98%	92%

Table 4.2 Comparisons of Col-0 reference spectra to Component spectra obtained for the mutants. Matching of the mutant Component spectrum to the reference Col-0 spectrum is given in percent.

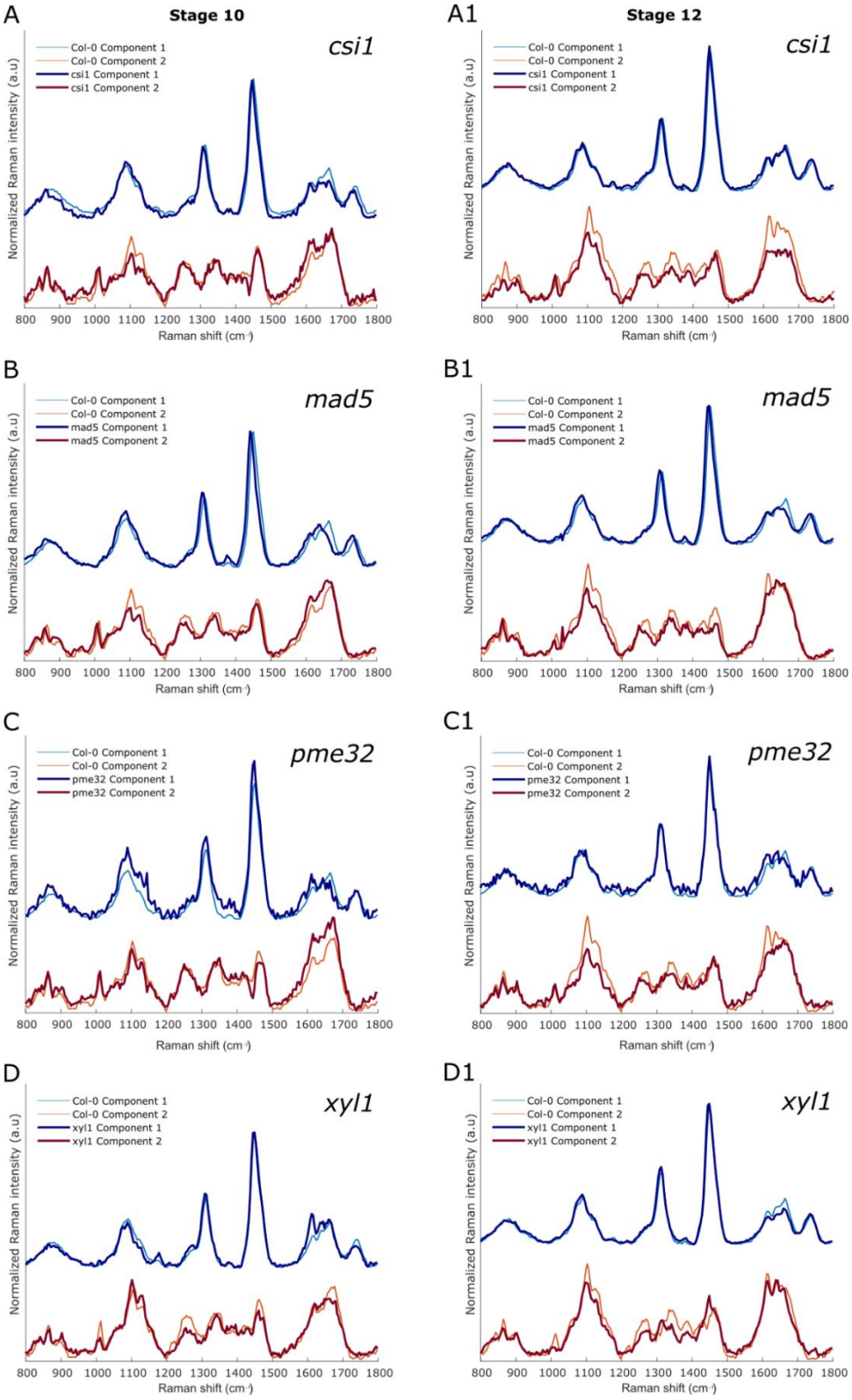

Fig. 4.3 Component spectra obtained with MCR-ALS for mutant sepals in stage 10 **(A-D)** and 12 **(A1-D1)**. The blue spectra correspond to Component 1, and red to Component 2. Reference spectra obtained from Col-0 are overlaid on those from the mutants to facilitate comparison.

Summarizing, Raman spectroscopy revealed subtle changes in primary cell wall composition during sepal maturation in wild type and mutants. Using MCR-ALS analysis restricted to two Components, the Component spectra of primary cell walls could be distinguished for each genotype and developmental stage. The Component spectra of mutants are similar to Col-0 spectra. In the case of younger sepals of all genotypes except for *xyl1*, concentration profiles of the two Component spectra are similar, while in mature sepals, the Component spectrum 1 dominates.

4.1.2 Assignment of spectrum peaks to primary cell wall components of ridged and non-ridged portions of primary cell wall

Raman spectroscopy was also used to compare the chemical structure of primary cell walls in wild type and mutants at late stages of sepal development, by assigning spectral bands to specific cell wall compounds. This analysis was performed for 10 μm × 10 μm maps of central portions of cell walls. First, the maps were obtained by integrating CH band from 2898 – 2940 cm^{-1} (Gierlinger and Schwanninger 2007, Bock et al. 2021). In such maps, the pattern of cuticular ridges is apparent. The structure of cell wall fragments covered by ridges is more complex than that of cell walls without ridges (see **Fig. 4.4A-B**), and ridges are not always parallel to the laser beam (Transmission Electron Microscopy micrograph in **Fig. 4.4B**). Moreover, because the primary cell walls are thin, the cubes used during Raman measurements include either the ridge and the underlying cell wall (black square in **Fig. 4.4**) or the cell wall portion covered with cuticle without ridges. This explains why the Raman signal that comes from the ridged wall fragments is stronger (**Fig. 4.5A**). Based on this difference, two clusters were distinguished within each 10 μm x 10 μm map using *K*-means clustering: the first cluster corresponds to the cell wall fragments located between cuticular ridges (red in **Fig. 4.5B**), and the second to the wall fragments covered by ridges (blue in **Fig. 4.5B**). For these clusters, further referred to as non-ridged and ridged clusters, respectively, specific spectra were extracted (**Fig. 4.5C**). The same analysis was performed for the cell walls of wild type and mutants (**Fig. 4.5**). There are only small differences between the spectra obtained from the examined genotypes, and they are in signal intensity rather than in band occurrence or absence (see **Fig. 4.6**).

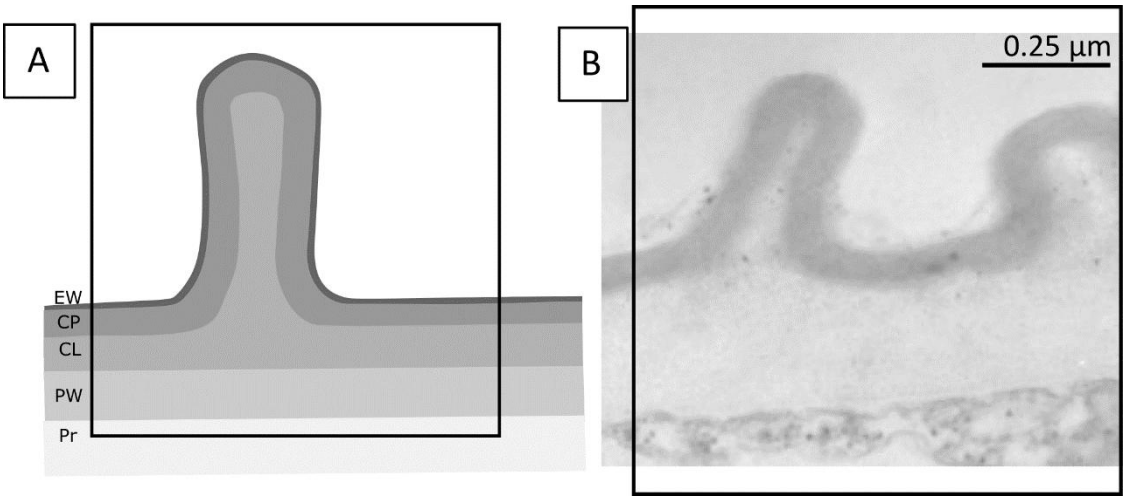

Fig. 4.4 (A) Scheme of cross-section of outer periclinal wall of Arabidopsis sepal epidermis, based on micrographs obtained using TEM **(B)**. Note that the cuticle proper is folded. Labels: epicuticular waxes (EW); cuticle proper (CP); cuticular layer (CL); non-cutinized primary wall (PW); and cell protoplast (Pr). The black square outlines a section of a cube used in Raman spectroscopy measurements. The laser polarisation plane is vertical. (A – based on Skrzydeł et al. 2021, modified; B – by courtesy of Dr. Dorota Borowska-Wykręt).

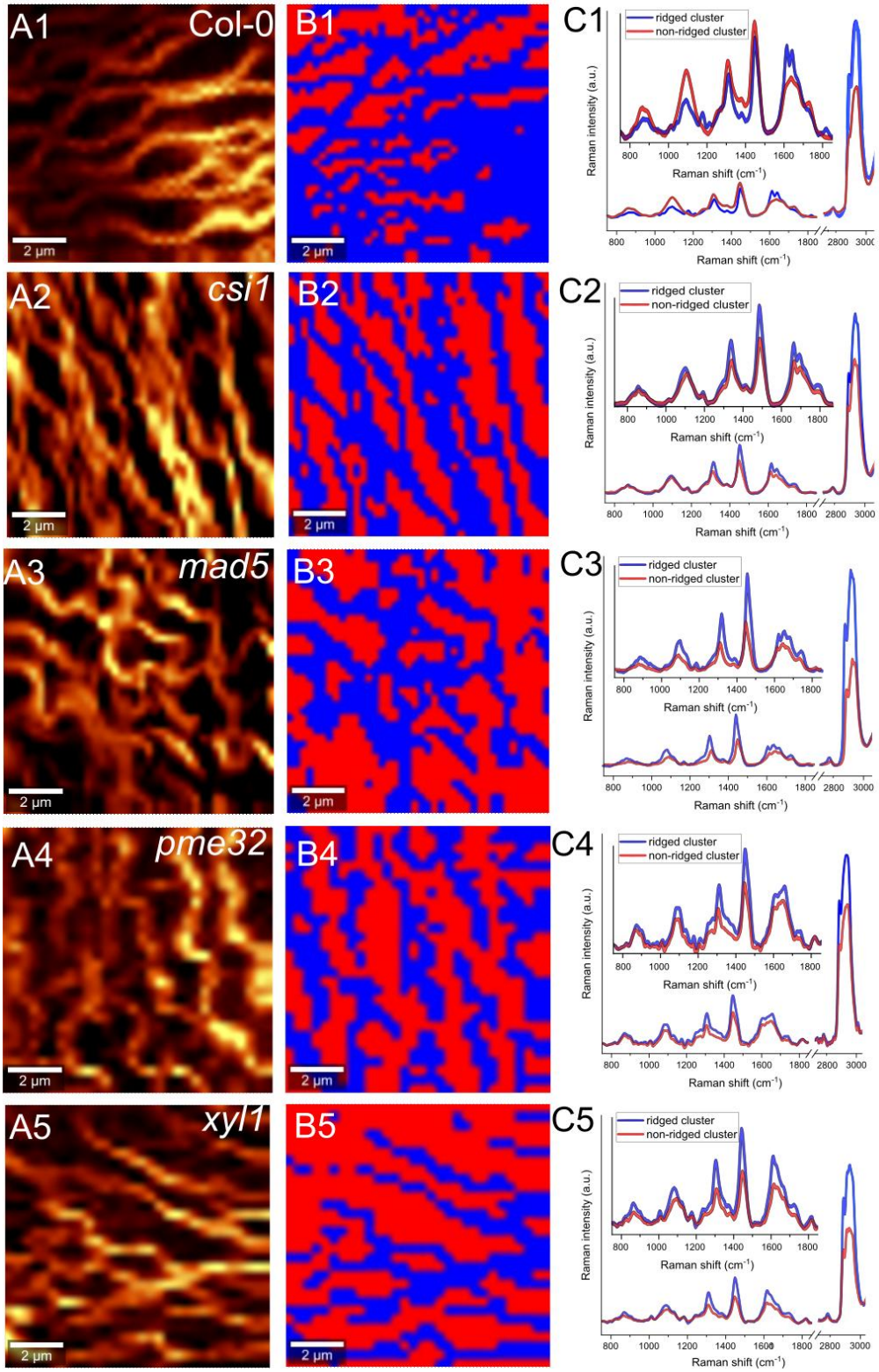

Fig. 4.5 (A) Exemplary Raman images of the abaxial epidermis of stage 12 sepal surface obtained by integrating from 2898-2940 cm^{-1} corresponding to CH stretching bond, **(B)** corresponding *K*-means clustering of Raman images shown in **(A)** using Manhattan distance, based on similarities between spectra. Blue cluster corresponds to the cell wall covered with cuticular ridges (ridged cluster), red – to non-ridged portion (non-ridged cluster). **(C)** averaged spectra corresponding to the ridged (blue) and non-ridged (red) clusters. The spectrum portion in the inset was used for further analysis. A, B, C are followed by numbers which correspond to different genotypes: 1 - Col-0, 2 - *csi1*, 3 - *mad5*, 4 - *pme32*, 5 - *xyl1*.

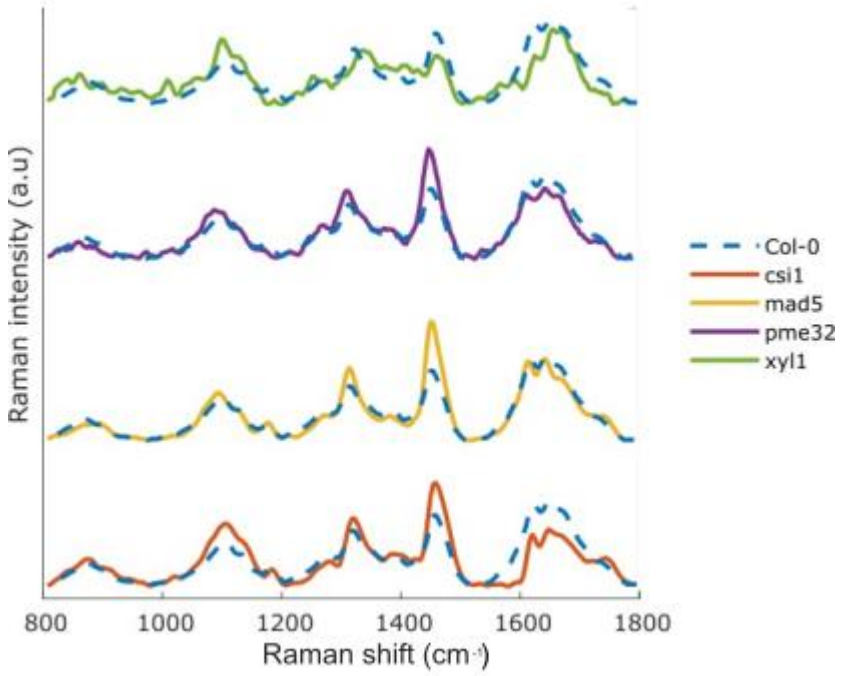

Fig. 4.6 Exemplary spectra of non-ridged wall regions of Col-0 (blue dashed line) overlaid on those of mutants to facilitate comparisons.

A more advanced *K*-means cluster analysis was also attempted to reveal differences between Col-0 and mutants, which includes the subtraction procedure where the ridged spectrum is subtracted from the non-ridged spectrum to reveal bands specific to the wall spectrum and *vice versa* (**Fig. 4.7**). However, the noise for the non-ridged spectrum after subtraction of the ridged spectrum was too high for meaningful analysis.

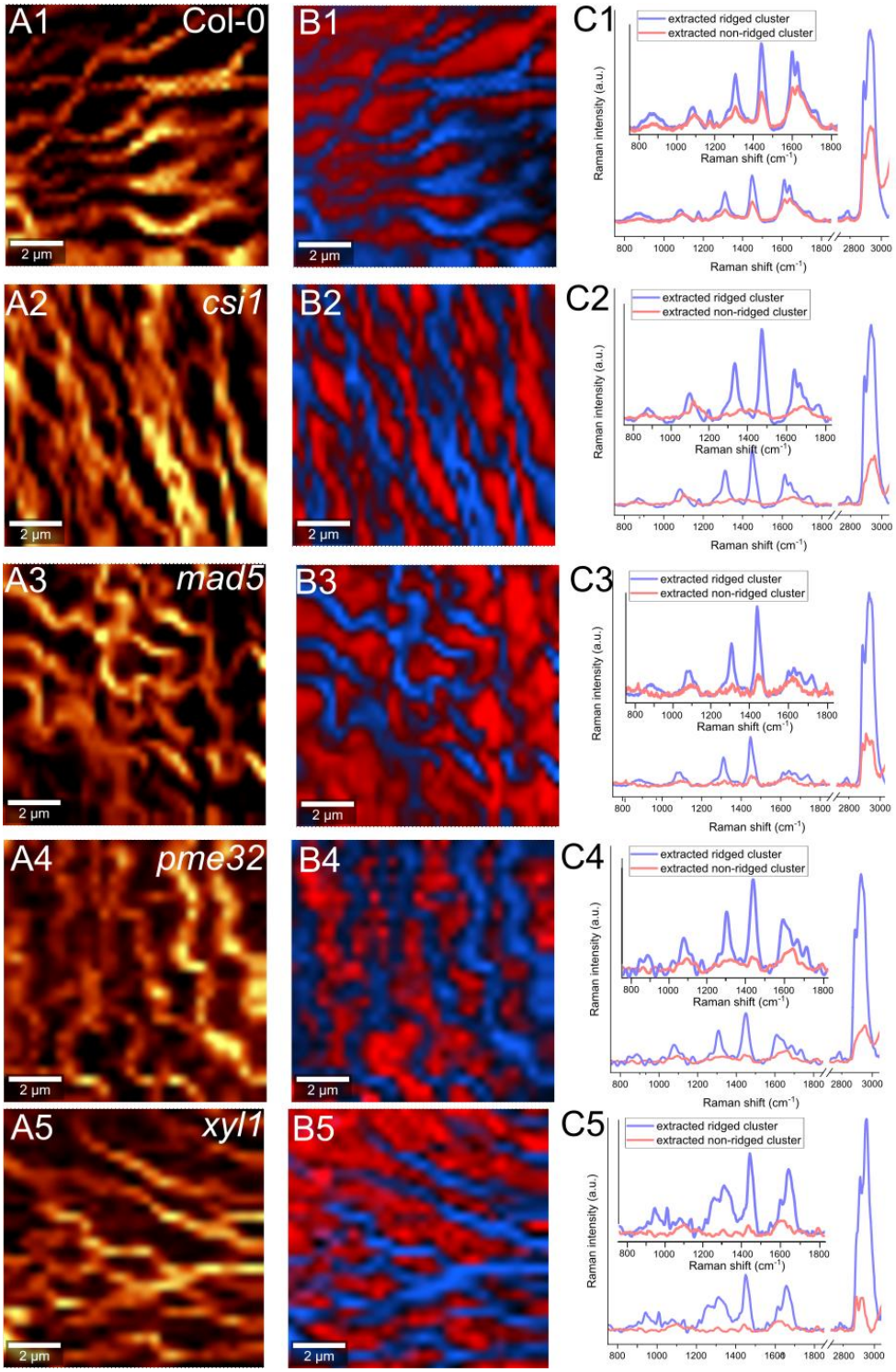

Fig. 4.7 Alternative method for analysis of Raman spectra of the same images as shown in **Fig. 4.5**. **(A)** Exemplary Raman images obtained by integrating from 2898-2940 cm^{-1} corresponding to CH stretching bond, **(B)** K-means clustering of Raman images shown in **(A)** using Euclidean distance, shading is based on the correlation between the intensity, similarity of the spectra and their morphology. Blue cluster corresponds to the cell wall covered with cuticular ridges, red – to non-ridged portion. **(C)** Spectra after subtraction: the light blue spectrum represents values for the ridged cluster from which the spectrum of the non-ridged cluster was subtracted, and *vice versa* for the light red spectrum. A, B, C are followed by numbers, which correspond to different genotypes: 1 - Col-0, 2 - *csi1*, 3 - *mad5*, 4 - *pme32*, 5 - *xyl1*.

Next, based on the literature data, peaks of averaged spectra of both non-ridged and ridged clusters were assigned to the specific functional group of cell wall polysaccharides or cuticle components. For Col-0, *mad5*, *pme32* and *xyl1* sepals, Raman spectra of the non-ridged clusters show 12 peaks that can be assigned to bands related to cell wall components, while there are 11 such peaks in *csi1* (**Table 4.3**). The band that is missing in *csi1* samples is at 1594 cm^{-1} in Col-0 and describes the stretching of the CC bond in phenolic compounds of cutin. In the spectra of the ridged clusters, 14 bands can be identified in all the lines. Spectra from both the non-ridged and ridged clusters include the band around 856 cm^{-1} corresponding to α-glycosidic bonds in pectins, which link galacturonic acid groups (Synytsya et al. 2003, Gierlinger and Schwanninger 2007). Although characterised by a relatively low signal intensity, this band occurs in spectra from every genotype. It indicates that pectins are found both in the cell wall covered by a nearly flat cuticle (non-ridged portion) and in the regions covered by cuticular ridges. Other bands, which were assigned to bonds characteristic for cellulose, hemicellulose, pectins and cutin (i.e. 1098, 1127, 1260, 1310, 1385, 1447, 1613, 1639, 1660, and 1737 cm^{-1}) were also detected in all of the spectra, in both non-ridged and ridged clusters. The cellulose and hemicellulose can be difficult to separate due to strongly overlapping bands (Gierlinger et al. 2008, Zeng et al. 2016), except for the δ(COH) vibration characteristic for xylan chains (assigned to C3-OH) located at 1313 cm^{-1} (Zeng et al. 2016). This band was detected in both non-ridged and ridged clusters. In the spectrum of the non-ridged cluster of *xyl1*, a minor shift to 1338 cm^{-1} was observed, which may suggest a different structure of xylan chains in the mutant. However, this shift occurred only in 2 out of 10 measured samples.

No	Non-ridged cluster					Ridged cluster					Component	Bond	Source
	Genotype					Genotype							
	Col-0	*csi1*	*mad5*	*pme32*	*xyl1*	Col-0	*csi1*	*mad5*	*pme32*	*xyl1*			
I	863	856	861	864	864	858	861	858	848	858	Pectins,	ν(C-O-C) asym, α-glycosidic bond	(Stephens 1984, Séné et al. 1994, Synytsya et al. 2003, Gierlinger et al. 2008)
II	1098	1106	1090	1098	1101	1089	1088	1080	1089	1089	Cellulose	ν(CO), ν(CC), ring, $\nu(COC)_{asym}$	(Marchessault and Sundararajan 1983, Agarwal and Atalla 1986, Agarwal and Ralph 1997, Gierlinger et al. 2008, Mateu et al. 2016)
III	1127	1128	1123	1122	1129	1119	1124	1114	1125	1119	Cellulose, Hemicellulose	ν(CO), ν(CC), ring, $\nu(COC)_{sym}$	(Marchessault and Sundararajan 1983, Agarwal and Atalla 1986, Agarwal and Ralph 1997, Gierlinger et al. 2008)
-						1172	1171	1167	1167	1172	Cellulose, Hemicellulose, Cutin, Phenolic compounds	δ(C-O-C) ring, ν(CO)	(Marchessault and Sundararajan 1983, Agarwal and Atalla 1986, Agarwal and Ralph 1997, Gierlinger et al. 2008; Mateu et al. 2016)
-						1240	1249	1247	1241	1240	Pectins, Hemicellulose, Phenolic compounds	δ(CH), δ(COH), ν(CO), δ(OH), ν(CC)	(Kacurakova et al. 1999, Gierlinger et al. 2008, Bichara et al. 2016)
IV	1260	1268	1271	1267	1272	1264	1267	1264	1260	1264	Hemicellulose	δ(CH), δ(COH), ν(CO), ν(CC)	(Faix 1991, Gierlinger *et al.* 2008, Chylińska et al. 2014)
V	1310	1318	1311	1308	1338	1305	1305	1310	1308	1305	Hemicellulose	δ(CH), δ(COH)	(Kacurakova et al. 1999, Zeng et al. 2016)
VI	1385	1387	1381	1377	1380	1375	1376	1368	1370	1375	Pectins, Cellulose	δ(CH2), ν(CC), ν(HCC), δ(HCO)	(Marchessault and Sundararajan 1983, Gierlinger and Schwanninger 2006)
VII	1447	1453	1446	1444	1462	1442	1442	1437	1445	1442	Pectins, Ester (cutin)	δ(CH), ν(C=C) aromatic (conjugated with C=C), $\delta(CH_2)$	(Séné et al. 1994, Ramirez et al. 1992, Mateu et al. 2016)
-	1594	X	1590	1581	1593						Phenolic compounds	ν(C=C) aromatic	(Ramirez et al. 1992, Heredia-Guerrero et al. 2014)

VIII	1613	1620	1611	1609	1626	1610	1609	1606	1614	1610	Water, Phenolic compounds	δ(HOH), ν(C=C) phenolic acid	(Séné et al. 1994, Gierlinger and Schwanninger 2007, Heredia-Guerrero et al. 2014)
IX	1639	1647	1638	1640	1644	1636	1634	1634	1639	1636	Cutin	Ring conjugated ν(C=C) of coniferyl alcohol; ν(C=O) of coniferaldehyde	(Gierlinger and Schwanninger 2007, Bock et al. 2021)
X	1660	1668	1664	1665	1669	1660	1660	1658	1659	1660	Cutin	Ring conjugated ν(C=C) of coniferyl alcohol; ν(C=O) of coniferaldehyde	(Bonaventure et al. 2004, Gierlinger and Schwanninger 2007)
XI						1678	1679	1675	1674	1678	Cutin	Ring-conjugated ν(C=C) of coniferyl alcohol; ν(C=O) of coniferaldehyde, ν(C=O···H strong) acid	(Gierlinger and Schwanninger 2007, Schmidt et al. 2009, Heredia-Guerrero et al. 2014)
XII	1737	1741	1742	1743	1739	1736	1730	1729	1742	1736	Pectins, Cutin, Hemicellulose	ν(C=O) ester	(Marchessault and Sundararajan 1983, Séné *et al.* 1994, Ramirez et al. 1992, Gierlinger and Schwanninger 2007, Heredia-Guerrero et al. 2014, Mateu et al. 2016)

Table 4.3 Band assignment of spectra from non-ridged and ridged clusters of Col-0 and mutant Arabidopsis sepal samples. All values are given in wavenumbers (cm^{-1}). δ – deformation, ν – stretching, asym – asymmetric, sym – symmetric. Roman numerals in the first column refer to band labels in **Fig. 4.2**.

Spectra obtained from the non-ridged cluster are similar to the ridged cluster spectra in all of the examined lines. However, it must be kept in mind that due to the small thickness of the primary cell wall in relation to the resolution of Raman measurements (**Fig. 4.4**), the separation of the cell wall and cuticle during the measurements was impossible. The only difference between non-ridged and ridged clusters was that in all the samples except for *csi1*, the non-ridged cluster has an extra band at 1594 cm^{-1}, which indicates phenolic compounds in the cuticle (stretching (CC) aromatic (Ramirez et al. 1992, Heredia-Guerrero et al. 2014)), while band at 1678 cm^{-1} related to cutin is detected only in the ridged cluster. This may mean a specific composition of cuticle covering the wall portions devoid of ridges, but may also be caused by a different orientation of the cuticle proper with respect to the laser beam in the two clusters. Namely, measurements for cuticle proper covering ridges are performed in a direction oblique or nearly parallel to the laser beam, except for the ridge tip (see **Fig. 4.4**). Analysis of TEM micrographs (see **Fig. 4.4B**) suggests that sepal ridges are built not only of cutin and waxes but also contain a pectin-rich core likely with embedded cellulose microfibrils. In spectra from the ridged cluster, this is manifested by the presence of bands at 1172 cm^{-1} and 1240 cm^{-1}, which are related to all of the wall components.

4.1.3 Structural anisotropy of primary cell walls of Arabidopsis sepal

By performing measurements of motionless samples at various angles of the laser polarisation plane, Raman spectroscopy can be used to analyse the extent of alignment of some wall components, i.e. structural anisotropy. Therefore, Raman measurements of primary cell walls of the sepal epidermis were performed for different orientations of polarisation plane in order to identify components sensitive to the orientation of polarisation plane. Only the non-ridged cell wall cluster of the 10 µm × 10 µm maps was used in this analysis in order to avoid a misinterpretation related to the shape of the cuticle proper that covers ridges. Changes in signal intensity related to the orientation of the polarisation plane are apparent in two regions of the spectrum (**Fig. 4.8**). One region includes the band around 1098 cm^{-1} related to the glycosidic bond (C-O-C) linking the glucose monomers, which represents asymmetric stretching vibrations within C-O-C (marked by blue arrow in **Fig. 4.8**). It is close to the second band, around 1122 cm^{-1}, which is not sensitive to orientation of polarisation plane and describes symmetric

stretching vibrations within C-O-C (blue asterisk in **Fig. 4.8**) (Marchessault and Sundararajan 1983, Agarwal and Atalla 1986, Agarwal and Ralph 1997, Gierlinger et al. 2008, Mateu et al. 2016). The second polarisation-sensitive region, between 1500-1700 cm^{-1}, is related to stretching vibrations in ring conjugated bonds C=C of coniferyl alcohol and C=O of conifer aldehyde characteristic for cuticle components. It includes the C=C stretching vibration bands with a frequency of approximately 1639 cm^{-1}, 1660 cm^{-1}, 1678 cm^{-1} (Bock et al. 2021) specific to the components of the Arabidopsis cuticle, which are sensitive to the polarisation plane orientation (red arrow in **Fig. 4.8**). They are close to the band independent of the polarisation orientation at around 1739 cm^{-1}, related to stretching vibrations in the C=O bond in esters characteristic of pectins, cutin and hemicellulose (red star in **Fig. 4.8**).

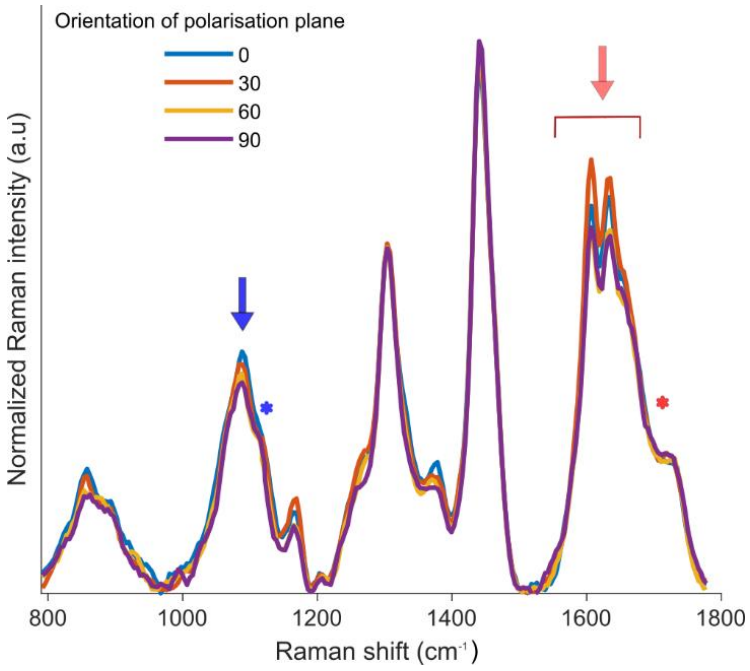

Fig. 4.8 Exemplary Col-0 cell wall spectra obtained for the same sample at different orientations of the polarisation plane (every 30° from 0° to 90°). The blue arrow points to the orientation-sensitive band for cellulose (1098 cm^{-1}), and the blue asterisk points to the non-sensitive band (1122 cm^{-1}); the red arrow points to the region including orientation-sensitive bands for cutin and waxes (1639 cm^{-1}, 1660 cm^{-1}, 1678 cm^{-1}); the red asterisk labels the non-sensitive band related to cutin, pectins, and hemicellulose (1736 cm^{-1}).

4.1.3.1 Alignment of cellulose microfibrils

In order to assess the extent of alignment of cellulose microfibrils, signals of two bands was used: the orientation-sensitive band centered at about 1098 cm^{-1} and the orientation non-sensitive band at about 1122 cm^{-1} (**Fig. 4.9**). Although the latter band can also be found in the spectrum of xyloglucan (XyG) where the main backbone consists of β-1,4-linked glucose residues, the contribution of hemicelluloses to this band is considered to be rather small (Agarwal and Atalla 1986, Gierlinger and Schwanninger 2007). To assess dependence of the signal intensity of the orientation of polarisation plane, the integrated intensity of orientation sensitive C-O-C band (1098 cm^{-1}; marked by blue arrow in **Fig. 3.3** in **Material and Methods**) was extracted and divided by the integrated intensity of the orientation non-sensitive band (1122 cm^{-1}; marked by a blue asterisk in **Fig. 3.3** in **Material and Methods**). The angle 0° was then assigned to the polariser orientation at the maximum signal intensity (**Fig. 4.9**). Polar plots were generated for the normalised ratio of cellulose-specific bands, where the surface area under the 1098 cm^{-1} band was divided by the area under the 1122 cm^{-1} band and normalised by the sum of such ratios over all polarisation angles (see **Fig. 4.10** for details). This procedure was performed for sepal cell walls of Col-0 and mutants, and for samples of amorphous and crystalline cellulose that were used as reference. For the amorphous cellulose (cellulose chains are non-aligned), the normalised ratio is constant across polarisation angles, while for crystalline cellulose (chains are aligned), the normalised ratio depends strongly on the polarisation angle (**Fig. 4.9**, **Fig. 4.10**). Polar plots of the normalised ratio highlight the differences of amorphous and crystalline cellulose (upper left corner of **Fig. 4.10**).

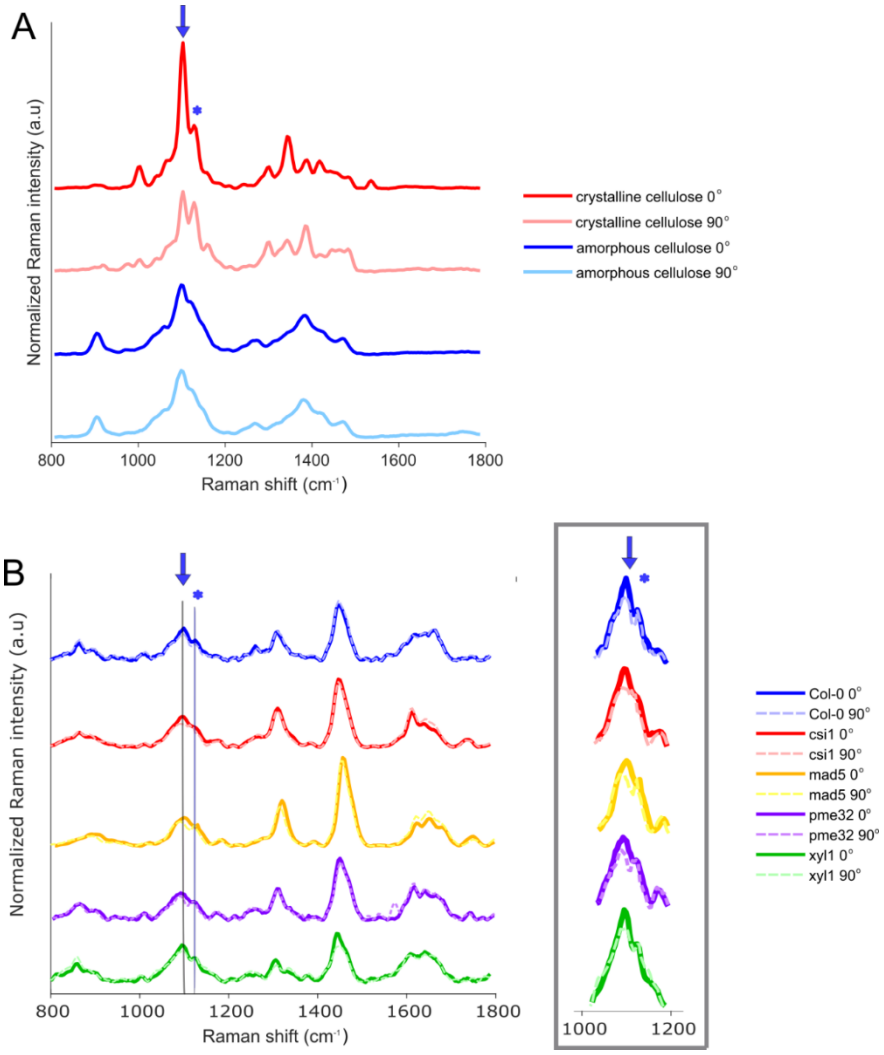

Fig. 4.9 (A) Reference spectra obtained from crystalline cellulose at maximum (0°) and minimum (90°) of 1098 cm^{-1} signal intensity, and from amorphous cellulose (polarisation insensitive). The blue arrow labels the band sensitive to the orientation of the polarisation plane in crystalline cellulose (1098 cm^{-1}), the blue star labels the non-sensitive band (1122 cm^{-1}). **(B)** Exemplary Col-0 and mutants spectra obtained for the non-ridged cluster at the maximum (polarisation plane at 0°) and minimum (90°) intensity of peak 1098 cm^{-1} signal. The inset (grey rectangle) shows a zoomed region, including the bands of interest.

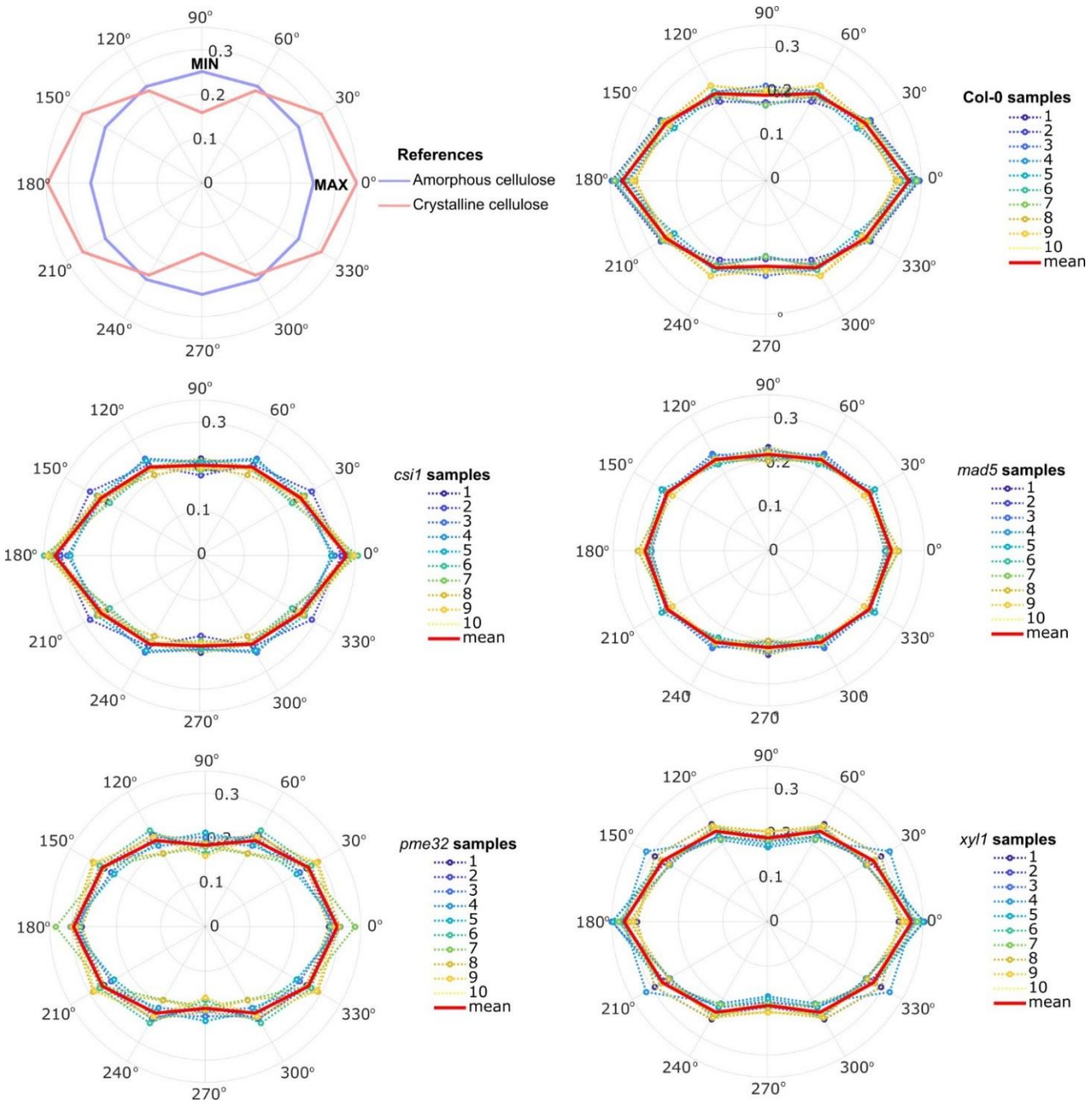

Fig. 4.10 Polar plots of the normalised ratio of cellulose-specific bands (surface area under the 1098 cm^{-1} band was divided by the area under the 1122 cm^{-1} band and normalised by the sum of such obtained values at all the orientations) plotted against the orientation of the polarisation plane for reference samples and sepal cell walls. Values from 0° to 90° were repeated to 360° to show periodicity. Red solid lines show mean values of the normalised ratio, and dotted lines represent individual measurements for each genotype.

Polar plots for all the cell wall samples show the angular dependence of the normalised band intensity on the polarisation direction. The extent of elongation of polar plot shape along the 0-180° axis is much weaker in the case of the cell wall than the crystalline cellulose, but differs from the circular shape observed for amorphous cellulose. It was therefore attempted to approximate the normalised ratio values of the wall by a sum of ratios of the two references at a given angle (cell wall normalised ratio = CoefA x amorphous cellulose normalised ratio + CoefB x crystalline cellulose normalised ratio), using the Least-Squares method (**Fig. 4.11**). It was assumed that such obtained coefficients would represent the contribution of crystalline (CoefB) and amorphous (CoefA) cellulose, and the coefficient ratio (CoefA/CoefB) computed for samples coming from different mutants was compared with those from Col-0 (**Fig. 4.12**). Those data were then subjected to statistical analysis, which showed no statistically significant differences between Col-0 and *csi1*, or *pme32*, or *xyl1*. Only the median coefficient ratio of *mad5* samples is significantly different from Col-0. The higher value of the coefficient ratio for this mutant means that, in terms of cellulose organisation, it is more similar to amorphous cellulose than other lines. This is further confirmed by comparison of the normalised ratio value for the orientation plane at 90° (minimal) divided by value at 0° (maximal) that again is significantly different from Col-0 only in the case of *mad5* samples (**Fig. 4.13**).

References

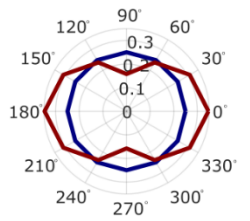

Amorphous cellulose
Crystalline cellulose

Sample values + the best fit

Coef A = 0.54
Coef B = 0.44

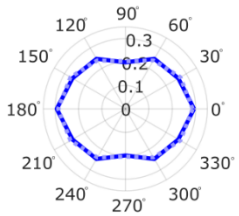

Col-0 Sample 1
Corresponding LS fitting

Coef A = 0.25
Coef B = 0.71

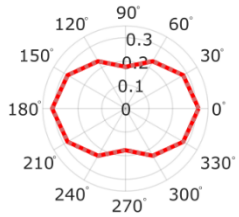

csi1 Sample 1
Corresponding LS fitting

Coef A = 0.78
Coef B = 0.20

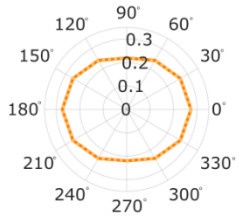

mad5 Sample 1
Corresponding LS fitting

Coef A = 0.37
Coef B = 0.61

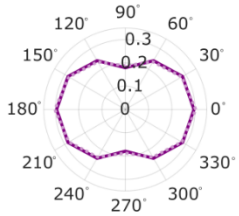

pme32 Sample 1
Corresponding LS fitting

Coef A = 0.46
Coef B = 0.51

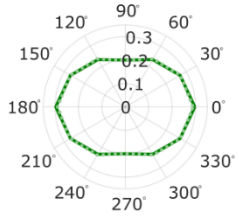

xyl1 Sample 1
Corresponding LS fitting

Sample values + the worst fit

Coef A = 0.27
Coef B = 0.68

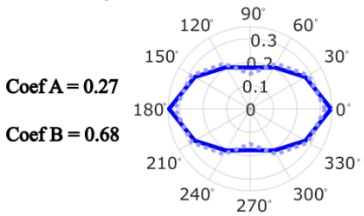

Col-0 Sample 2
Corresponding LS fitting

Coef A = 0.19
Coef B = 0.75

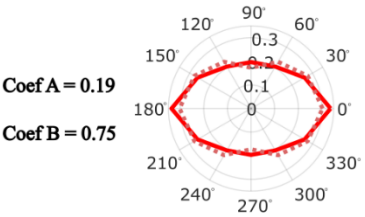

csi1 Sample 2
Corresponding LS fitting

Coef A = 0.68
Coef B = 0.29

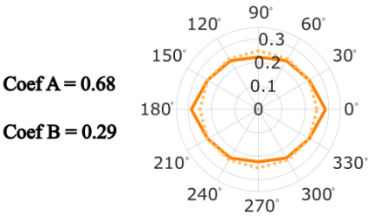

mad5 Sample 2
Corresponding LS fitting

Coef A = 0.20
Coef B = 0.77

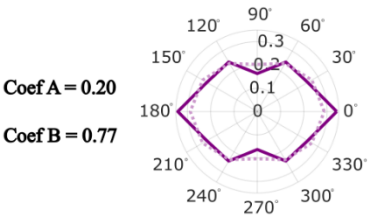

pme32 Sample 2
Corresponding LS fitting

Coef A = 0.35
Coef B = 0.61

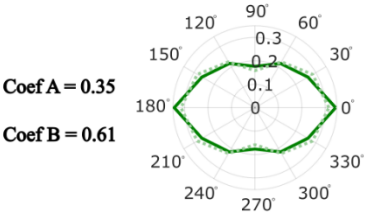

xyl1 Sample 2
Corresponding LS fitting

Fig. 4.11 Polar plots of the normalised ratio of cellulose-specific peaks plotted against the orientation of the polarisation plane. Values from 0° to 90° were repeated to 360° to show periodicity. Plot for the reference celluloses, amorphous and crystalline, is followed by exemplary samples of Col-0 and mutants, where dotted lines show approximations of original polar plots by a sum of references obtained using the Least-Squares method (see **Material and Methods**). Coefficient values are given for each example, where CoefA represents similarity to amorphous cellulose and CoefB - to crystalline cellulose. Examples of samples with the best and the worst fit (selected from all of the examined samples of a genotype) are shown for each genotype.

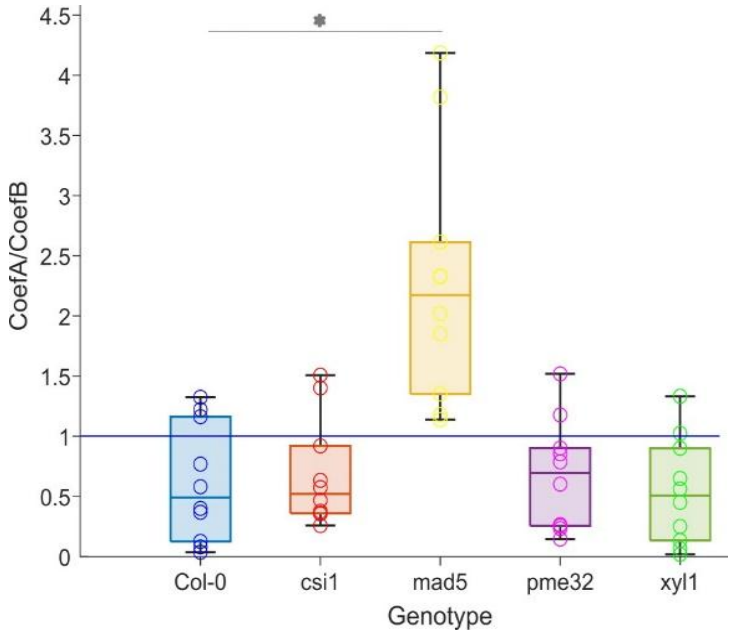

Fig. 4.12 Ratio of coefficients (CoefA/CoefB) describing the contribution of amorphous (CoefA) and crystalline (CoefB) cellulose for all samples from different genotypes. Only the median for *mad5* is significantly different from Col-0 (asterisk; statistically significant difference of pairwise comparison of *mad5* with Col-0, p-value of Mann-Whitney test is 0.005; for all the other pair-wise comparisons $p > 0.05$; $N = 10$ for each genotype). A coefficient ratio higher than 1 represents higher similarity to amorphous than to crystalline cellulose. The boxes show the interquartile range of the data; the line inside the box represents the median; whiskers show the range of the data. Circles represent coefficient ratios for individual samples.

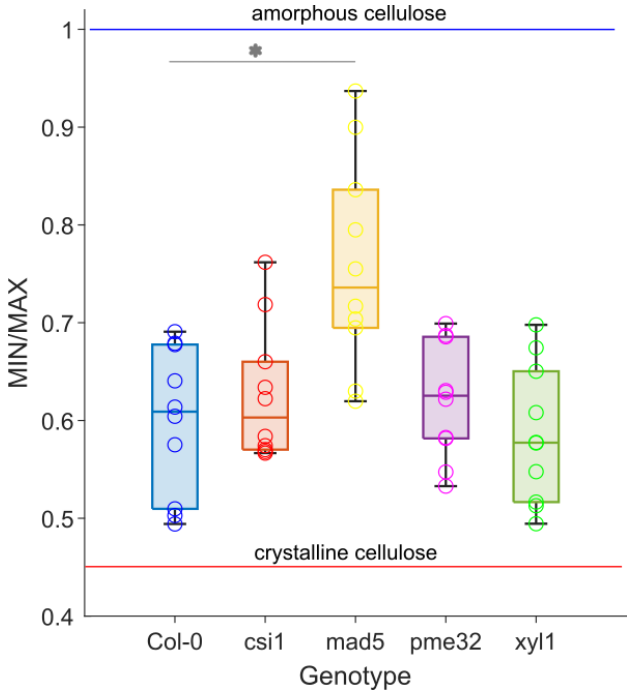

Fig. 4.13 Ratio of minimum (at polariation angle 90°) to maximum (0°) normalised signals for individual samples of Col-0 and mutants (N = 10 for each genotype), and for reference cellulose samples. The ratios of cellulose-specific normalised signals for individual samples are marked as circles, blue and red lines point to values obtained for references: blue - amorphous cellulose and red - crystalline cellulose. Only ratios for *mad5* are significantly different from Col-0 (asterisk; statistically significant difference of pairwise comparison of *mad5* with Col-0; p-value for Mann-Whitney test is 0.009; for all the other pair-wise comparisons $p > 0.05$). See **Fig. 4.12** legend for further explanations.

4.1.3.2 Aligned cuticle components

Similar analysis was performed for orientation-sensitive spectrum fragments related to cuticle components, localized between the 1500-1700 cm^{-1} region (pointed by the red arrow in **Fig. 4.8**, see also **Fig. 3.3** in **Material and Methods**). To assess signal dependence on the orientation of the polarisation plane, the surface area under sensitive bands in the range 1500-1700 cm^{-1} was extracted and divided by the surface area under the non-sensitive band at 1737 cm^{-1}. Then the normalised ratio was computed as explained above for the cellulose. To perform this analysis, angle 0° was assigned to the maximum normalised ratio for the cuticle. Noteworthy, it was usually not the same polariser orientation as defined earlier for the maximum of cellulose signal. Such obtained polar plots of the normalised ratio show that the signal changes with the orientation angle in a similar way in all the samples (**Fig. 4.14**). Accordingly, the minimal normalised ratio (orientation plane at 90°) divided by the maximal ratio (at 0°)

is similar for all the lines (no mutant samples are significantly different from Col-0; **Fig. 4.15**). These results suggest that in all the Arabidopsis genotypes examined, some lipid components of sepal cuticle are aligned, adding an additional level of structural anisotropy of the sepal cell walls. This interpretation should be taken with caution, given the complexity of the 1500–1700 cm^{-1} bands and the unknown depolarisation ratios of its component signals.

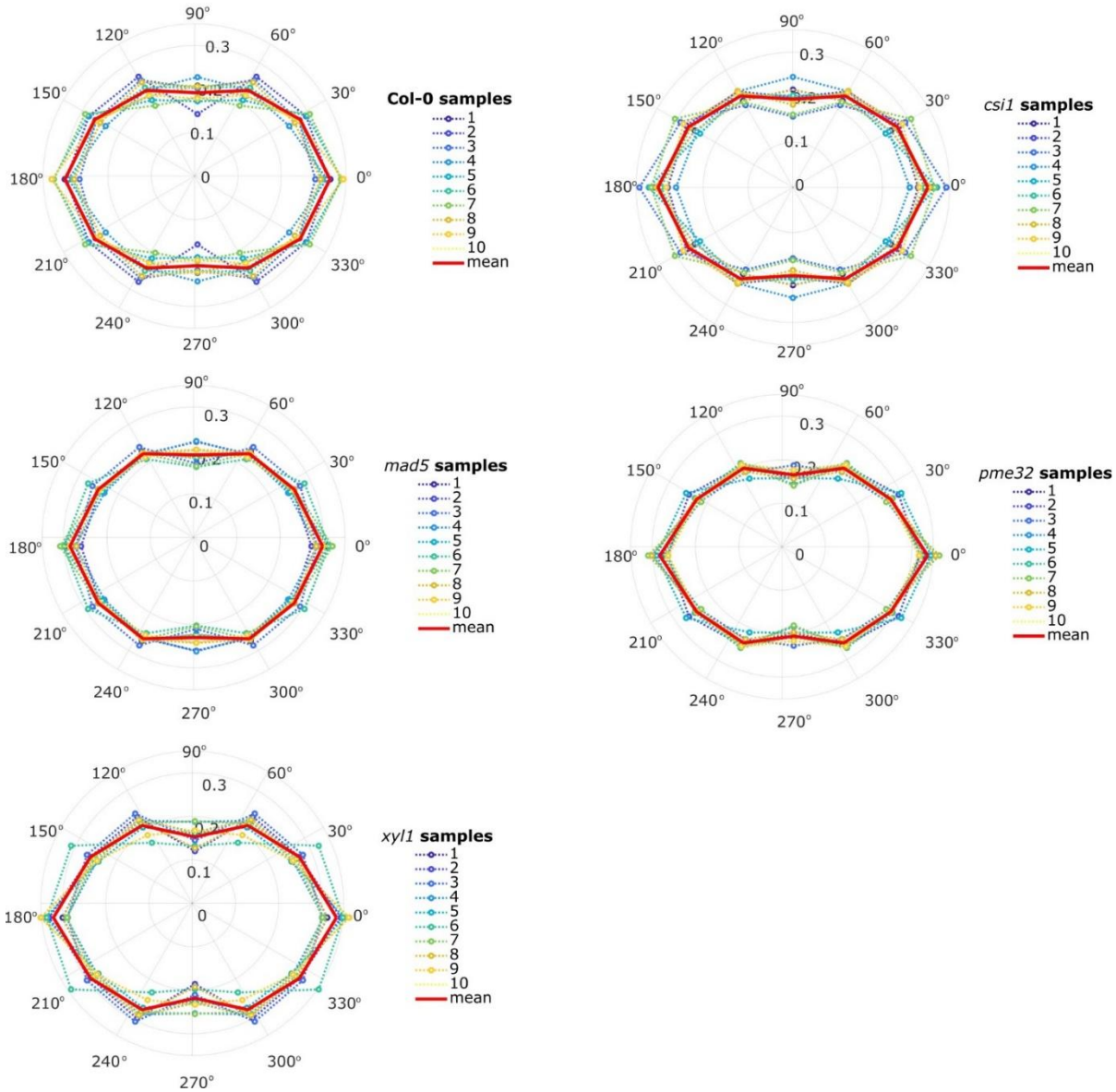

Fig. 4.14 Polar plots of the normalised ratio of cuticle component signals (surface area under bands at 1550-1700 cm^{-1} divided by area under band around 1737 cm^{-1} and normalised by the sum of values at all the orientations) plotted against the orientation of the polarisation plane. Mean values of the normalised ratio (solid red lines) and values for individual samples (dotted lines) are shown for each genotype.

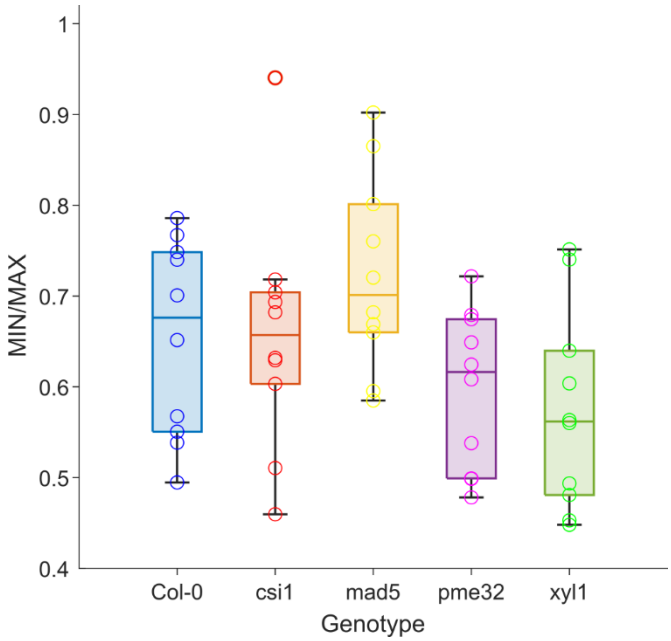

Fig. 4.15 Ratio of minimum (at polarisation angle 90°) to maximum (0°) normalised signals from cuticle components for Col-0 and mutants (N = 10 for each genotype). The ratios of cuticle-specific signals for individual samples are marked as circles. No significant differences between mutants and Col-0 were detected (pairwise comparisons using the Mann-Whitney test; $p > 0.05$). See **Fig. 4.12** legend for further explanations.

4.1.4 Compensatory effect of cell wall composition in mutants

Raman spectroscopy enables simultaneous assessment of the contribution of various compounds in the same cell wall sample. Thus, it facilitates the investigation of a putative compensatory effect (compensation), i.e. a phenomenon when the lack or reduction of one of the cell wall compounds is compensated by the overproduction of another (Vogler et al. 2015, Gigli-Bisceglia et al. 2020). To check if the compensation takes place in cell walls of mutant sepals the spectra with maximal signal intensity for the cellulose-related band around 1098 cm^{-1} were used (i.e. the spectra at orientation angle defined as 0° for the cellulose alignment analysis presented above), such that the intensity of the signal from cellulose can be compared between the genotypes. Three bands specific for the main cell wall polysaccharides were considered (see **Material and Methods, Fig. 3.3**): esterified pectins band around 856 cm^{-1} (Synytsya et al. 2003, Gierlinger and Schwanninger 2006, Gierlinger and Schwanninger 2007); cellulose band around 1098 cm^{-1} (Agarwal and Ralph 1997); and hemicellulose-specific band around 1313 cm^{-1} (Agarwal and Ralph 1997, Kacurakova et al. 1999). The sum of integrated intensity of these bands was assumed to be 100%. Such normalised band intensities

(relative signal contributions) do not reflect the relative content of wall components, but facilitate comparisons of calculated parameters between wild type and mutants.

In Col-0 and all the mutants, the lowest relative signal contribution is that of the pectin-specific band (e.g. 15.57% ± 1.25%, mean ± standard error for the Col-0), intermediate for the cellulose peak (32.13% ± 1.47%) and the highest for hemicellulose (52.3% ± 1.24%) (**Fig. 4.16A**). Pairwise comparisons of the relative signal contributions in mutants and Col-0 revealed some statistically significant differences (**Fig. 4.16A)**. In order to better visualize the differences between mutants and wild type, relative contributions in Col-0 were used as a reference and subtracted from those of mutants (**Fig. 4.16B**).

csi1 exhibits a significantly lower contribution of esterified pectin signal than Col-0 (-4.84% in **Fig. 4.16B**) while differences in cellulose and hemicellulose signals are insignificant. Cell wall samples of *mad5* do not present any statistically significant differences from Col-0. In *pme32* samples, the mutation leads to the statistically significant increase of the relative contribution of the esterified pectin band signal (+4.27% higher than in Col-0; **Fig. 4.16B**), and the significant increase in cellulose band signal (+7.9%). The way in which the relative contribution was calculated implies that the increase of pectins and cellulose signals in *pme32* samples has to be related to a decrease in the remaining component, i.e. the band characteristic for hemicelluloses (-15.15%). In the *xyl1* mutant, there is a significant decrease in hemicellulose signal contribution (-10.58%) and an increase in cellulose contribution (+8.45%).

To summarize, these results suggest the occurrence of a compensation phenomenon, whereby mutations induce compensatory responses as increased levels of some cell wall components compensate for deficiencies in others.

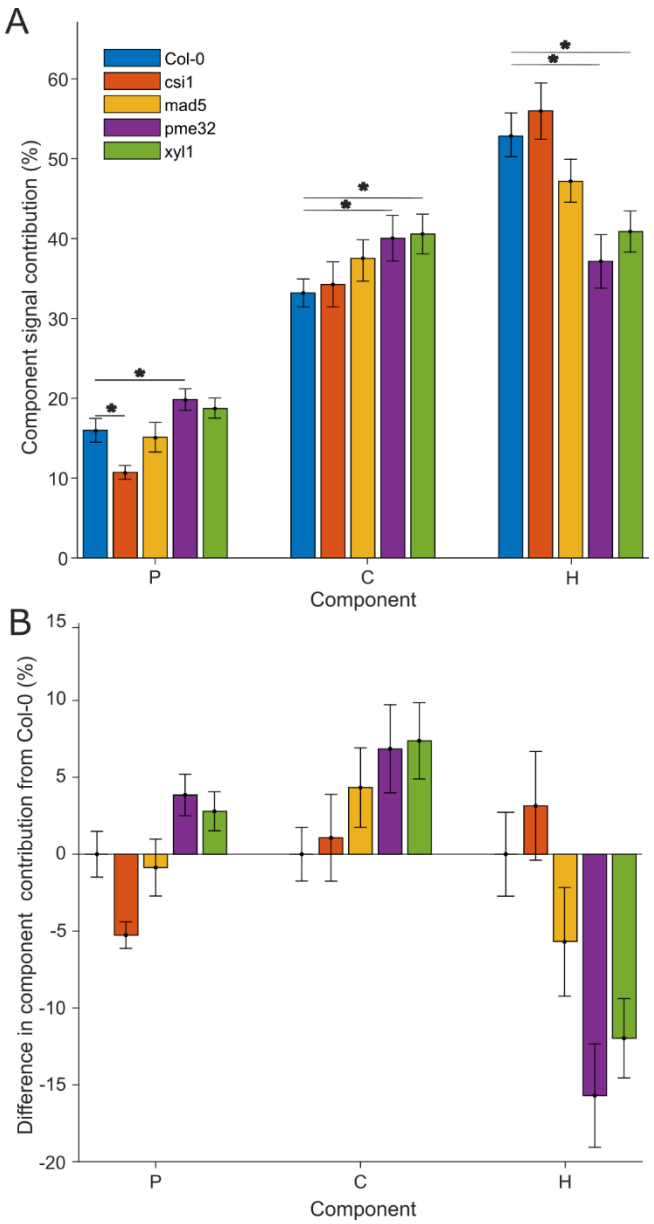

Fig. 4.16 (A) Relative signal contribution of bands specific for pectin (P), cellulose (C), and hemicellulose (H) in spectra of Col-0 and mutants. Asterisks point to statistically significant differences between Col-0 and mutants (in pairwise comparison of mutant to Col-0, p-values for Mann-Whitney test are: for pectins – Col-0 vs. *csi1* 0.017, Col-0 vs. *pme32* 0.021; for cellulose – Col-0 vs. *pme32* 0.045, Col-0 vs. *xyl1* 0.0003; for hemicellulose – Col-0 vs. *pme32* 0.009, Col-0 vs. *xyl1* 0.0002; other differences are not significant with $p>0.05$; $N = 10$ for each genotype). Bar heights represent median values for Col-0 and mutants. Whiskers represent the standard error. **(B)** Differences between contributions of the same band signals in mutants and Col-0. Bar heights represent the mutant value from which Col-0 value was subtracted. Whiskers represent the standard error.

4.2 Dynamic changes of cuticular pattern on the sepal cell wall surface

Raman spectroscopy facilitated investigations of the composition of superficial primary cell walls of Arabidopsis sepals. The investigations showed subtle changes in the wall composition during the final stages of the sepal development. These changes may be related to formation of cuticular ridges on the sepal surface, which is the topic of the present chapter.

First, the structure of cuticular ridges and general traits of the cuticular pattern were examined using Transmission Electronic Microscopy (TEM) and Scanning Electron Microscopy (SEM). Observations of cross sections of the cell wall covered with cuticular ridges in TEM (**Fig. 4.17A, B**) reveal that ridges consist of three layers: the cuticular layer (labelled as CL in **Fig. 4.17A**) covered by the cuticle proper (CP) and the thin top layer of epicuticular waxes (EW). The shape of ridges can be quite complex, i.e. the folds formed on the cell wall surface can branch and bend (see ridges marked by asterisk in **Fig. 4.17B)**. Observations of sepals in SEM were performed in order to visualize the surface of epidermal cells at consecutive developmental stages (**Fig. 4.17C–F**). They confirmed the earlier reports (Hervieux et al. 2016) that cuticular pattern first appears on the cell surface on the tip of the sepal and during the organ development the frontier between the surface covered and devoid of cuticular ridges progresses basipetally. SEM imaging also showed the shape diversity of ridges, which vary from nearly straight to strongly waved (compare e.g. cells on left and right in **Fig. 4.17G).**

Among all of the analysed genotypes, *mad5* mutant exhibits the strongest phenotype in terms of sepal morphology and growth. Sepals of *mad5* are smaller and buds open earlier than in Col-0 (Trinh et al. 2024), before the generative flower organs are fully developed. Also giant cells in Col-0 are longer than in *mad5*, and the cuticular pattern on the *mad5* cell surface is more complex (compare **Fig. 4.17G** and **H**). Moreover, in Col-0, ridges are formed on the entire surface of the still closed flower bud while in *mad5* the flower bud opens while the ridges frontier is still progressing (**Fig. 4.17D**). Thus *mad5* was chosen for analysis of cuticular pattern in comparison to the wild type (Col-0).

To obtain comprehensive data on the development of the pattern of cuticular ridges, confocal microscopy was employed for *in vivo* imaging. Such confocal images were used to analyse the ridges formation and changes of cuticular pattern in time.

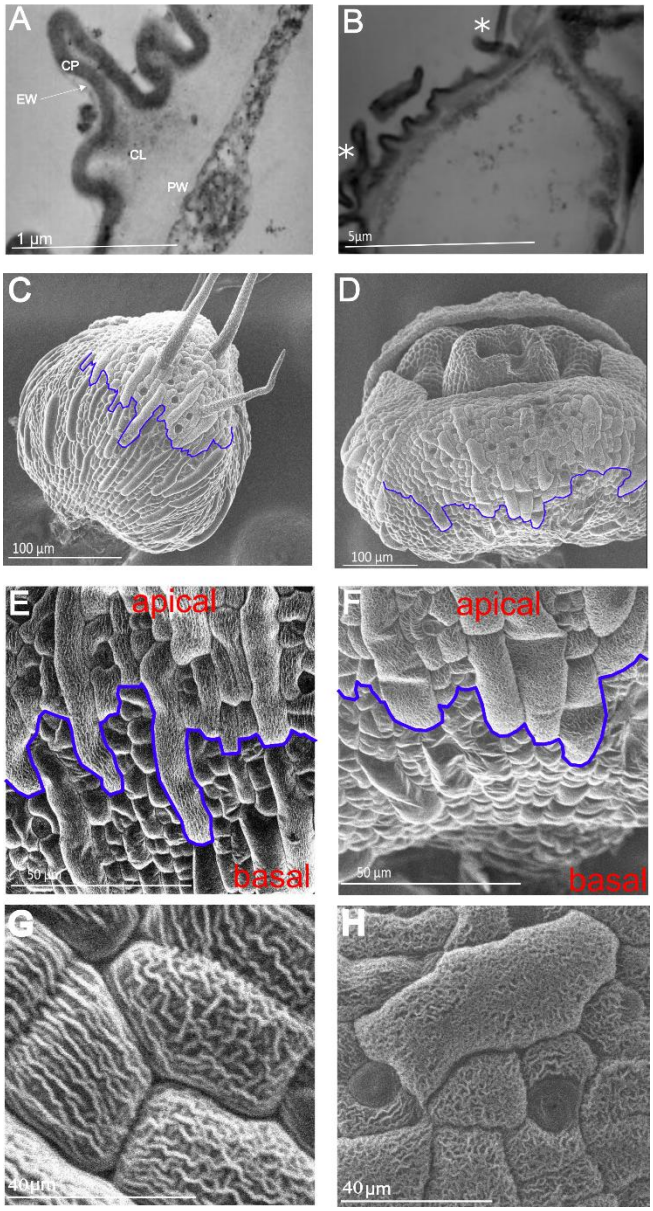

Fig. 4.17 (**A,B**) Exemplary TEM micrographs showing cross sections of outer periclinal wall of Col-0 sepal: section in plane transverse to sepal axis showing the cell wall layers: EW – epicuticular waxes, CP – cuticle proper, CL – cuticular layer, PW – primary cell wall **(A)** and section in plane parallel to sepal axis visualising bending and branching ridges, marked by white asterisks **(B). (C-H)** Arabidopsis flower buds in stage 9: SEM micrographs showing the flower buds of Col-0 **(C)** and *mad5* **(D)**. Fragments of sepal surface with frontier (blue line) of cuticular ridges formation in Col-0 **(E)** and *mad5* **(F)**. Close-up of cuticular pattern in Col-0 **(G)** and *mad5* **(H)**.

4.2.1 Growth and shape of pavement cells during ridges formation

In the early stages of flower development (up to the stage 7 according to Smyth et al. 1990), the surface of sepal pavement cells is smooth, without cuticular ridges. The ridges start to appear on the sepal surface in stage 8, in the apical portion of the sepal (Hervieux et al. 2016) and progress basipetally to cover the entire sepal surface in stage 12. *In vivo* confocal microscopy applied at 24 h intervals facilitated tracking of the process of ridges formation on the surface of individual cells. Noteworthy, the pavement cells continue to grow after the ridges formation has begun, as visualised in colourmaps presenting growth ratio of the cells (**Fig. 4.18A** and **B**). Cell growth at this stage of sepal development is accompanied by only infrequent divisions of pavement cells. In the course of cuticular pattern formation and during the following time intervals, each cell changes slightly the shape of its outline and surface curvature, as well as the growth ratio and direction (anisotropy). For the analysis presented here, the *in vivo* imaging of cells started when cuticular ridges were not visible (T0 – initial time point) and the cells were followed until the fully developed (distinct and well visible) ridges pattern appeared on their surface. Such analysis was performed for Col-0 (**Fig. 4.18**) and for *mad5* (**Fig. 4.19**) sepals.

After the cuticular pattern appears during the first time interval, the surface of cells is still expanding for up to 48 hours but the growth slows down (**Fig. 4.18B** and **Fig. 4.19B**). In Col-0 sepals, cells on the surface of which the ridges appeared during the first time interval (outlined in white in **Fig. 4.18),** grew slower than cells on which the ridges appeared later (cells marked with asterisks in **Fig. 4.18A**; see comparison in **Fig. 4.20A**). In *mad5,* the growth of such two groups of cells (compare cells marked with asterisks in A and outlined in white and purple in **Fig. 4.19**) was not significantly different (**Fig. 4.20B**). The growth ratio for cells with ridges appearing during the first time interval or later was similar in Col-0 and *mad5* (**Fig. 4.20C** and **D**).

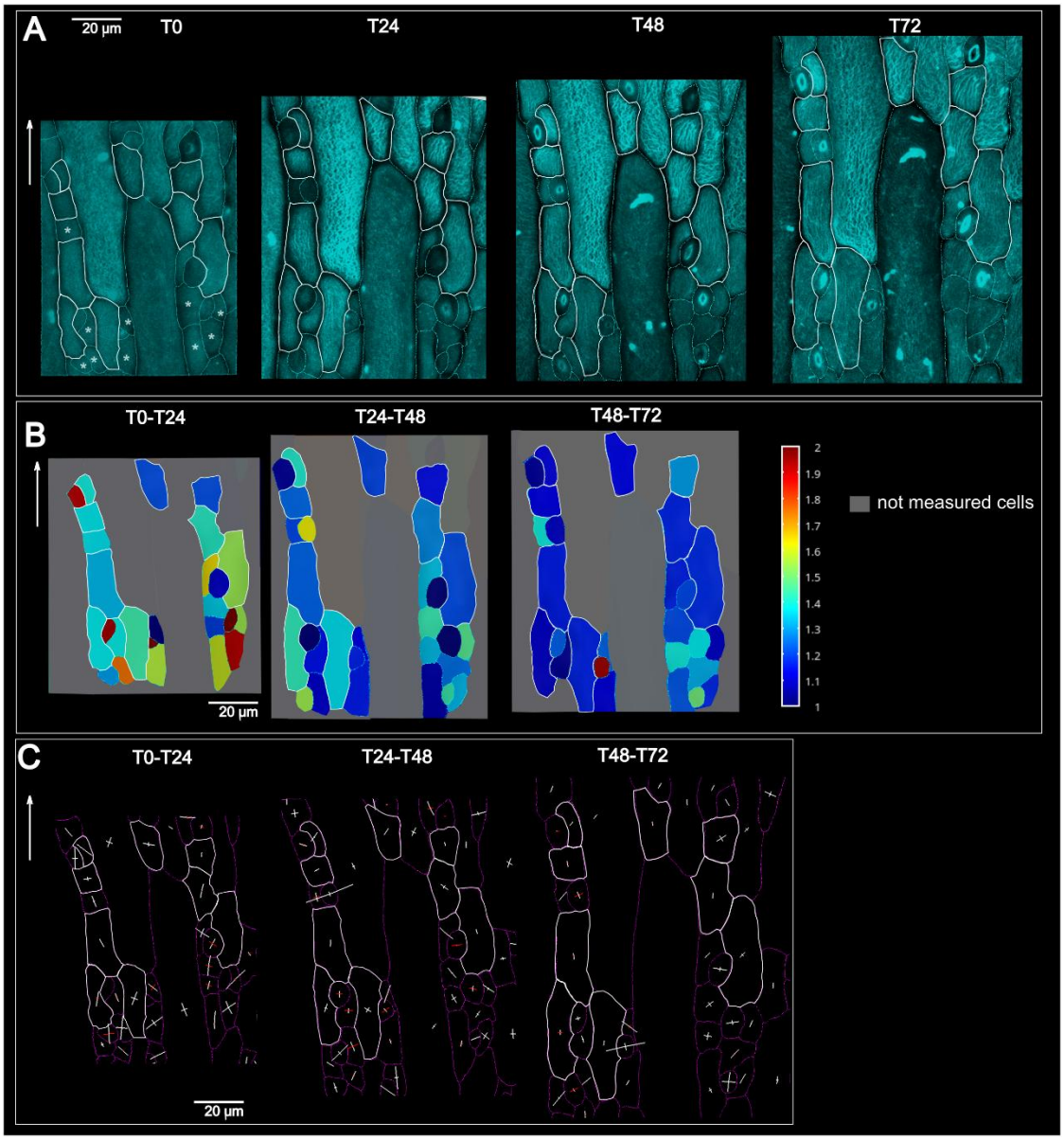

Fig. 4.18 Exemplary developmental sequence of a fragment of Col-0 sepal (sepal #3; see **Supplementary Table 1**) epidermis including cells already covered with ridges, those on which the ridges are formed during the first 24 h of observation (outlined in white), and cells on which ridges appear later (non-ridged cells labelled by asterisks at T0) **(A)**. **(B)** The sequence illustrates the growth ratio of the analysed cells. Cells that were not included in the analysis are shaded in grey. **(C)** Growth anisotropy represented by crosses overlaid on the cell outlines. Each cross shows Principal Growth Directions (PDGs) of the cell, and the length of the arms is proportional to the growth ratio in this direction. Cells on which ridges appear during the first time interval are outlined in white, cells on which ridges appear later, labelled with asterisks on A, are outlined in purple. T0 – initial time point, T24 – visualisation after 24 hours, T48 - after 48 hours, T72 – after 72 hours. Arrow points to the apical direction.

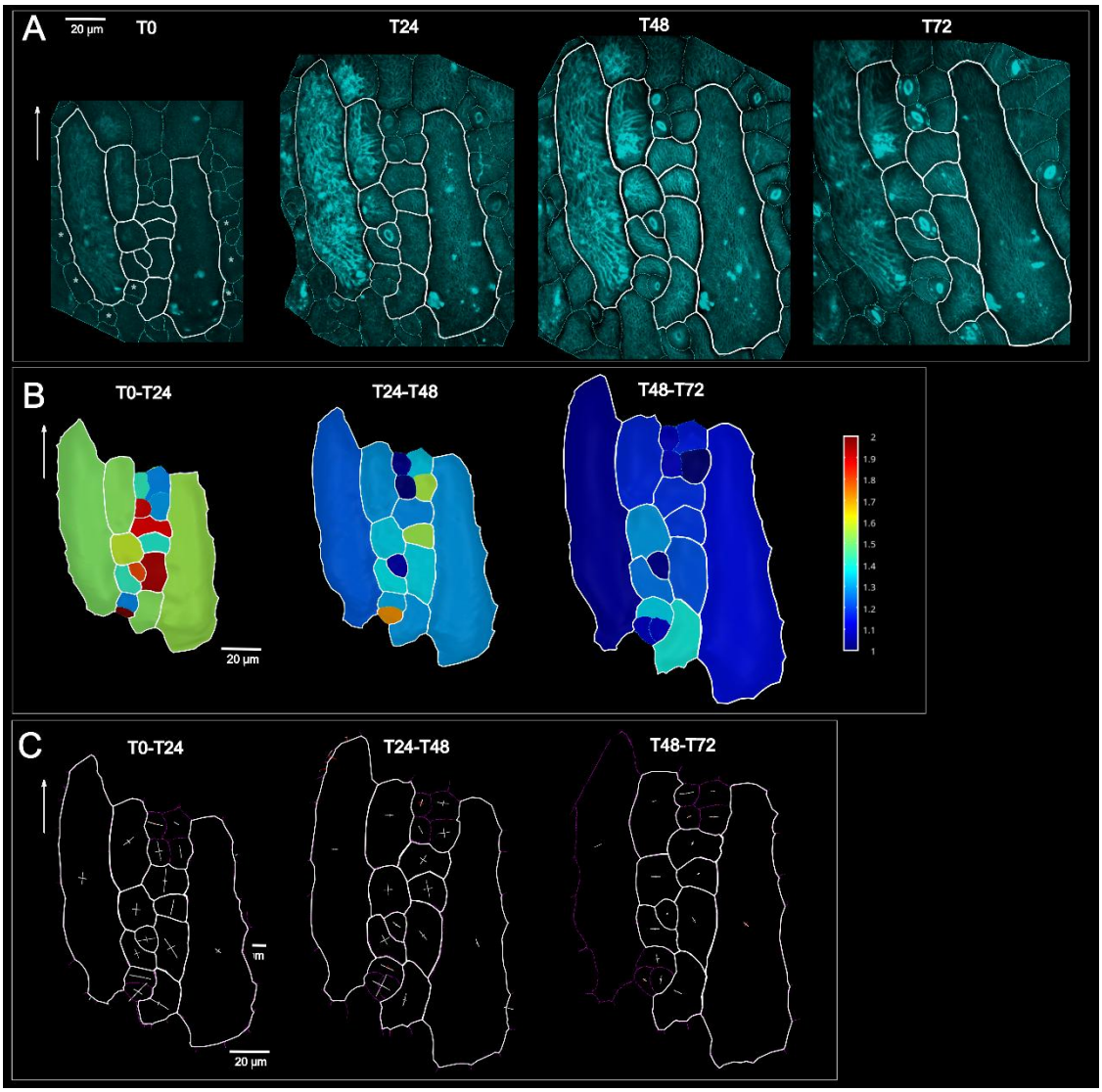

Fig. 4.19 Exemplary developmental sequence of a fragment of *mad5* sepal (sepal #2; see **Supplementary Table 1**) epidermis including cells already covered with ridges and without ridges. See **Fig. 4.18** legend for further explanation.

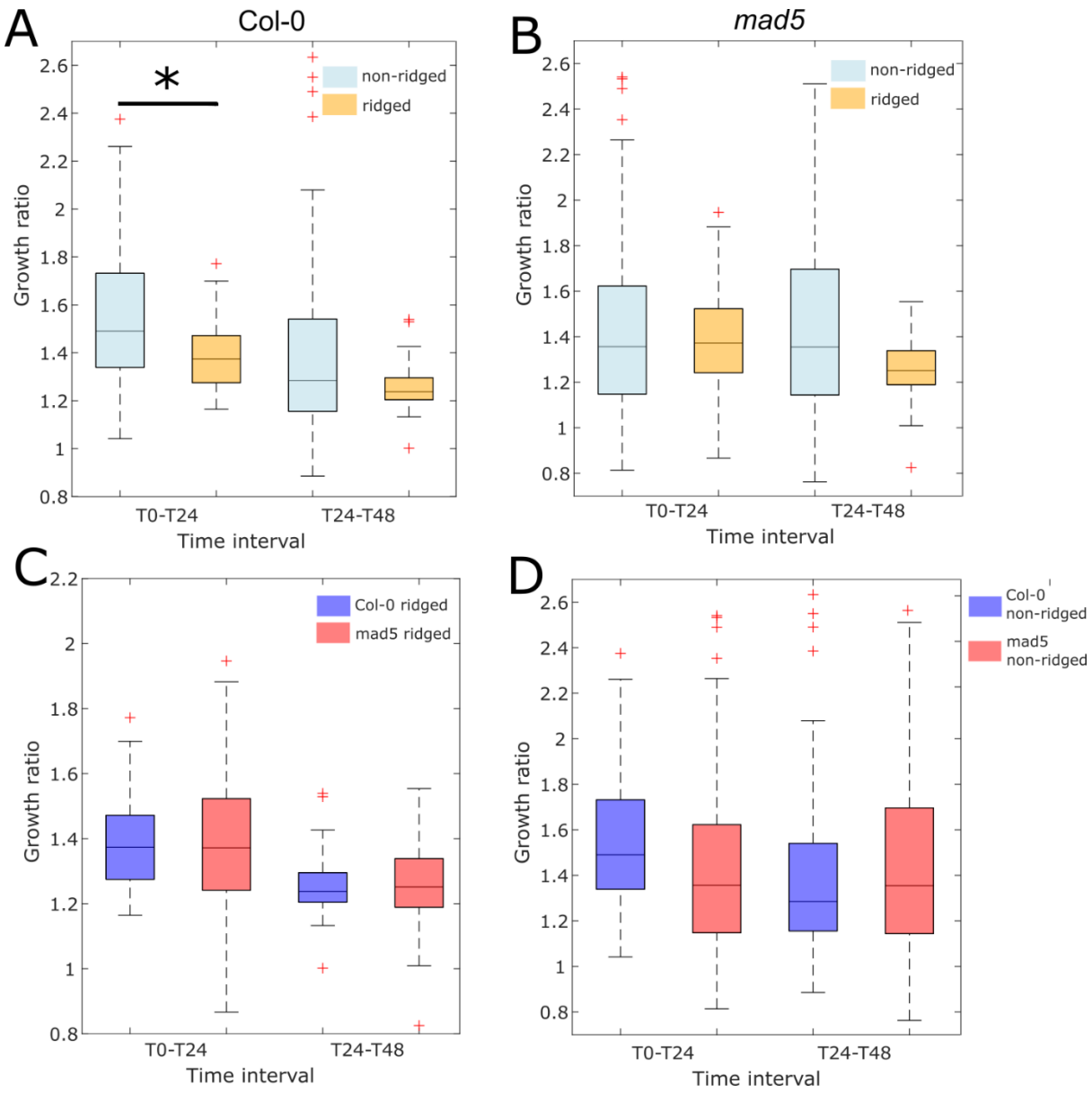

Fig. 4.20 (A, B) Comparisons of the growth ratio for Col-0 (**A**) and *mad5* (**B**) cells on the surface of which ridges were formed during the first time interval (ridged cells) and the cells on which ridges appeared later (non-ridged cells) (Col-0 non-ridged cells: 0-24h - 76 cells; 24-48h - 82 cells from 3 different sepals; Col-0 ridged cells: 0-24h - 25 cells; 24-48h – 25 cells from 3 different sepals; *mad5* non-ridged cells: 0-24h – 110 cells; 24-48h - 58 cells from 3 different sepals; *mad5* ridged cells: 0-24h - 31 cells; 24-48h – 31 cells from 3 different sepals). Asterisk marks statistically significant difference of pairwise comparison of the ratio between ridged and non-ridged cells; where p-value for Mann-Whitney test for 0-24h is 0.001 (for other pairwise comparisons p>0.05). **(C-D)** Col-0 and *mad5* growth ratio comparison for ridged (**C**) and non-ridged **(D)** cells. Differences between Col-0 and *mad5* are not statistically significant. See **Fig. 4.12** legend for further explanations; crosses are outliers.

Growth of pavement cells during the formation of cuticular ridges is accompanied by changes in cell shape, in particular curvature of the outer periclinal cell wall and the shape of the cell outline. Thus, next the shape of cells was quantified. First, local minimum, maximum and mean curvatures as well as overall cell curvature directions were assessed for the cells on the surface of which cuticular ridges were formed (for both genotypes these cells are outlined in white in **Fig. 4.18** and **19**; see **Fig. 4.21** for Col-0 curvature maps; **Fig. 4.22** for *mad5*). These parameters show how much the cell wall is bent in various directions with respect to the cell long axis. The cell walls, on which ridges are formed, are curved before the ridges formation, both in Col-0 (T0 in **Fig. 4.21**) and *mad5* (T0 in **Fig. 4.22**). All the three local curvature parameters increase during the cell growth and are generally higher in *mad5* than in Col-0 (note that colourmap scales are different in **Fig. 4.21A, B** and **Fig. 4.22A, B**). Crosses overlaid on the colourmaps of mean curvature represent directions of maximal and minimal curvature computed for the entire cell wall surface (white cross arm indicates that the wall is convex in this direction, red indicates that it is concave). In Col-0 cells (see crosses in **Fig. 4.21A**), the lengths of the two cross arms are usually very different (the maximal curvature computed for the entire cell wall surface is much higher than the minimal) and in case of elongated cells, the maximum curvature direction is usually perpendicular to the cell axis, which means that the overall shape of the cell resembles a cylinder. In *mad5* cells (see crosses in **Fig. 4.22A**), the differences in cross arm length are smaller, which means that the walls are bent rather strongly in all the directions. More difficult to interpret are curvature directions for small cells that are located between giant cells or/and are adjacent to stomata (Cell 5 in **Fig. 4.21;** note that guard cells were excluded from all measurements). The minimal curvature computed for these cells, nearly perpendicular to their long axis, is negative (red colour of cross arms) suggesting that in this direction their surface is concave. This, however, may be an artefact related to surface detection errors (the mesh approximating the sepal surface may locally not reach the intercellular junctions precisely). This problem was encountered mostly in Col-0, where pavement cells were between the convex giant cells.

Local minimal curvature (see colourmaps in **Fig. 4.21B** for Col-0 and **Fig. 4.22B** for *mad5*) is low at the cell periphery, i.e. close to the cell boundaries, because in these regions there are creases overlaying anticlinal walls between neighbouring cells. This was observed in both genotypes. The creases are deeper and wider between *mad5* cells

as manifested by wide regions of low minimum curvature (compare e.g. Cell 9 in Col-0 with Cell 7 in *mad5*). Also in both genotypes, local maximum curvature (**Fig. 4.21C** for Col-0 and **Fig. 4.22C** for *mad5*) is the highest in the centre of the cell. Noteworthy, both maximal and minimal curvatures vary strongly over the surface of relatively big *mad5* cells, i.e. the surface curvature is much less homogeneous than in Col-0 (compare e.g. Cell 8 and Cell 9 in Col-0 with Cell 5, Cell 6 and Cell 7 in *mad5*).

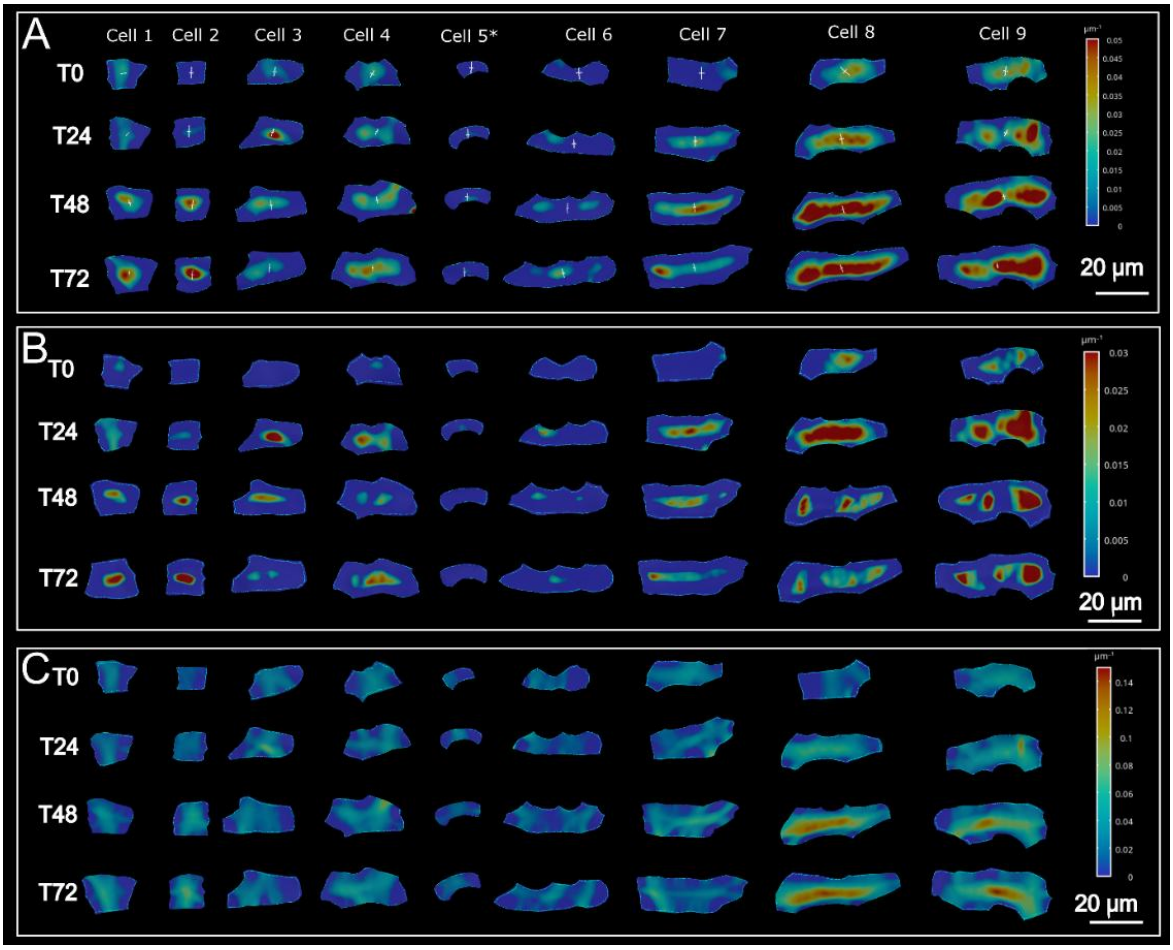

Fig. 4.21 (A) Colourmaps showing local mean curvature of the Col-0 cell surface on which surface ridges pattern is forming during the first time interval (the same cells are shown in **Fig. 4.18**, see cells of sepal #3 in **Supplementary Table 1**). Consecutive images of individual cells are shown in different columns. Crosses represent curvature directions computed for the entire cell wall surface. Cross arm is white if the wall is convex in this direction, red – if it is concave. **(B)** Colourmaps of local minimum curvature of the same cells. **(C)** Colourmaps of local maximum curvature. Cell 5, marked with white asterisk, is located adjacent to the stomata.

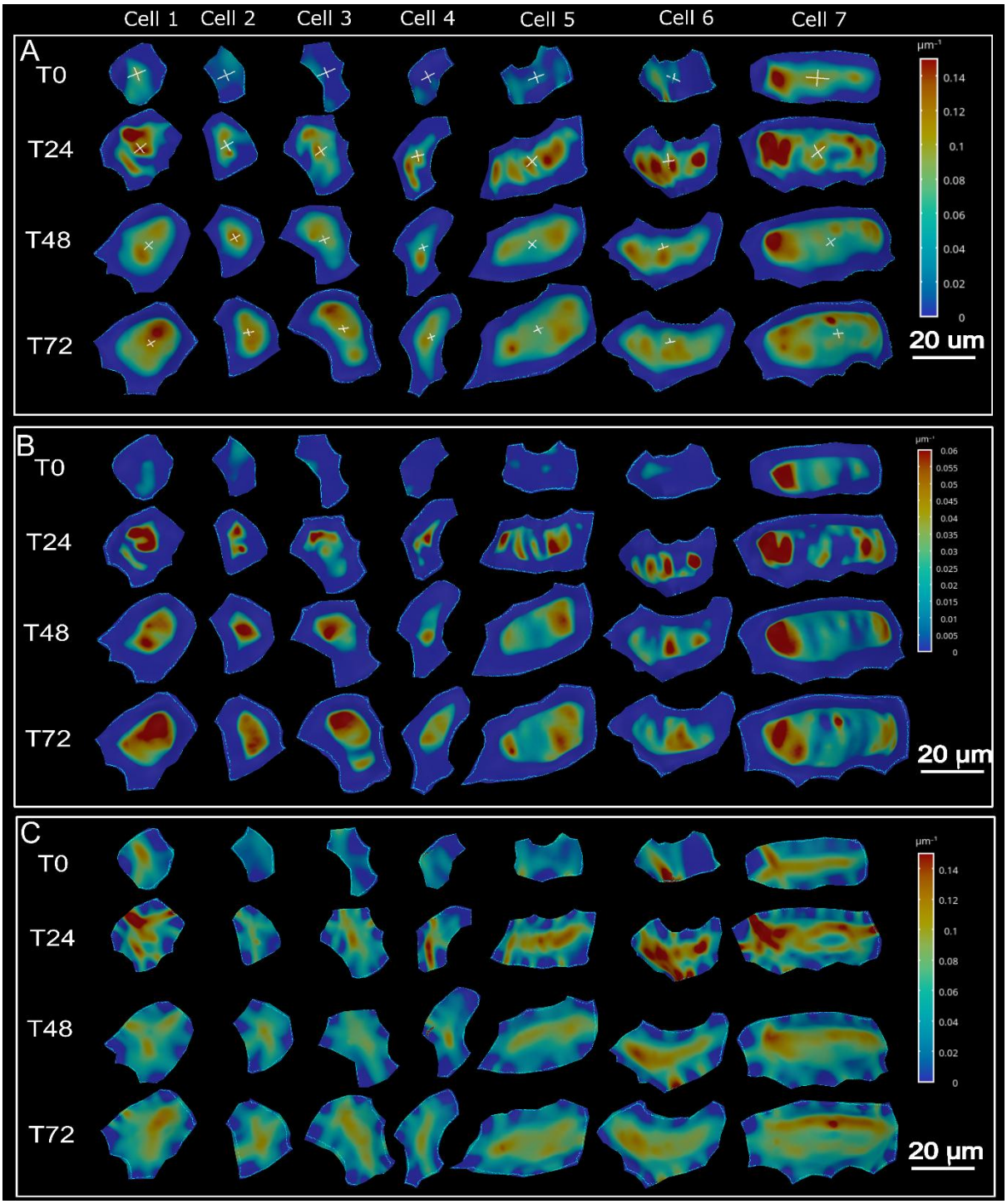

Fig. 4.22 Curvature colourmaps of *mad5* mutant (the same cells are shown in **Fig. 4.19**; see cells from sepal #2 in **Supplementary Table 1**). **(A)** Colourmaps showing local mean curvature of *mad5* cells with overlaid crosses representing curvature directions. **(B)** Colourmaps of local minimum curvature. **(C)** Colourmaps of local maximum curvature. See legend of **Fig. 4.21** for further explanation.

The epidermal pavement cells of Arabidopsis sepals differ not only in surface curvature but also in the shape of cell outline. The shape parameter, defined as the ratio of the long cell axis to the short cell axis, was used to quantify the outline shape. The shape parameter values of all analysed cells of Col-0 and *mad5* are presented in **Fig. 4.23A**. Within both genotypes the variation between the examined cells was very large (from 1 to 5, where 1 represents isodiametric cells and 5 - strongly elongated cells). The statistically significant differences between genotypes were observed in the time points T0 and T48 where Col-0 cells exhibited a higher value of shape parameter in comparison to *mad5*. It means that Col-0 cells were more elongated than *mad5* cells at the beginning of the time interval during which the ridges were formed. Another parameter of the cell outline shape is so-called lobeyness, which describes the extent of lobing (formation of protrusions) along the cell boundaries. Comparison of cell lobeyness in the two genotypes did not reveal statistically significant differences (**Fig. 4.23B**) and showed that in both Col-0 and *mad5* cell outlines are nearly smooth.

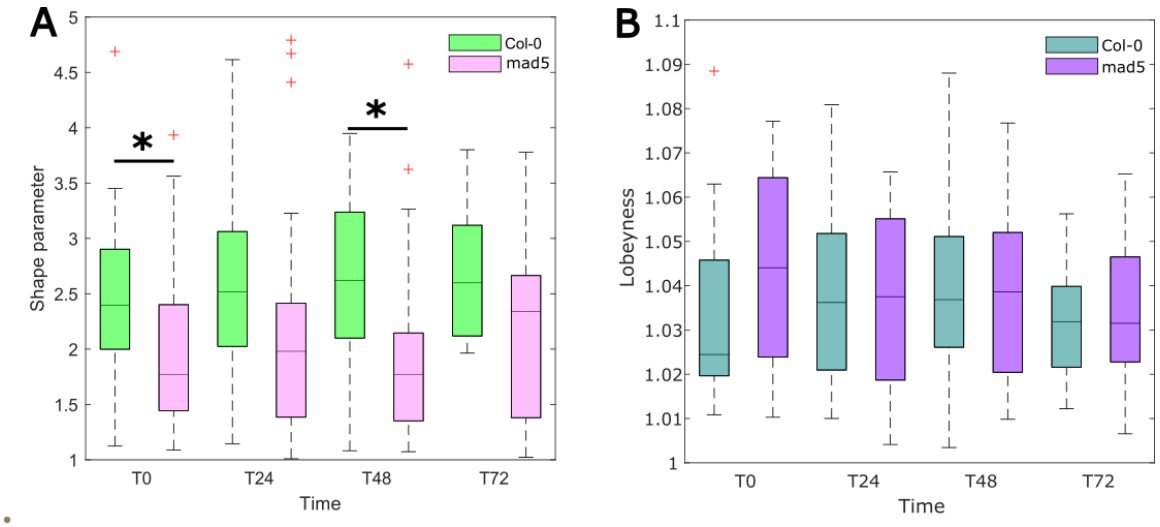

Fig. 4.23 (A) Comparisons of shape parameter of Col-0 and *mad5* cells, on which the ridges appear during the first time interval, plotted for consecutive time points. Asterisks point to statistically significant difference of pairwise comparison at a given time point; p-value for Mann-Whitney test for T0 is 0.045 and for T48 is 0.0385 ($p>0.05$ for other pairwise comparisons). **(B)** Lobeyness of the same Col-0 and *mad5* cells as shown in (A). $p>0.05$ for all pairwise comparisons. See **Fig. 4.12** legend for further explanations.

To summarize, cuticular ridges are formed on the initially smooth, slightly curved surface of sepal epidermal cells when the cell surface is still expanding. The cell growth slows down after the ridges formation in both genotypes but to a higher extent in Col-0.

Col-0 cells are generally more elongated than *mad5* cells. The outer periclinal walls of *mad5* cells are curved stronger than Col-0 cells already during the ridges formation, and the curvature in *mad5* is less homogeneous. The curvature of cell walls increases with time.

4.2.2 Relationships between orientation and shape of newly formed ridges and growth and geometry of pavement cells

Next, growth anisotropy, cell geometry as well as orientation and shape of newly formed ridges were examined in search of putative relationships between these parameters. Because both Col-0 and *mad5* cells showed high variation of the shape parameter, which was more variable than lobeyness, all the analysed cells were divided into three shape groups: cells in the shape group 1 had the shape parameter values between 1.0 and 2.0 (shape close to isodiametric), in the shape group 2 – 2.01 to 2.5, and in the shape group 3 – 2.51 and more (strongly elongated cells). For such groups of cells the existence of relationships between emerging pattern of cuticular ridges, overall and local growth anisotropy and surface curvature was verified.

4.2.2.1 Ridges formation on outer periclinal walls of nearly isodiametric cells (shape group 1)

Representative cells with the low shape parameter values are shown in **Fig. 4.24**. This shape group included only 6 Col-0 cells and much bigger number of *mad5* cells (18 cells).

At the beginning of the analysis, i.e. at the initial time point T0 (T0, green cell image in **Fig. 4.24**), the cell surface was smooth while the ridges became visible at the second time point (T24, green in **Fig. 4.24**). As described above, the cells were growing during the ridges formation. They differed in the degree of growth anisotropy assessed for the entire cell surface (see single crosses overlaid on purple cells in **Fig. 4.24**; growth and curvature parameters and relation with ridges pattern for individual cells are given in **Supplementary Table 1**). The mean degree of growth anisotropy for all Col-0 cells within this shape group was 1.17 in T0-T24 time interval, 1.16 in T24-T48 interval and

1.12 in T48-T72, while for *mad5*: 1.22 in T0-T24, 1.09 in T24-T48, 1.09 in T48-T72 (see **Supplementary Table 1**). Thus, in *mad5* cells, growth anisotropy decreased sooner after ridges formation than in Col-0. In the majority of cells of both genotypes, the newly formed ridges were parallel to the direction of maximal growth of the cell (cell PDGmax) during the time interval of ridges formation (see **Table 4.4**; Col-0 Cell 1 and *mad5* Cell 2 in **Fig. 4.24A**). In other cells, the ridges were orthogonal or oblique with respect to cell PDGmax (Col-0 Cell 2 in **Fig. 4.24A**), or it was impossible to compare the two directions because of the complex shape, especially the strong waviness, of the ridges (*mad5* Cell 1 in **Fig. 4.24A**).

Comparisons of cell wall surface curvature at T0 (just before cuticular ridges formation) and at T24 (just after the ridges formation) with cell PDGs during the first time interval (**Fig 4.24B; Supplementary Table 1**) showed that directions of maximal cell curvature and cell PDGmax are not similar but the direction of maximal curvature is often either nearly parallel or nearly orthogonal to the cell PDGmax (compare e.g. Cell 1 and Cell 2 of Col-0 in **Fig. 4.24B**). The tendency of opposite alignment of T0, T24 curvature and growth directions is somewhat stronger in Col-0 than in *mad5*, where curvature directions and growth directions are more often oblique (for curvature T0) or parallel (for curvature T24) to the cell PDGmax and at the same time parallel to the newly formed ridges (**Supplementary Table 1**). Accordingly, in majority of Col-0 cells, ridges were parallel to the cell PDGmax and orthogonal to the maximal curvature direction while in majority of *mad5* cells, ridges were parallel to the cell PDGmax and to the maximal curvature direction (**Table 4.4**).

Next, the local PDGs were investigated (numerous smaller crosses overlaid on purple cells in **Fig. 4.24A**). Although it has to be kept in mind that the assessment of local PDGs may be erroneous because the model is very sensitive to the position of cell junctions and additional landmarks used to reproduce cell outlines, it was the only available protocol to assess the local growth of the cell surface. Nevertheless, the analysis showed that local PDGs and the orientation of newly formed ridges are often related (**Table 4.4, Supplementary Table 1**). Namely, the newly formed ridges that are not very wavy are often nearly parallel to the local PDGmax (see purple Col-0 Cell 1 with small crosses at T0-T24, **Fig. 4.24A**). In many cells, such alignment of ridges and local PDGmax was true only for a portion of cell surface (*mad5* Cell 1 in **Fig.4.24A;** "mixed" in **Table 4.4**).

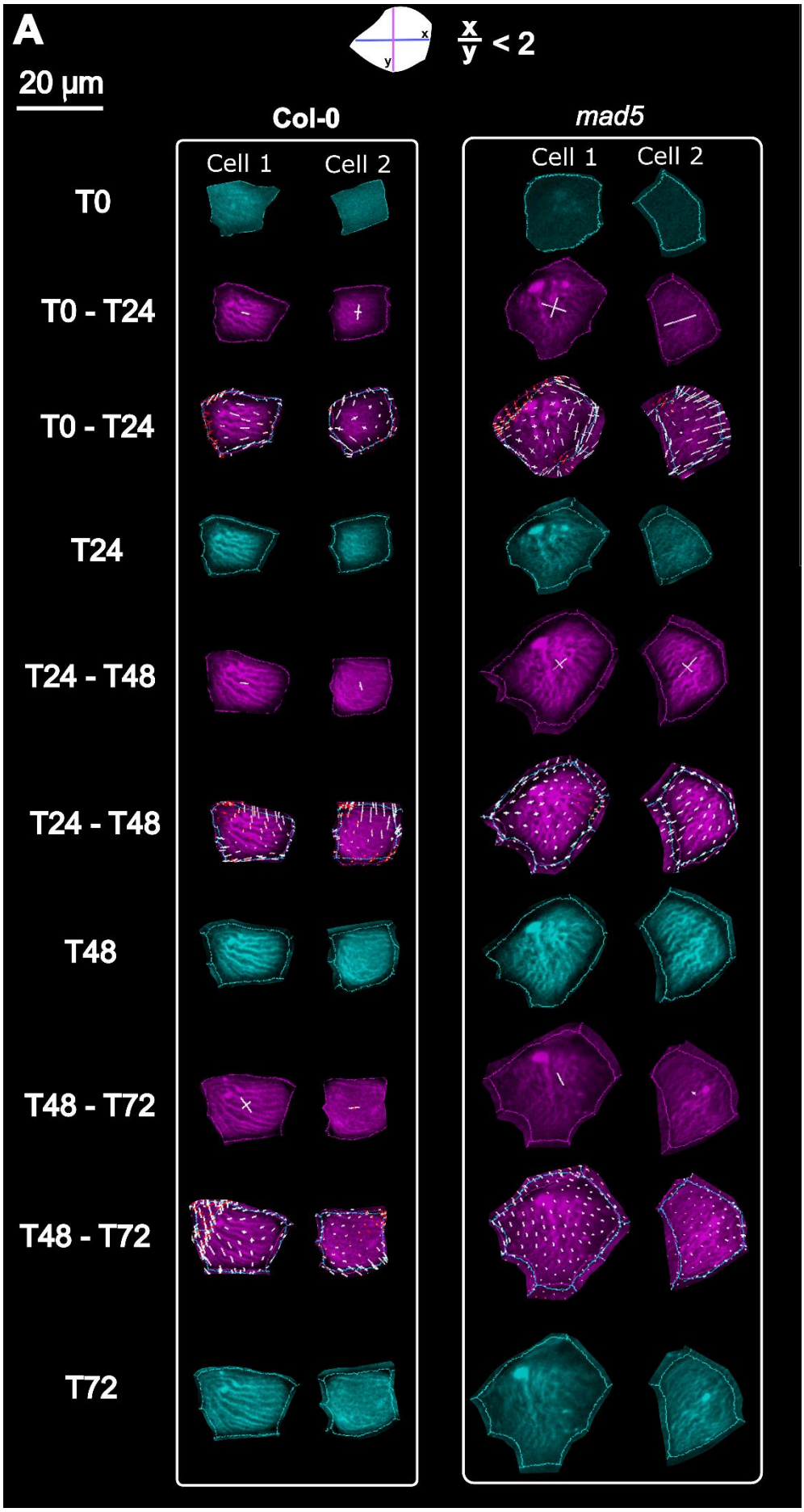

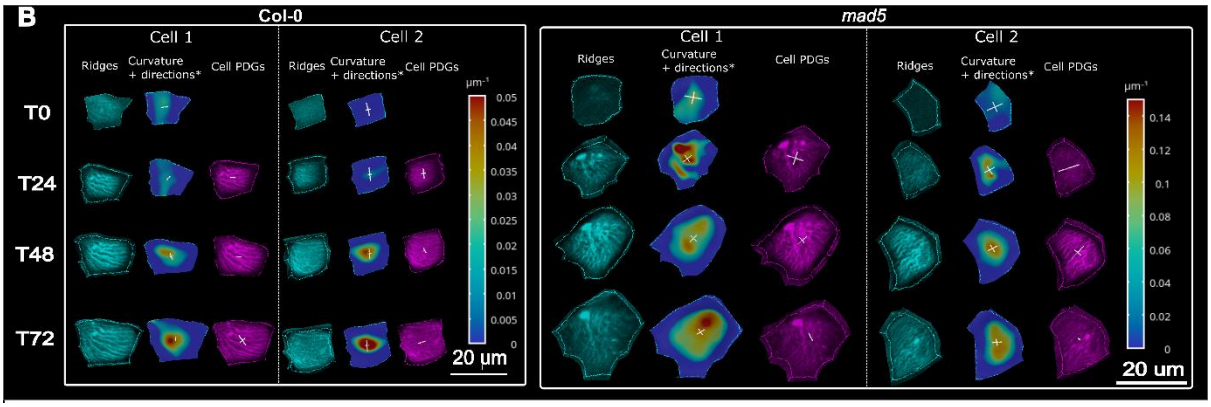

Fig. 4.24 (A) Exemplary Col-0 and *mad5* cells belonging to shape group 1 (at the first time point). Green images represent the cell at the beginning of the time interval for which growth was assessed. Purple are cells at the end of the time interval. PDGs are overlaid on cell images at the end of time interval: big crosses represent the cell PDGs, smaller crosses are local PDGs, computed at the subcellular scale. **(B)** Images of the surface of the same cells as in A, at the beginning of time interval (green) followed by the map of local mean curvature with overlaid overall cell curvature directions, and the cell surface image at the end of time interval (purple) with overlaid cell PGDs.

4.2.2.2 Ridges formation on the moderately elongated cells (shape group 2)

This shape group includes cells that are moderately elongated (shape parameter 2.0-2.5), with examples presented in **Fig. 4.25.** Col-0 was represented by 11 such cells and *mad5* by 10. As already mentioned, all the cells in this group are growing when ridges are formed. At the cellular scale, the cell PDGmax during the ridges formation was parallel (Cell 3 of *mad5*), oblique (Cell 1 of Col-0) or perpendicular (Cell 2 of *mad5*) with respect to the long cell axis, meaning that at least some cells were not only elongating but also growing in width (big crosses on T0-T24 purple cells in **Fig. 4.25A**). Mean growth anisotropy for Col-0 was similar to *mad5* during this time interval (1.23 for Col-0 and 1.23 for *mad5*). Later, growth anisotropy decreased in *mad5* (for interval T24-T48 it was 1.09, for T48-T72 – 1.13; **Supplementary Table 1**). In Col-0, cells maintained higher anisotropy during T24-T48 interval (1.21), while it decreased to 1.12 during the T48-T72 interval. Ridges in Col-0 cells were usually aligned with the cell PDGmax (e.g. Col-0 Cell 2 **Fig. 4.25A, Table 4.4)**, while *mad5* ridges were oblique to the PDGmax in most cases (Cells 1, 4 in **Fig. 4.25A; Table 4.4**). In some cells, especially in *mad5*, the waviness of ridges prevented such comparison (*mad5* Cell 2 in **Fig. 4.25A**).

The cell PDGmax was less often parallel to the maximal curvature direction at T0 or T24 in this shape group than in the group 1 (**Fig. 4.25B; Supplementary Table 1**).

Accordingly, the tendency of alignment of newly formed ridges and T0 or T24 curvature was also weaker (**Table 4.4)**.

The local PDGs in Col-0 and *mad5* were not uniform within the cells during the time interval when ridges were formed (T0-T24 interval, purple cells with small crosses in **Fig. 4.25A**). Similar to shape group 1, in many cells, alignment of ridges and local PDGmax was true only for a portion of the cell surface (Col-0 Cell 2, *mad5* Cell 3 in **Fig. 4.25A; Table 4.4**). A unique case was one of the *mad5* cells that exhibited local shrinkage (Cell 2 in **Fig. 4.25A**), which was followed by ridges accumulations in this part of the cell (see timepoints T48, T72, *mad5* Cell 2 in **Fig. 4.25A**) while the remaining newly formed ridges in the first time interval followed the local PDGmax in the remaining parts of the cell.

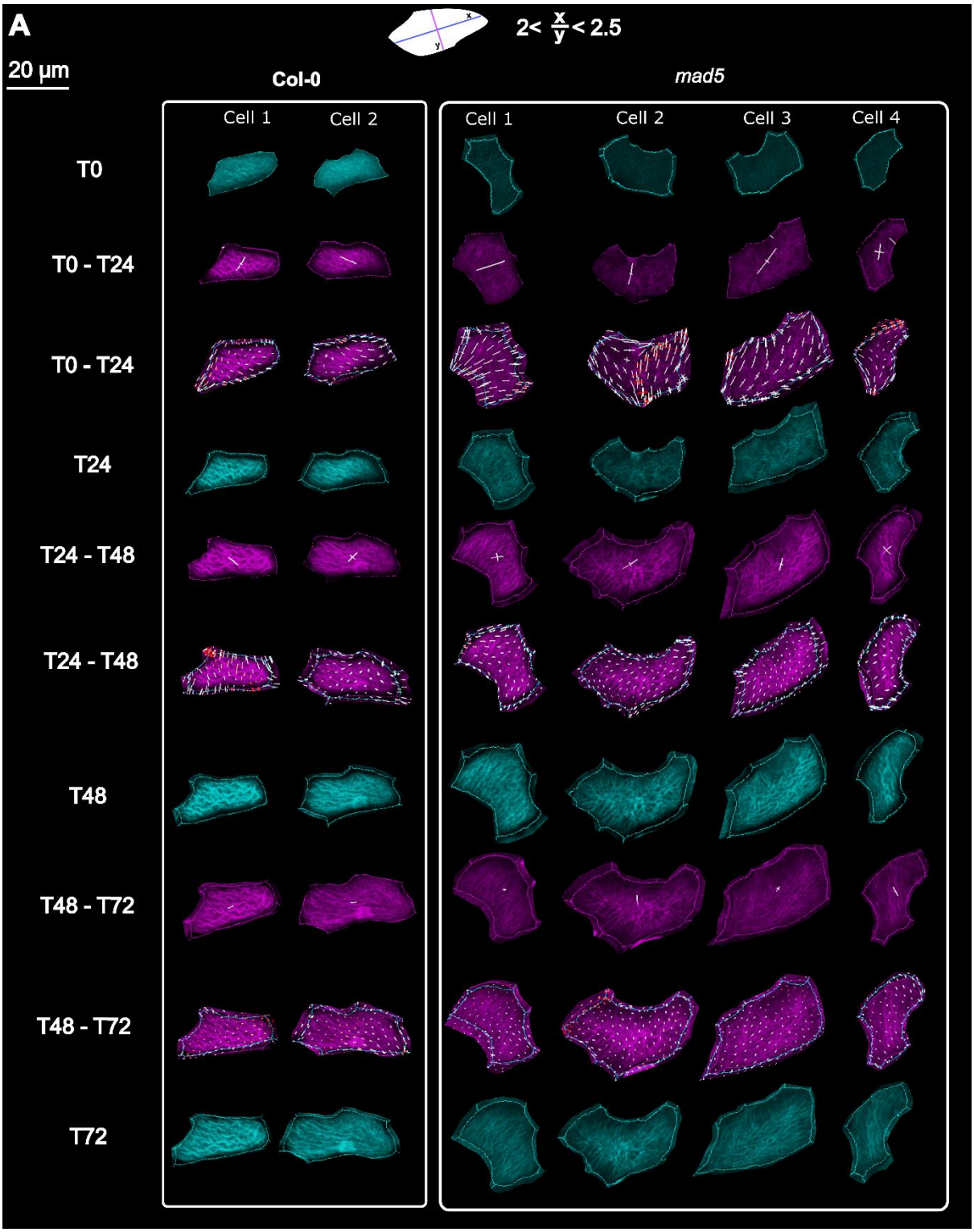

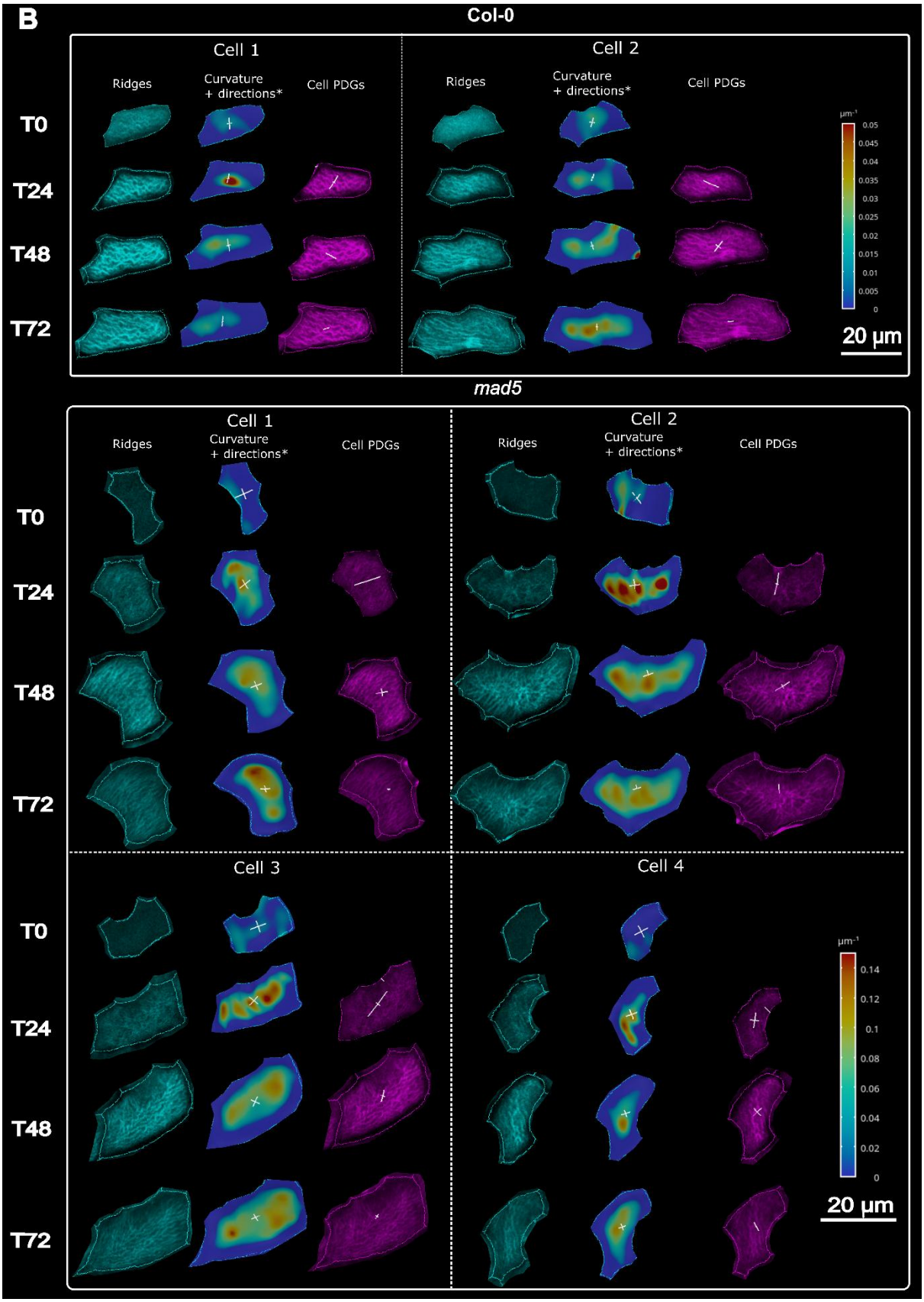

Fig. 4.25 Exemplary Col-0 and *mad5* cells belonging to shape group 2. See **Fig. 4.24** legend for further explanation.

4.2.2.3 Ridges formation on the surface of strongly elongated cells (shape group 3)

Examples of strongly elongated cells are presented in **Fig. 4.26.** This group includes 8 cells for Col-0 and 3 for *mad5*. Mean growth anisotropy was higher for Col-0 in comparison to *mad5* during the T0-T24 interval (1.26 for Col-0 and 1.08 for mad5; see **Supplementary Table 1**). Later, growth anisotropy in *mad5* was similar to the interval T0-T24 (for interval T24-T48 it was 1.09, for T48-T72 – 1.10) while Col-0 cells the anisotropy slowly decreased (during T24-T48 it was 1.16 and decreased to 1.13 during the T48-T72 interval). The orientation of cell PDGmax in both Col-0 and *mad5* varied and was parallel to the long axis of some cells and oblique or orthogonal in others (compare Col-0 Cells 1,2 with 3 or *mad5* Cells 2 and 3 in **Fig. 4.26A)**. In the majority of Col-0 cells, the newly formed ridges were parallel or oblique to the cell PDGmax (e.g. Cells 1 and 3 in **Fig. 4.26A**, respectively; **Table 4.3**). In *mad5*, such comparison was not possible because of strongly wavy ridges.

Cell surface curvature increased in time in both genotypes (**Fig. 4.26B**). Interestingly, in *mad5* cells the local curvature (presented on colourmaps) was much less homogeneous than in Col-0, which was accompanied by very complex pattern of ridges (similar situation was observed in *mad5* Cell 2 from shape group 2 shown in **Fig. 4.25B**). Relationships between orientation of maximal cell curvature and cell PDGmax were similar to those of shape group 2 and there was no tendency for alignment of newly formed ridges and maximal curvature direction at T0 or T24 (**Table 4.4)**.

Similar to the shape group 2, the orientation of local PDGs varied over individual cell surface (T0-T24 interval, purple cells with small crosses in **Fig. 4.26A**). In Col-0, in some cell portions ridges appeared along the local PDGmax.

To sum up, in all the shape groups, the orientation of newly formed ridges is in most cases parallel to PDGmax at both cellular and subcellular scales (**Table 4.4**). The relation between ridges orientation and curvature is much weaker. Only in shape group 1 in Col-0, orientation of newly formed ridges is usually perpendicular to the direction of maximal curvature while there is no relation in other Col-0 groups and in *mad5*.

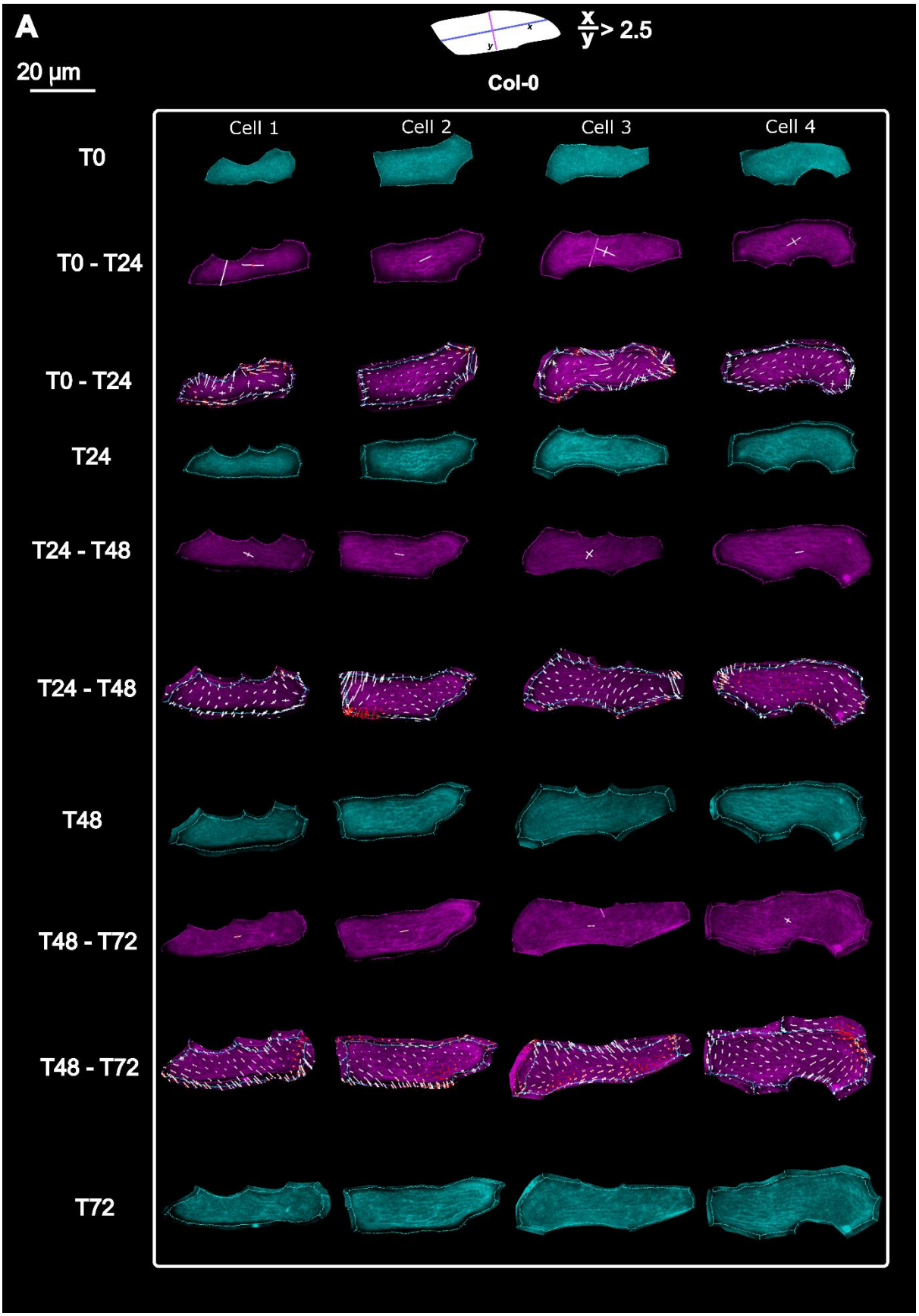

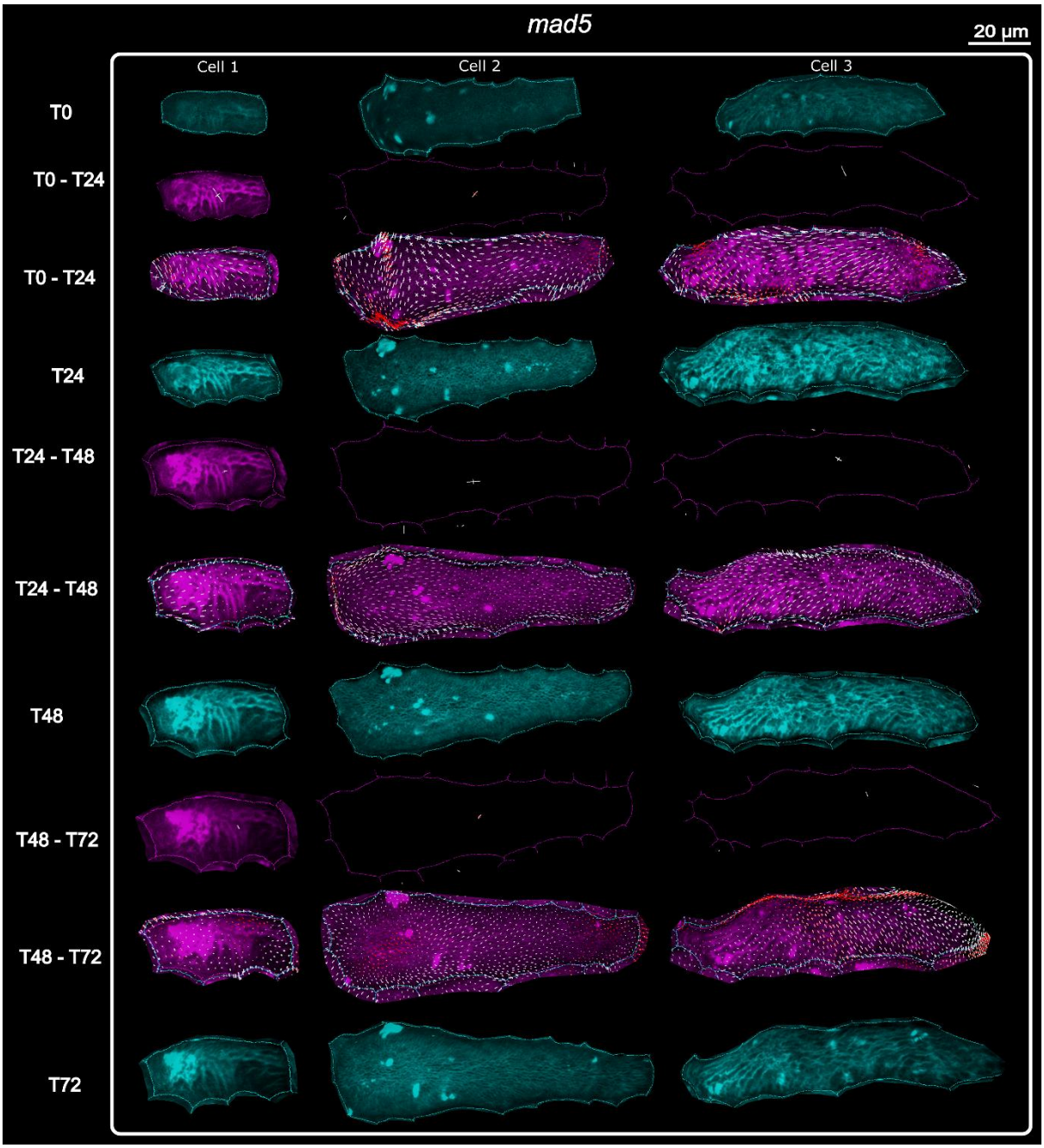

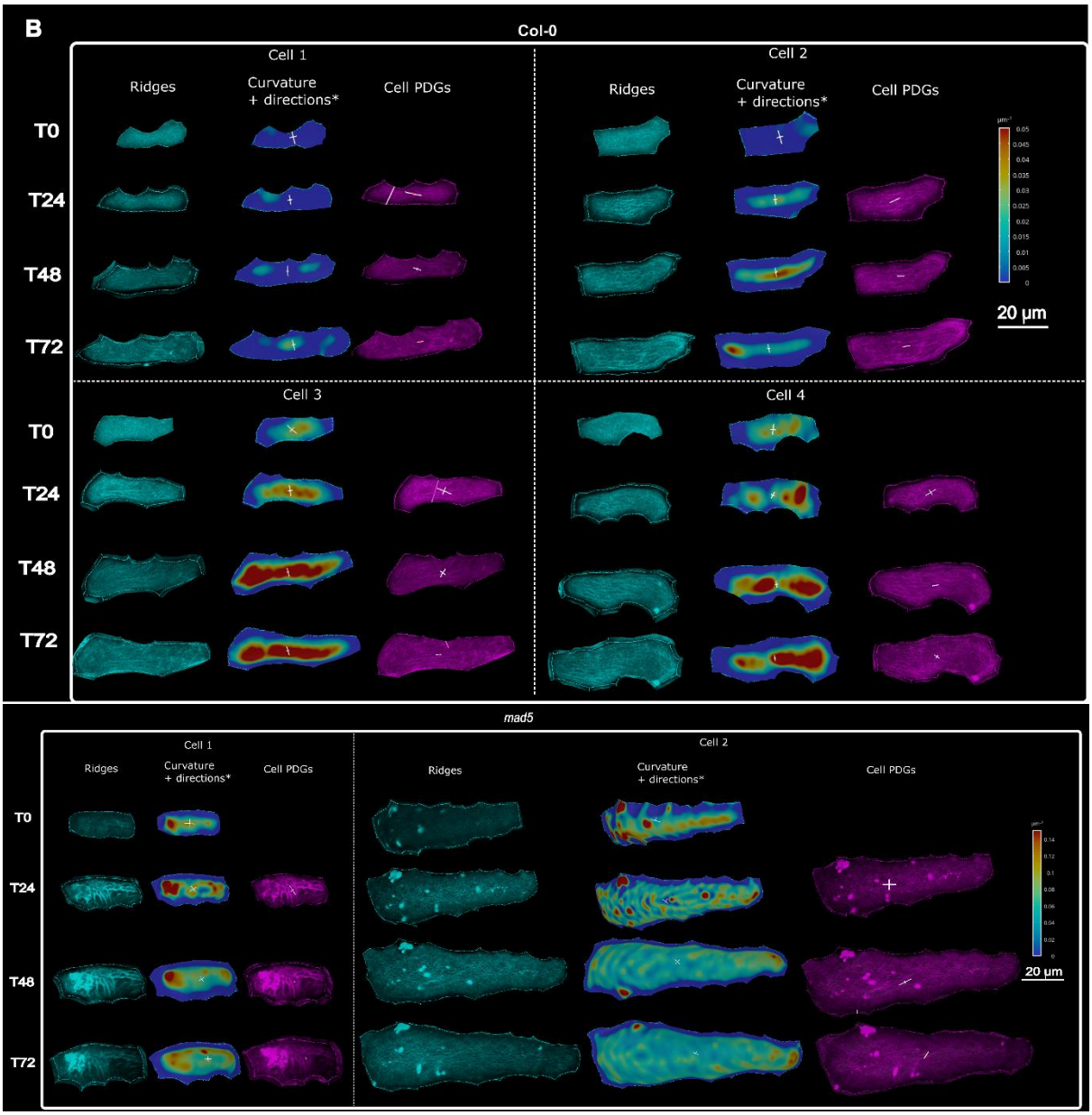

Fig. 4.26 Exemplary Col-0 and *mad5* cells belonging to shape group 3. See **Fig. 4.24** legend for further explanation.

Genotype	Shape group	General ridges direction vs Cell PDGmax				General ridges direction vs maxCurvT24				Local ridges direction vs local PDGmax				
		Parallel	Orthogonal	Oblique	N/A	Parallel	Orthogonal	Oblique	N/A	Parallel	Orthogonal	Mixed	Oblique	N/A
Col-0	1	5	1	0	0	1	4	1	0	4	2	0	0	0
	2	6	1	3	1	1	4	4	2	4	0	4	0	3
	3	3	0	4	1	3	4	0	1	1	0	7	0	1
mad5	1	6	2	2	8	6	2	0	10	4	1	5	0	8
	2	2	0	4	4	2	2	1	5	1	0	5	0	4
	3	0	0	0	3	0	0	0	3	0	0	1	0	2

Table 4.4 Summary of relations between growth, curvature directions and ridges orientation in cells of the three shape groups of Col-0 and *mad5* sepals. N/A refers to cells for which the ridges pattern was such complex (e.g. strongly wavy ridges) that their orientation could not be recognised. Cell PDGmax – direction of maximal growth assessed for the cell; local PDGmax – direction of maximal growth assessed at subcellular scale; maxCurvT24 – direction of maximal curvature assessed for entire cell wall at time point T=24h; mixed refers to cells with ridges variously oriented with respect to local PDGmax in different porrtions of the wall.

4.3 Changes in pattern of cuticular ridges accompanying cell surface growth

The analysis of ridges formation showed that from the very beginning the cuticular pattern varies between cells and/or between portions of an individual cell. Moreover, close inspection of the pattern on the surface of an individual cell at different time intervals reveals that the pattern is often changing (compare ridges at consecutive time points in **Figs. 24-26A**). Investigations of such changes in the cuticular pattern may provide crucial information for understanding the mechanisms of ridges formation. Thus, in this section the focus is on the variation and changes of the already existing pattern of cuticular ridges. Because the ridges form a complex pattern that covers the entire surface of the outer periclinal cell wall the pattern was investigated at two scales. The first scale is cellular where the overall ridges pattern on the whole cell surface is analysed. The second scale is subcellular and pattern variation down to the scale of individual ridges is examined.

4.3.1 Changes at the cellular scale

First, the ridges alignment on the cell surface, i.e. the pattern anisotropy, was assessed using FibrilTool plugin in ImageJ. The anisotropy of ridges pattern is visualized as a red line segment oriented in the direction of ridges alignment on the cell surface, the longer the segment the more aligned are the ridges (see **Fig. 4.27A** for Col-0 and **Fig. 4.27B** for *mad5*). The analysis was performed for pavement cells of the sepal epidermis, for which the *in vivo* imaging started when their surface was already covered with cuticular ridges, and the analysis started at T24 when the pattern was distinct. In both Col-0 and *mad5*, ridges alignment usually increased at subsequent time points (the length of red line segment is increasing in **Fig. 4.27**). In Col-0 cells, ridges were aligned along or very close to the long cell axis (see Cells 1,2,6, and 9 in **Fig. 4.27A**), while in *mad5* ridges orientation with respect to the long axis of the cell was variable (compare e.g. Cells 3,5 and 9 in **Fig. 4.27B**). However, the biggest difference between the two genotypes was in ridges morphology: Col-0 ridges are apparently less wavy than *mad5.* Moreover in *mad5*, ridges may form complex pattern where distinguishing one ridge from another is very difficult or even impossible (see Cells 4,6 and 10 in T24 in **Fig. 4.27B**).

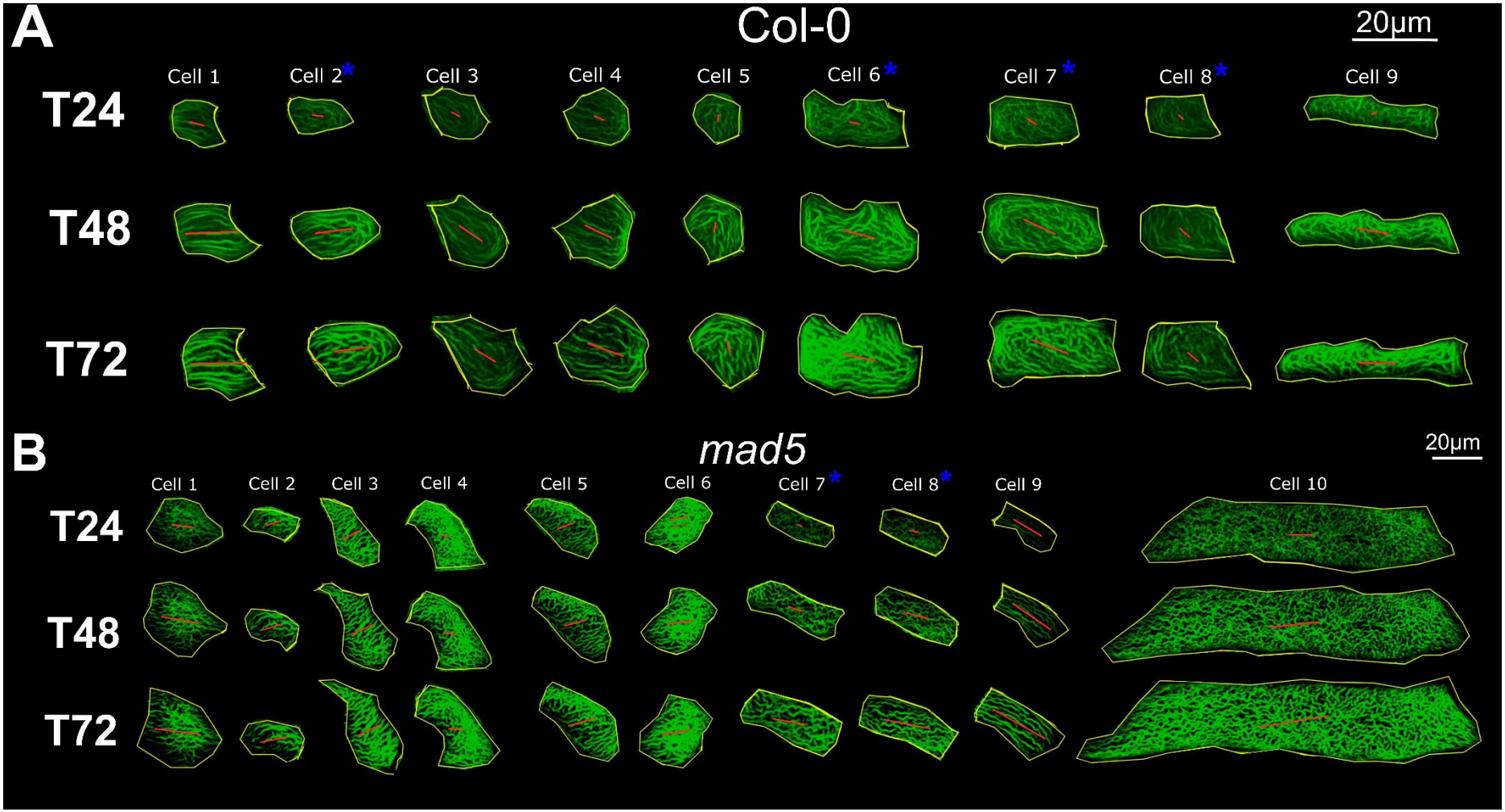

Fig. 4.27 Exemplary Col-0 **(A)** and *mad5* **(B)** cells with anisotropy of cuticular pattern (red lines) measured at each time point. Red line segments show the direction of ridges alignment and their length is proportional to the extent of alignment. Asterisks mark cells with new short ridges formed in between existing ones (compare T72 with T24).

Next, such assessed anisotropy of ridges pattern was compared in the two genotypes. At the first two time points (T24 and T48) ridges pattern anisotropy was higher in Col-0 cells than in *mad5* cells (**Fig. 4.28A**), which is most likely related to the fact that in *mad5* ridges are more wavy. Moreover, changes in anisotropy during the cell wall expansion (difference between anisotropy value at the last, T72, and first, T24, time points; Δ anisotropy; **Fig. 4.28B**) differed between the two genotypes. In Col-0, ridges anisotropy increased in some cells and decreased in others. Decrease in anisotropy could be related to formation of new ridges (cells with the new ridges are marked by the blue asterisks in **Fig. 4.27,** details are shown in **Fig. 4.29A**) or changes in shape of the already existing ridges (both cases are described below). In *mad5*, ridges alignment increased in majority of the examined cells. The reason for this increase is not clear because the ridges in *mad5* were very wavy, which made it difficult to detect new ridges between the existing ones. Moreoever, in the mutant, ridges often create more complex structures and deeper "layers" of ridges often cannot be visualised in *in vivo* confocal images.

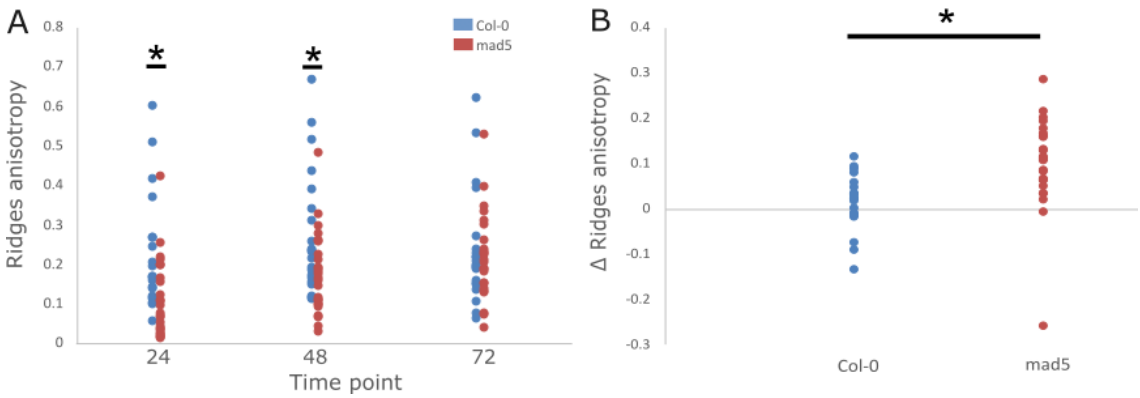

Fig. 4.28 (A) Comparison of anisotropy of ridge pattern of all analysed cells of Col-0 (21 cells) and *mad5* (25 cells) at different time points. Asterisks mark statistically significant differences of pairwise comparison of *mad5* with Col-0; p-value for Mann-Whitney test for T24 is 0.035 and for T48 is 0.042; for T72 p>0.05. **(B)** Comparison of ridge anisotropy changes (T24 anisotropy subtracted from T72 anisotropy) between the two genotypes. Asterisk points to significant difference (p-value for Mann-Whitney test 0.045).

During the cell surface growth new ridges appeared in between the already existing ones (**Fig. 4.29**). This was observed in both genotypes. However, newly formed ridges in Col-0 were much shorter, less distinct and sometimes perpendicular to the existing ones (**Fig. 4.29A**). In *mad5* cells, some new ridges were short and perpendicular to the existing ones, in other cases rather long new ridges appeared parallel to the existing ones.

These new ridges were well visible and wavy (see **Fig. 4.29B)**. Interestingly, in *mad5* a few cells in two sepals were covered by very long ridges which extended to the adjacent cell (**Fig. 4.30**; not included in the measurements) while in Col-0 such phenomenon was not observed.

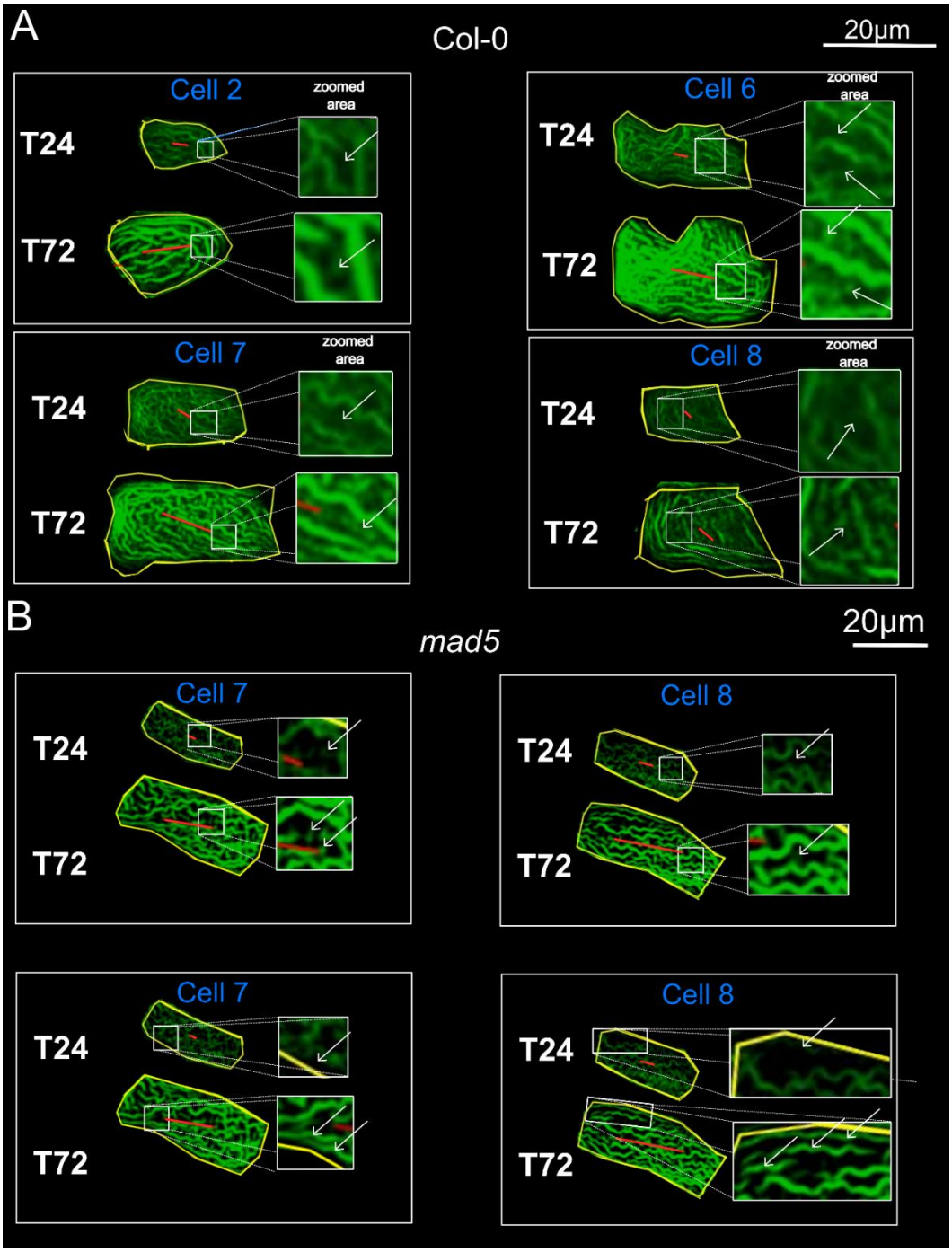

Fig. 4.29 Exemplary Col-0 **(A)** and *mad5* **(B)** cells (the same as labelled by asterisks in **Fig. 4.27**) on the surface of which new ridges appear, details are shown in insets. White arrows point to the place where new ridges were formed.

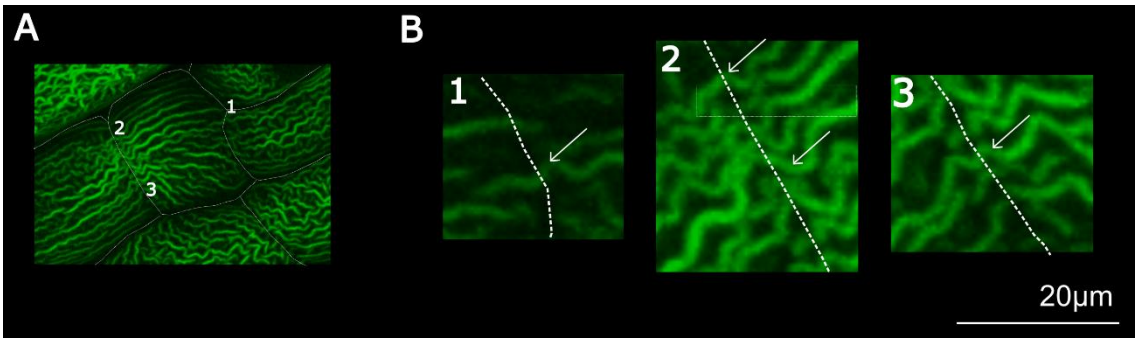

Fig. 4.30 Exemplary fragment of cell ridges pattern in *mad5* (**A**). (**B**) Enlarged places marked by numbers in A. Arrows point ridges passing the boundary between two cells.

4.3.2 Changes at the subcellular scale

Cells, on which ridges appeared, often had rather complex shapes while local growth of individual cell surface was not uniform (see **Figs. 4.24-26**). Both these factors can explain the variation of orientation and/or waviness of ridges within the individual cell walls (see e.g. Col-0 Cell 2 in **Fig. 4.25A** and Col-0 Cell 4 in **Fig. 4.26A**). As a consequence of this variation, anisotropy of ridges pattern assessed for the entire cell wall can be low despite the fact that locally the ridges are aligned but with different orientation. Thus, the cuticular pattern and its changes were also assessed for cell portions, which were identified on individual cell surface at consecutive time intervals based on specific traits of the ridges pattern, e.g. ridge endings. Ridges anisotropy of cell wall portions are presented in **Fig. 4.31**. Such an approach revealed that the shape of the cell has an impact on ridges anisotropy and anisotropy changes of cell portions are different than the changes at the cellular scale. For example, in Col-0 cell shown in upper panel of **Fig. 4.31A**, comparison the cell portions anisotropy at consecutive time intervals reveals that ridges alignment (anisotropy value represented by red segment length) increases slightly more near the cell ends than at its centre. It means that ridges straightening is not homogeneous within the cell. Inspection of the elongated Col-0 cell shown in the lower panel of **Fig. 4.31A** shows, in turn, increasing differences in the orientation of ridges in adjacent cell portions. Another example of such changes is *mad5* second cell in **Fig. 4.31B**.

In general, anisotropy of cell portions has higher values for Col-0 than for *mad5* showing that cuticular ridges are more aligned at all the three time points (**Fig. 4.32).** This is most likely related to the fact that ridges were more wavy in *mad5*. However, changes in

ridges anisotropy during the cell wall expansion assessed for wall portions (Cell Portions Δ anisotropy*)* did not differ significantly between Col-0 and *mad5*. In both genotypes, ridges alignment either increased or decreased during growth (**Fig. 4.32B)**.

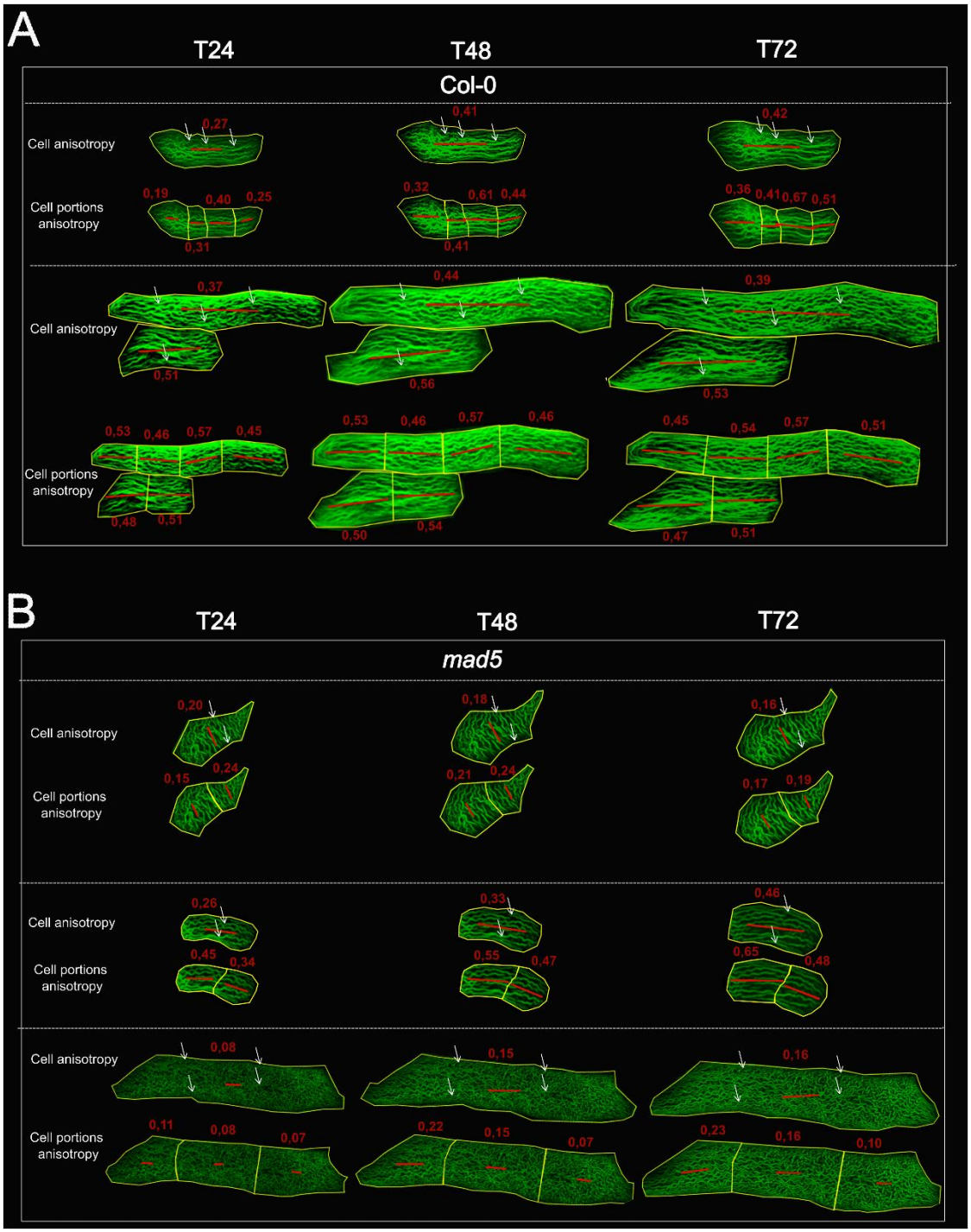

Fig. 4.31 Exemplary ridges anisotropy assessed for the entire cell and for portions of the same cells for Col-0 (A) and *mad5* (**B**). White arrows point to ridge endings, which were used to identify the same portions at consecutive time points.

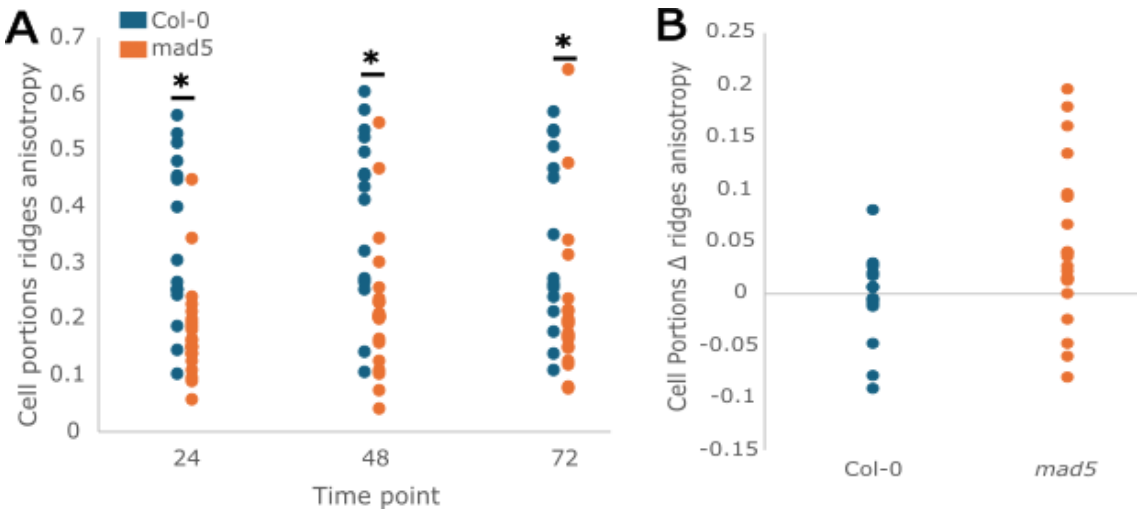

Fig. 4.32 (**A**) Ridges pattern anisotropy of cell wall portions for Col-0 (16 portions) and *mad5* (19 portions) at consecutive time intervals. Asterisks mark statistically significant differences of pairwise comparison between *mad5* and Col-0; p-value for Mann-Whitney test: T24 0.0000834, T48 0.000394, T72 0.000578 (**B**) Changes of anisotropy between the last time point (T72) and the first time point (T24). The difference between Col-0 and mutant is not significant (p>0.05).

Because the above comparisons of anisotropy of ridges pattern suggest that ridges may either become more wavy or straighten during the cell wall expansion, the following analysis focused on the fate of individual ridges (**Fig. 4.33, Fig. 4.34**). The anisotropy of individual ridges assessed for Col-0 was higher than in *mad5* at all time points, i.e. Col-0 ridges were less wavy (**Fig. 4.34A**). Interestingly, the ridge anisotropy during wall expansion (difference in anisotropy between T72 and T24) was increasing in all the cases examined and did not differ between the genotypes which showed that their behaviour during cell development is similar (**Fig. 4.34B**).

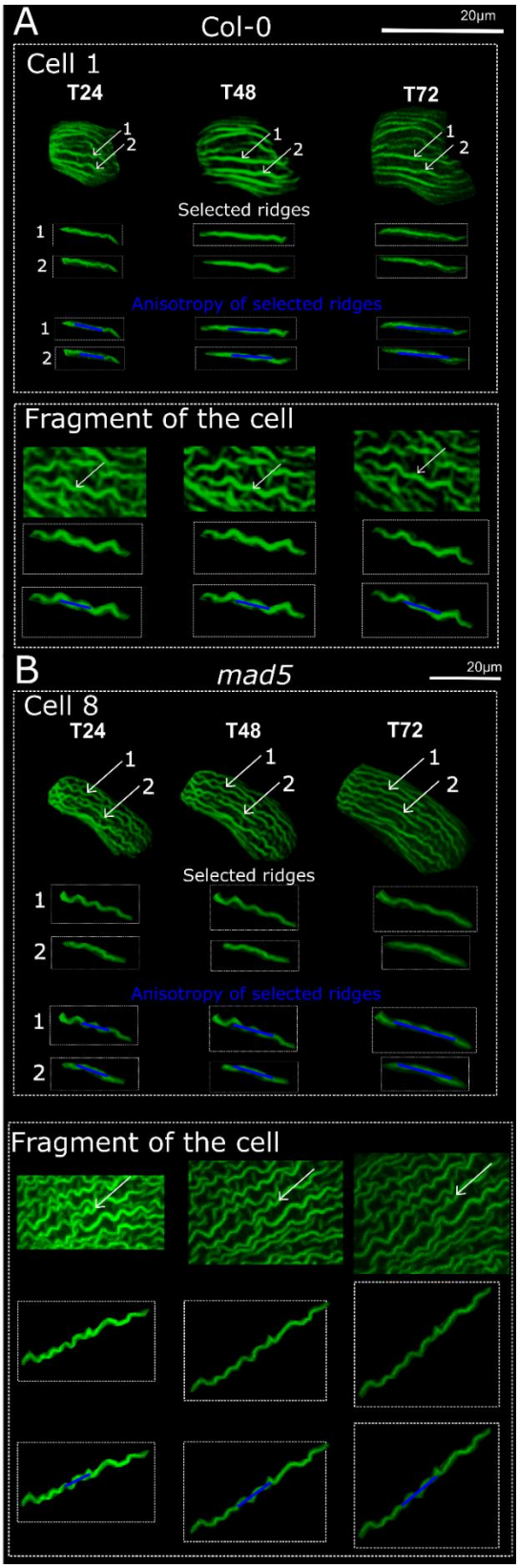

Fig. 4.33 Exemplary Col-0 (**A**) and *mad5* (**B**) cells with straightening ridges (corresponding to Col-0 Cell 1 and *mad5* Cell 8 shown in **Fig. 4.27**, as well as representative fragments of the largest Col-0 and *mad5* cells from **Fig. 4.31**). Arrows point to exemplary ridges that straighten during cell growth. Enlarged individual ridges, the same as pointed by arrows, are shown below, without and with anisotropy marked as blue line segments.

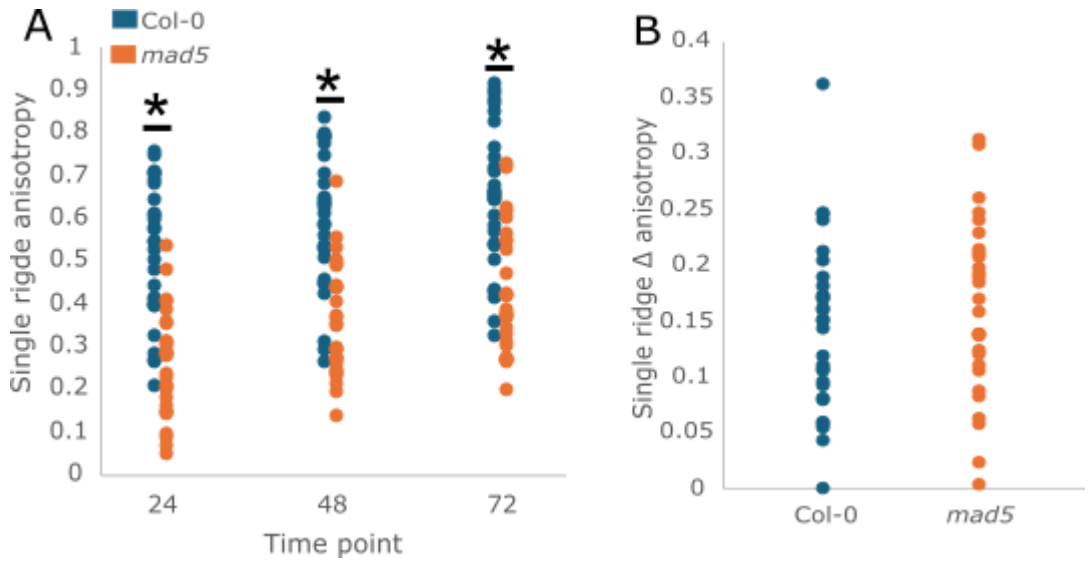

Fig. 4.34 (**A**) Anisotropy of individual ridges of Col-0 (29 ridges) and *mad5* (28 ridges). (**B**) Difference of the anisotropy between the last time point (T72) and the first time point (T24). Asterisks mark statistically significant differences of pairwise comparison between *mad5* and Col-0; p-value for Mann-Whitney test: T24 0.00000211, T48 0.000001, T72 0.0000109.

5. DISCUSSION

5.1 Raman spectroscopy reveals spatiotemporal heterogeneity of primary cell walls of Arabidopsis sepal epidermis and some phenotypic traits of the investigated mutants

Due to the dynamic nature, in particular the capacity for expansion and for continuous remodelling, primary cell walls play a fundamental role in the regulation of plant growth and development (Cosgrove and Park 2012, Cosgrove 2024). The composition and organisation of plant cell walls have been studied extensively (see comprehensive review by Cosgrove 2024A). The investigations often focused on one wall component, such as cellulose for which fibril alignment and its temporal dynamics during development were shown (Schmidt et al. 2010, Richter et al. 2011, Park 2012, Li et al. 2014, Wang and Hong 2016, Mollier et al. 2023, Morel and Gierlinger 2023), as well as pectins (Peaucelle et al. 2011, Haas et al. 2020) and xyloglucan (Sampedro et al. 2010, Günl and Pauly 2011), for which direct involvement in regulation of wall growth and mechanical properties has been postulated.

In the present investigation, we employed Raman microspectroscopy to quantify the overall chemical composition of individual, intact primary cell walls on the surface of Arabidopsis sepal. Such approach enabled subcellular analysis of the spatial heterogeneity of the walls and assessment of changes in the wall composition during sepal development.

5.1.1 Spatiotemporal heterogeneity of primary cell walls of sepal epidermis in Arabidopsis wild type and mutants

Comparison of Raman spectra obtained from epidermis of the stage 10 sepals, i.e. the sepals that were still growing, with spectra of stage 12, i.e. mature sepals (Smyth et al. 1990, Roeder 2021, Yadav and Roeder 2024), shows that the differences are mainly in the band signal intensity. The same is true for the comparison of spectra obtained from wild type and mutant sepals. However, Raman does not allow for direct quantitative comparison of spectra coming from measurements of different samples (Bowie et al. 2000A, Bowie et al. 200B, Agarwal 2019). Thus, we used the Multivariate Curve

Resolution-Alternating Least Squares (MCR-ALS) method (Felten et al. 2015) in order to compare the spectra quantitatively, by analysing the contribution of component spectra that were distinguished for each developmental stage and genotype. In some biological samples, such components identified by the multivariate curve resolution algorithm correspond to well defined sample components, like in the case of renal calculus (Piqueras et al. 2011, Piqueras et al. 2020). In the case of plant cell walls, however, the correspondence is blurred because of the similarity between chemical bonds of the wall polysaccharides (Chylińska et al. 2014).

In the present analysis of cell walls of Arabidopsis sepal epidermis, two component spectra were distinguished. Component 1 is enriched in ester-related signals, most notably the ν(C=O) band, at ~1740 cm^{-1}, and the relatively high signal of the 1447 cm^{-1} band (δCH, νC=C aromatic, δCH_2 in esters), consistent with contributions from esterified pectins and cutin (see **Table 4.3**). Component 2 shows a relatively high contribution of signal from cellulose, alongside cutin and pectin. Importantly, both the component spectra contain most bands of the major primary cell wall constituents; they differ in relative contributions rather than exclusive composition.

The two component spectra were similar both for the comparison of the two developmental stages and for the comparisons of the same stage in wild type and mutants. The overall spectral features of the mutants resembled those of Col-0 by more than 92%, suggesting that the changes in wall composition caused by mutations, which affect a single component of the primary cell wall, are rather subtle. Nevertheless, the contribution of the two components in the sets of Raman spectra obtained from the samples was different for the two developmental stages, and some differences in the contribution between the wild type and mutants were also revealed. In younger sepals of Col-0, *mad5* and *pme32*, the contribution of the two component spectra was similar, whereas in mature sepals, the Component 1 spectrum became dominant. This shift likely reflects a developmental transition in wall structure associated with maturation, in the course of which an increase in stiffness and altered polymer crosslinking related to cessation of cell wall expansion are expected. Interestingly, *xyl1* diverged from this pattern, showing domination of the Component 1 spectrum already in younger sepals and stronger than in other genotypes, domination of this component in mature sepal walls. Moreover, in *xyl1* sepals at the mature stage, the Component 2 spectrum showed the strongest difference from the corresponding wild type component among all of the

investigated mutants. On the other hand, in the spectra obtained from cell walls of mature *csi1* sepals, the contribution of the dominating Component 1 spectrum was lower than in the wild type. This suggests that the lack of α-xylosidase (Sechet et al. 2016) activity as well as malfunctioning guidance of CESA by microtubules (Bringmann et al. 2012, Mollier et al. 2023) may affect remodelling of the cell wall that takes place during the sepal maturation. In the case of *xyl1*, the wall maturation seems to be accelerated while in *csi1*, delayed. In the former case, it may be a direct mutation effect on mutation, as hemicelluloses affect the mechanical properties of cell walls (Park and Cosgrove 2015) that may be related to maturation. In the case of *csi1*, only indirect effects can be expected because *csi1* mutation is known to affect cellulose arrangement, growth anisotropy and growth coordination in later stages of sepal development, which lead to altered sepal size and shape (Mollier et al. 2023). Surprisingly, the quantitative analysis has not revealed any effects of *mad5* mutation, although the sepal shape and size of *mad5* are much stronger affected than those of *csi1* (Mollier et al. 2023, Trinh et al. 2024). Also, in the case of *pme32*, no mutation effects were revealed although a higher degree of pectin methylesterification, known to affect growth and mechanical properties of the walls, are expected in the mutant (Hongo et al. 2012). This, however, may be related to functional redundancy among PMEs. Nevertheless, explaining such phenotypes would require further studies.

Altogether, the component spectra analysis indicates quantitative differences in the cell wall composition between still growing and mature sepals, supporting *Hypothesis 1* that the primary cell wall composition of the Arabidopsis sepal epidermis undergoes developmental changes.. Moreover, the changes in cell wall composition are likely affected by mutations *xyl1* and *csi1,* in agreement with the second part of *Hypothesis 1* (the changes in cell wall composition can be affected by mutations). However, the observed effect is rather weak.

Raman spectroscopy also revealed spatial heterogeneity of the primary cell walls on the sepal surface. It allowed us to distinguish two wall portions, the ridged and non-ridged regions, in Raman maps of mature sepals. While both regions showed generally similar spectral profiles for samples of the examined genotypes, their qualitative comparison, focusing on the presence/absence of specific bands, revealed reproducible and region-specific differences. Two peaks, at 1172 cm^{-1} and 1240 cm^{-1}, were absent in the non-ridged portion of the wall but present in the ridged area. However, interpretation of such

the difference between the two regions was not possible because these bands are assigned to bonds present in most of the cell wall components (see **Table 4.3** in section **4.1.2 Assignment of spectrum peaks to primary cell wall components of ridged and non-ridged portions of primary cell wall**). Nevertheless, there are also more specific bands, at 1594 cm^{-1} and 1678 cm^{-1}, that differentiate the ridged and non-ridged wall regions. The first one, 1594 cm^{-1}, is associated with phenolic compounds in the cuticle, located likely mainly in the cuticular layer (Reynoud et al. 2021), and was detected only in the non-ridged cell wall portion. The second band, 1678 cm^{-1}, is characteristic of cutin (Gierlinger and Schwanninger 2007, Schmidt et al. 2009, Heredia-Guerrero et al. 2014, Bock et al. 2021) and was detected only in the ridged portion. These distinctions suggest a difference in chemical composition of the two regions and highlight that compositional heterogeneity can occur even within an individual cell wall. However, both compounds are located in the cuticle (Reynoud et al. 2021, Sasani et al. 2021) and thus the effect of the difference in cuticle proper orientation (e.g., polymer alignment relative to the laser beam) between the regions cannot be excluded, especially in the case of the cutin-characteristic band that most likely originates mainly from the folded cuticle proper.

Noteworthy, the qualitative comparison of band presence in wild type and mutant spectra revealed that the 1594 cm^{-1} band, associated with phenolic compounds, is consistently present in non-ridged wall regions of all the genotypes except *csi1*. This is a rather surprising phenotype trait of the *csi1* mutant, where CESA guidance by cortical microtubules is affected, but may reflect an altered composition of the cuticular layer, in which cellulose is also often present (Domínguez et al. 2017, Philippe et al. 2020, Reynoud et al. 2021). It can be speculated that malfunctioning CESA guidance affects the arrangement of cellulose fibrils in this layer, which in turn may have an influence on component interactions and eventually the layer composition. However, understanding this phenomenon requires further investigation.

When comparing the mutant spectra with those of the wild type, we also observed slight shifts in peak positions. The strongest shift was noted for non-ridged cell wall portions of *xyl1*, where the xylan-related band was shifted from 1310 to 1338 cm^{-1}. Such a spectral shift may result from the lack of α-xylosidase activity in modifications of xylan side chains. However, the shift was observed only in some of the examined samples, raising questions about the robustness of this finding. One possible explanation is that there are only a few structural changes in the xylan of mutant cell walls, and thus, in

many samples, they are below the resolution threshold of Raman spectroscopy. Alternatively, the effect might be confined to specific places/time points of epidermal cell morphogenesis. In such a case, additional investigations using other techniques, such as immunolabelling of hemicellulose epitopes, should complement Raman measurements. Our analysis also revealed reproducible but smaller spectral shifts with respect to wild type in the case of Raman spectra of other mutants (see **Table 4.3**). Similar shifts were observed in spectra obtained for Arabidopsis petals (Mazurek et al. 2017). However, it has to be kept in mind that in Raman spectroscopy, the position of bands and their signal intensities can vary due to technical and environmental factors such as slight differences in laser wavelength, temperature, or even the mounting method. This complicates straightforward comparisons across experiments or instruments (Bowie et al. 2000A, Bowie et al. 2000B).

Samples of *mad5* and *pme32* mutants did not present any unique bands but rather showed subtle changes in band intensity and shape, particularly in the 1098-1127 cm^{-1} region, which corresponds to cellulose and hemicellulose signatures. These variations may indicate altered wall composition, but the differences are not clear enough to draw any conclusions.

To sum up, qualitative comparison of Raman spectra showed that the cell wall composition is affected by mutations *xyl1* (the spectral shift of the xylan-related band) and *csi1* (lack of the band associated with phenolic compounds). Thus, *Hypothesis 1* (the cell wall composition is affected by the investigated mutations) is partly confirmed.

5.2 Putative compensation effect in cell wall composition of the investigated mutants

Raman spectroscopy enables simultaneous assessment of the contribution of various compounds in individual cell wall samples and has the advantage of spatial resolution, which allows detection of shifts in biochemical composition at the cellular level (Gigli-Bisceglia et al. 2020). It makes this method particularly well suited to detect compensatory responses, where the balance of wall polymers is adjusted to maintain cell wall integrity despite genetic perturbations (Vogler et al. 2015). Compensation refers to a shift in wall composition that occurs in response to changes in a specific component

or its deposition pattern. For example, disruption of cellulose synthase activity in the primary cell wall by mutation of *CESA3* or application of the herbicide isoxaben, which targets cellulose biosynthesis, activates ectopic lignification in leaves and basal parts of inflorescence stems of Arabidopsis (Delgado-Cerezo et al. 2012, Faria-Blanc et al. 2018). A classic example of compensation was observed in the *cesa3je5* mutant, where a reduction in crystalline cellulose was accompanied by increased pectin deposition (Li et al. 2014), illustrating the broad capacity of the wall to rebalance its components. Using Raman spectroscopy, we attempted to detect putative compensatory shifts in polysaccharide composition in the investigated mutants that would demonstrate the plasticity of wall remodelling.

In *pme32* samples the mutation leads to the statistically significant increase of relative contribution of the band related to esterified pectin. When the path of demethylesterification of HG in cell walls is affected in a mutant, the cell wall retains a higher degree of methylesterified pectins, which likely explains the increased signal of the peak 856 cm^{-1} characteristic for methylesterification of HG. This retained methylesterification likely leads to a softer pectin matrix due to reduced calcium crosslinking structures within the cell wall, as shown for *pme35* mutants (Hongo et al. 2012). In the *pme32* cell wall samples, the relative Raman intensity of the cellulose band was significantly increased, which may indicate structural compensation, possibly offsetting the mechanical softness of the methylesterified pectin matrix. Given the normalisation method used to estimate band contributions, an increase in the relative proportion of pectin and cellulose bands implies a relative decrease in hemicellulose band contribution. Noteworthy, the compensation analysis revealed an effect of the *pme32* mutation, although we were not able to reveal any effects using the other methods of Raman spectra comparisons discussed above.

In the *xyl1* mutant, the activity of α-xylosidase, known also as apoplastic glucoside hydrolase, is disrupted (Günl and Pauly 2011). Although the *xyl1* mutant phenotype is rather weak (Günl and Pauly 2011), the mutation affects substituents of XyG chains in the cell wall (Sampedro et al. 2010, Günl and Pauly 2011). Investigations of Arabidopsis hypocotyls, embryos and endosperm have shown that the *xyl1* mutation results in increased level of xylose substituents building the hemicellulose side chain, while in Col-0 the subunits are more diverse (e.g. glucose, galactose) (Günl and Pauly 2011, Sechet et al. 2016). This leads to the formation of less branched chains (Fry et al. 1993),

which can give lower signal intensity in Raman spectroscopy for the hemicellulose-related band (1313 cm^{-1}). Accordingly, in the *xyl1* sample spectra, we noted a decrease in the relative contribution of this hemicellulose signal. It is hypothesised in the literature that decreased content of XyG may be related to a low degree of pectin methylesterification, and these cell wall modifications affect longitudinal cell wall loosening during hypocotyl elongation (Sechet et al. 2016). Our analysis of compensation effect has not revealed a significant increase in pectin signal contribution, but the pectin band chosen for the analysis is related to esterified rather than de-methylesterified pectins. However, the significant increase in cellulose signal contribution that was detected may represent a compensation effect and likely affects the mechanical properties of the sepal walls in the mutant.

The *csi1* and *mad5* mutations indirectly influence the arrangement of cellulose microfibrils. In *csi1* CESA guidance by cortical microtubules is damaged. The compensation effect analysis has not revealed significant changes in the relative contribution of the cellulose signal in the *csi1* samples. However, *csi1* exhibits a significantly decreased contribution of signal from esterified, i.e. softer pectin. This may suggest that to compromise the altered cellulose microfibrils organisation, the level of demethylesterified pectins in the matrix is increased. Mechanical properties of the wall may also depend on hemicelluloses, especially the branching of the chains. For example, hemicelluloses in hardwoods tend to be less branched to confer stiffness (Berglund et al. 2020). However, our analysis has not shown any significant changes in the contribution of the hemicellulose signal. On the other hand, although the sepals of *mad5* mutant exhibit the most pronounced phenotype among the examined mutants, the compensation effect analysis has not shown any statistically significant differences between wild type and the mutant. However, as discussed below, *mad5* is the only mutant for which Raman analysis revealed significantly decreased anisotropy of cellulose fibril alignment.

To sum up, the analysis of the relative contribution of signals originating from the main wall polysaccharides points toward the existence of a compensatory mechanism that modulates cell wall composition in response to different perturbations in cell wall mutants. For instance, changes in HG methylesterification may be partially buffered by altered cellulose content, while changes in cellulose alignment by altered HG methylesterification. These results suggest that cells of Arabidopsis sepal epidermis are able to reorganise wall components to decrease mutation effects on growth and shape

robustness, which supports *Hypothesis 3* that deficiency of a cell wall component in Arabidopsis mutants activates a compensatory mechanism.

5.3 Raman spectroscopy reveals structural anisotropy of two components of primary cell walls on the Arabidopsis sepal surface

Raman spectroscopy can be applied to acquire information about the structural anisotropy of examined samples. In the case of cell wall components, the dependence of signal intensity of Raman bands on the orientation of the laser polarisation plane is well known for bands related to cellulose, which is the main component forming aligned fibrils in secondary cell walls (Agarwal and Ralph 1997, Agarwal 2006, Gierlinger et al. 2019). Due to stabilization by hydrogen bonds, cellulose chains can form highly ordered structures, in contrast to hemicellulose, the chains of which are decorated by a variety of differently positioned side chains (Zeng et al. 2016, Makarem et al. 2019, Zhang et al. 2023). Two levels of organisation can be distinguished for cellulose. The first one is related to the molecular organisation within the cellulose microfibril, where crystalline and/or amorphous structures can exist (Festucci-Buselli et al. 2007). The main structural differences between amorphous and crystalline cellulose are in the length of the cellulose chains and the way hydrogen bonds are formed (Yu and Wu 2010). The second level of cellulose organisation refers to the arrangement of cellulose microfibrils, which can be aligned to various extents. The extent of cellulose alignment can be quantified by comparing signals from cellulose-related bands, which are polarisation-sensitive, like the 1098 cm^{-1} band, and non-sensitive, like the 1122 cm^{-1} band, in the same spectra. Comprehensive studies show that cellulose can be highly organised and amplify the signal of the specific Raman spectrum bands in the case of secondary cell walls (Agarwal 2006, Gierlinger et al. 2008, Gierlinger et al. 2010, Makarem et al. 2019, Felhofer et al. 2021). Such analyses were conducted, for example, to assess cellulose orientation in secondary cell walls of secondary xylem of trees (e.g. Agarwal 2006, Zhang et al. 2023), hypodermal fibres of *Equisetum hyemale* L. shoots (Gierlinger et al. 2008), and the level of cellulose crystallinity in bleached hardwood and kraft pulp (Agarwal 2022).

While numerous investigations were performed on relatively thick secondary cell walls, where cellulose microfibrils are well aligned (Makarem et al. 2019), there is only a limited number of investigations on the cellulose microfibril alignment in primary cell

walls (Szymańska-Chargot et al. 2011, Chylińska et al. 2014, Borowska-Wykręt and Dulski 2019, Bock et al. 2021). The reasons are the technical difficulties in sample preparation and the fact that the primary cell walls are usually very thin (Derbyshire et al. 2007). For example, in Arabidopsis petals, the primary cell wall is approximately 300-500 nm thick, with an additional 200-300 nm contributed by the cuticle (Mazurek et al. 2017). These structural constraints make it particularly difficult to isolate reliable cellulose-related Raman bands, especially those indicative of microfibril orientation, without signal interference from the cuticle. We nevertheless attempted to assess the structural anisotropy of primary cell walls of Arabidopsis sepal epidermis using Raman spectroscopy. When analysing spectra obtained from individual samples at different polariser orientations, we recognised two regions that were polarisation-sensitive, one related to cellulose and the other to cuticle components.

The analysis of changes in the intensity ratio of cellulose bands 1095 and 1120 cm^{-1} accompanying polariser angle changes, provided evidence of some level of cellulose microfibril organisation in primary cell walls of all the genotypes. Changes in band intensities were consistently observed for Col-0 and the mutants, but were significantly smaller in *mad5* samples than in the wild type. This shows that anisotropy of cellulose fibril arrangement can be detected in primary cell walls and that the degree of microfibril alignment varies between genotypes.

The role of cellulose fibril arrangement in the regulation of anisotropy of cell wall expansion is comprehensively documented (see section **1.1.4 Cell wall as a composite material**), while the relationship between this arrangement and microtubule arrangement was postulated even before the microtubules were actually discovered (Green 1962, Probine and Barber 1966). Also, recent investigations show that cell elongation in hypocotyls is dependent on cell wall architecture but not on the overall crystalline cellulose content (Xin et al. 2020). Therefore, phenotypes of *csi1* and *mad5* mutants (reduced elongation, altered organ shapes) are not surprising. Our recent investigations, using Atomic Force Microscopy, of the cellulose microfibril arrangement on the protoplast facing wall surface showed that alignment of cellulose microfibrils is locally higher in *csi1* than in Col-0 sepal epidermis (Mollier et al. 2023). Also, studies using Atomic Force Microscopy performed on Arabidopsis hypocotyls demonstrated that cellulose alignment in the most recently deposited layer of epidermal cell walls exhibits some organisation, and the *csi1* mutant presents a higher level of cellulose

alignment (Xin et al. 2020). The present investigations on sepal epidermis surface show that the extent of cellulose alignment in *csi1*, manifested by Raman signal changes in relation to polariser orientation, does not differ significantly from that of Col-0. However, the Atomic Force Microscopy visualises cellulose alignment only on the wall surface, while Raman spectroscopy used in this work enables measurements of cellulose alignment across the entire cell wall thickness.

Interestingly, in the case of *mad5,* wall samples did not show statistically significant differences in composition from Col-0, although *mad5* plants have a clear phenotype, including reduced leaf and seedling size. Furthermore, the sepals of *mad5* mutant exhibit the most pronounced phenotype among the examined mutants, as manifested by the altered sepal shapes and unique ridge patterns. These features are likely related to the significant reduction in cellulose microfibril alignment in *mad5*, revealed with Raman measurements, emphasizing the importance of microtubule-mediated cellulose organisation in the regulation of growth anisotropy. The reduction in cellulose microfibril alignment in *mad5* may be attributed to disordered cortical microtubule arrays, as *mad5* and related *katanin* mutants (*ktn1*) display decreased levels of the microtubule severing enzyme Katanin (Brodersen et al. 2008). Katanin deficiency leads to unordered microtubule arrays in petiole and cotyledon cells (Komis et al. 2017). Also, in meristematic cells of the shoot apex in the Arabidopsis *botero* mutant (one of the *katanin* alleles), the anisotropy of microtubule arrays is significantly lower (Uyttewaal et al. 2012). In addition to phenotype traits of *mad5* that could be explained directly by cytoskeletal defects, the sepal surface sculpture in *mad5* exhibits traits that could be explained by altered sepal growth or altered formation of cuticle proper. Some authors propose the existence of nanoparticles known as cutinsomes, which are formed by the self-assembly of cutin monomers transported from lipid bodies in the cytoplasm to the cell wall (Stępiński et al. 2020). These structures have been implicated in cuticle development, particularly in tomato fruit (Segado et al. 2020). Although the precise role and dynamics of cutinsomes remain to be clarified, altered cutin deposition in which cutinsome trafficking may be involved may contribute to the observed surface phenotype in *mad5* sepals.

Only few reports refer to polarisation-dependent Raman signal from cuticle components (Bock et al. 2021, Sasani et al. 2021). This phenomenon was described for bands characteristic of epicuticular wax, i.e. 1632 cm^{-1}, 1712 cm^{-1} and 2900 cm^{-1}, of a thick

cuticle covering the Norway spruce (*Picea abies*) needle epidermis, where the epicuticular wax layer was thick enough to distinguish it from the remaining cuticle and to separate the signal from the two layers (Sasani et al. 2021). The polarisation dependence was attributed to coumaric acid and aliphatic chains of the epicuticular wax that are oriented perpendicular to the needle surface. Bock et al. (Bock et al. 2021) distinguished three types of cuticle compound organisation: crystalline structure not aligned, crystalline structure aligned, and amorphous structure. Every type of organisation results in different responses to polariser changes. In the case of an amorphous wax structure, the signal intensity is not affected by the polarisation plane. However, when the waxes are arranged in a specific way, the signal intensity depends on the polarisation of the laser beam. Thus, in the cuticle layer of the spruce needle, where the compounds are not aligned and comprise an amorphous structure, their signal intensity does not change with the polarisation plane (Sasani et al. 2021).

Raman spectroscopy was successfully applied to investigate changes in microchemistry of tomato cuticle during fruit development and revealed formation of layers rich in specific components like phenolics, waxes or flavonoids (González Moreno et al. 2022). In Arabidopsis, the stem cuticle investigation using Raman spectroscopy showed that it contains mainly cutin, a small amount of cuticular waxes and less phenolic compounds than tomato (Mateu et al. 2016). However, polarisation-dependent Raman signal from cuticle components has not been shown for Arabidopsis yet. In the present investigations of Arabidopsis sepal epidermis, Raman analysis revealed orientation-dependent signal variation in the 1500-1700 cm^{-1} region, corresponding to cuticle-related components such as cutin and waxes. The consistent polarisation response across all genotypes, including Col-0 and all the investigated mutants, suggests that certain lipidic components of the cuticle exhibit a significant degree of molecular alignment. The minimal to maximal signal ratio did not differ significantly between genotypes, indicating that mutations affecting the primary cell wall do not substantially disrupt this aspect of cuticle organisation.

To sum up, the presented results provide experimental confirmation od *Hypothesis 2*, demonstrating that the primary cell walls in Arabidopsis sepal show structural anisotropy in two components, cellulose and cutin/wax, which to some extent depend on the genotype.

5.4 Advantages and disadvantages of Raman microspectroscopy application in investigations of primary cell walls

Studies of primary cell wall composition often relied on bulk extraction and biochemical assessment of wall polymers, such as cellulose, hemicelluloses, and pectins, typically using whole tissues or organs (Zablackis et al. 1995, Bonaventure et al. 2004, Tsugawa et al. 2019). These approaches, while informative, average out local variability and exclude assessment of spatial or developmental differences within the walls or tissues.

One of the few techniques which allows for the simultaneous, *in situ* assessment of all the chemical components of a sample is Raman microspectroscopy. As a non-destructive technique with label-free detection of multiple cell wall polymers in a single measurement, Raman microspectroscopy facilitates the direct *in situ* analysis of native cell wall architecture without the need for chemical fixation, staining, or extraction of the primary cell wall components (Xu et al. 2018, Saletnik et al. 2021). This capability is crucial as it preserves the structural and chemical integrity of the cell wall in its natural context. Raman microspectroscopy has high chemical specificity by exploiting the unique vibrational spectra of molecular bonds within key wall polymers such as cellulose, pectins, and hemicellulose (Gierlinger and Schwanninger 2007). This specificity enables the spatial mapping of these polymers within complex tissues, providing insights into their distribution and relative abundance (Zeise et al. 2018). Raman microspectroscopy also achieves subcellular spatial resolution, allowing resolution of chemical heterogeneity not only between different cell types but also within individual cell walls or discrete wall subdomains (Chylińska et al. 2016, Sasani et al. 2021, Bock et al. 2021). This level of detail is particularly valuable for understanding the intricate architecture and dynamic remodelling of primary cell walls during development.

While absolute quantification remains challenging due to factors such as signal variability and orientation effects, comparisons of Raman intensity ratios and polarisation analyses have proven useful for semi-quantitative assessments (Sasani et al. 2021). For example, the degree of cellulose microfibril alignment can be inferred from polarisation-dependent Raman signals, offering important clues about structural anisotropy of cell walls which was already used for secondary cell walls of *Picea abies* where Raman measurements showed that cellulose is organised differently depending

on the cell wall layer (Gierlinger et al. 2010). Raman microspectroscopy also enables monitoring of spatial and temporal changes in cell wall chemistry within the tissue (Chylińska et al. 2016). This facilitates investigations on how polymer composition and structure evolve during organ growth, differentiation, and response to environmental conditions.

Despite these advantages, Raman microspectroscopy also presents several important limitations when applied to living plant tissues. One key drawback is its limited penetration depth. Typically, confocal Raman microspectroscopy probes only the surface layers of the tissue, making it difficult to access deeper cell wall regions without physical sectioning or chemical clearing (Morel and Gierlinger 2023). Additionally, the weak Raman signal of some biopolymers, particularly hemicelluloses, combined with the high water content in living tissues, often results in low signal-to-noise ratios that challenge the detection and interpretation of these components. Another significant challenge is spectral overlap and background fluorescence. Many cell wall polymers share similar chemical groups, causing overlapping Raman bands that complicate unambiguous identification. In particular, the wall polysaccharides share similar chemical structures, leading to overlapping Raman spectral bands due to vibrations of common functional groups, as in the case of cellulose and hemicellulose (Gierlinger et al. 2012, Zhang et al. 2017B). Finally, the sensitivity of Raman spectra to experimental conditions introduces variability that complicates direct comparisons between different samples or over time (Bowie et al. 2000B). Variations in tissue hydration, laser focus, and sample positioning may alter spectral output, requiring careful experimental approach and controls to ensure meaningful interpretation (Bowie et al. 2000B). These limitations highlight that while Raman microspectroscopy is a powerful tool, it should be kept in mind that spectra analysis always has to be performed with caution.

Nevertheless, Raman spectroscopy remains widely used in plant research, including, for example, analysing pectin dynamics, cell wall composition, and is even used for the identification of ornamental plant cultivars (Zhang et al. 2017, Juárez and Kurouski 2024). Many studies have acknowledged the spectral variability, particularly in biological samples, and have still drawn meaningful conclusions by focusing on trends and relative changes rather than absolute values. In that sense, while Raman has its disadvantages, it is still a powerful and informative technique as long as the data are interpreted cautiously and in the context of other observations.

5.5 Emerging pattern of cuticular ridges depends on the growth of the outer periclinal cell walls and less so on the wall geometry

The striking and not fully understood phenomenon that accompanies the late stages of development of the Arabidopsis sepal is the emergence of an elaborate cuticular pattern, which was followed in the present investigation using *in vivo* imaging. Plant cuticles have been extensively studied in relation to their structure (see e.g. Koch and Ensikat 2008, Mazurek et al. 2017) and function (Riederer and Müller 2006, Whitney et al. 2009, Buschhaus and Jetter 2011, see table in Skrzydeł et al. 2021). Investigations focusing on the mechanical properties of cuticle were performed mainly on cuticles of fruits, especially tomato (Benítez et al. 2021, Reynoud et al. 2021, Reynoud et al. 2023), while in the case of thin cuticles covering flower organs, direct mechanical measurements are technically challenging and thus available data are scarce (Domínguez et al. 2017, Skrzydeł et al. 2021, Airoldi et al. 2024). One of striking traits of plant cuticle, closely related to its various functions, is a variety of patterns on the cuticle surface, which are formed by epicuticular waxes and/or the cuticle proper. These patterns can differ between plant species or organs of the same plant, like leaves (Jenks et al. 2002, Cheng et al. 2019), flower organs (Huang et al. 2017, Hong et al. 2017, Mazurek et al. 2013), and stems (Jenks et al. 2002). Various models have been proposed to explain how specific surface patterns, such as cuticular ridges, are formed (Martens 1933, Kourounioti et al. 2013, Huang et al. 2017, Airoldi et al. 2021, Lugo et al. 2023). However, despite extensive characterization of cuticle structure, chemical composition, and surface patterns, the mechanisms governing the emergence of specific topographies, such as cuticular ridges, require further empirical investigations and complementary modelling.

Previous studies have demonstrated that a proper rate of cutin biosynthesis is essential for the formation of cuticular ridges. Moyroud et al. (2022) reported that chemical and genetic interference with cuticle production in *Hibiscus trionum* cultivars and related species leads to modification of the cuticular pattern of mature petals. In the case of Arabidopsis sepal surface, mutants such as *cus1*, *cus2*, and *cdr*, in which cutin polymerization or precursor production is affected, display smooth epidermal cell surface (Hong et al. 2017, Panikashvili et al. 2009). While these findings underscore the importance of biosynthesis and delivery of cuticle precursors, they do not explain the mechanism of the emergence of specific surface patterns during the formation of ridges.

This suggests that, beyond cutin deposition, additional factors such as the composition and mechanical properties of cuticle and the underlying cell wall also contribute to cuticular patterning. Support for this postulate comes from studies on chemical composition of petal cuticles in *Hibiscus* (Moyroud et al. 2022) and Arabidopsis (Mazurek et al. 2017), which show that the formation of cuticular ridges (striation in *Hibiscus*) and the pattern itself are related to cuticle chemistry. Observations of cross-sections of petal or sepal superficial cell walls covered by ridges show that ridges comprise folded cuticle proper of uniform thickness and underlying presumably pectin- and cellulose-rich domains (Mazurek et al. 2017, Airoldi et al. 2021, Skrzydeł et al. 2021). This implies that polysaccharide components of the primary cell wall contribute to ridge formation. Importantly, it is expected that the cell wall and the overlying cuticle layers differ in their physical properties, such as density and stiffness, which could affect how forces are distributed at the surface (Airoldi et al. 2021, Lugo et al. 2023, Airoldi et al. 2024). Recent mechanical models of cuticular ridges formation show that formation of cuticular pattern does not depend on properties of the cuticle proper alone, as was assumed in previous models (Kourounioti et al. 2012), but also on interactions between the cuticle and the cell wall, as well as anisotropy and timing of the cell wall growth (Airoldi et al. 2021, Lugo et al. 2023). The models explain the mechanism as buckling of cuticle proper, i.e. mechanical instability that is triggered by compressive stress in a bilayer system, which comprises a relatively soft substrate – the cuticular layer, covered by a stiff film of cuticle proper (Lugo et al. 2023, Airoldi et al. 2024). The compressive stress in the plane of the cuticle proper is the prerequisite for buckling. The models assume that it originates from the mismatch of cell wall and cuticle expansion and is thus related to cell growth and geometry. To verify these models, the identification of causal relationships between growth and geometry of outer periclinal walls of epidermal cells and the emerging pattern of cuticular ridges is required. The present investigations have provided some of this information. Equally important would be the assessment of the mechanical properties of the cuticle proper and the underlying cell wall layers in intact cell walls of Arabidopsis sepal at the time of ridges formation (Airoldi et al. 2024).

To address the question of putative causal relationships between growth and geometry of outer periclinal walls of sepal epidermal cells and emerging pattern of cuticular ridges, we analysed cuticular ridges formation on the surface of Arabidopsis sepal. We

examined both wild type and *mad5* mutant, which has a strong phenotype regarding sepal morphology, growth and cuticular pattern. The present investigations show that *mad5* displays a more complex cuticular pattern on its sepal epidermal surface than the wild type. Sepals of *mad5* are smaller and open earlier than those of the wild type (Trinh et al, 2024), while giant cells of their epidermis are generally shorter. Moreover, Raman measurements showed that the structural anisotropy of cellulose arrangement is lower in *mad5* cell walls. We thus expected differences in growth anisotropy between the wild type and mutant.

Our time-lapse imaging of growing sepal epidermis showed that cuticular ridges are formed on the initially smooth surface when the epidermal cells stop dividing but are still expanding, in agreement with earlier reports (Hong et al. 2017). Emergence of cuticular ridges on expanding cell walls was also reported for *Hibiscus trionum* petals, where striation appears in the distal part of petals before the growth cessation (Kourounioti et al. 2013). Our most important observation in terms of model verification is that on the surface of cells representing all the shape groups defined in this study (from nearly isotropic to strongly elongated cells), the newly formed ridges are in most cases parallel to the direction of maximal growth (PDGmax), at both cellular and subcellular scales. This is in agreement with our *Hypothesis 4* (the initial pattern of cuticular ridges is influenced by cell growth) and also with predictions of the models, which assume that ridges are formed due to buckling of the cuticle proper (Kourounioti et al. 2013, Airoldi et al. 2021, Lugo et al. 2023). The growth that we assessed for the sepal cells is not strongly anisotropic; in fact, it is much less anisotropic than that reported for *Hibiscus trionum* petals (Lugo et al. 2023). In the case of Arabidopsis sepals, the mean growth anisotropy during the time interval when ridges appear is circa 1.2, while in *Hibiscus* petals, it is close to 2. This is likely the reason why Arabidopsis sepals are usually covered by more or less wavy ridges, unlike the regular striation on the surface of *Hibiscus* petals. Nevertheless, in Arabidopsis sepals, the direction of maximal growth is usually parallel to the long cell axis, and ridges follow this orientation, similar to the *Hibiscus* petal striation.

We have not found any relation between the waviness of ridges and growth anisotropy assessed at the cellular scale. In particular, the growth anisotropy in *mad5* was similar to Col-0, while the ridges were apparently more wavy in the mutant. However, it has to be kept in mind that growth anisotropy was assessed for cell outlines (defined by vertices

that are three-way junctions of anticlinal cell walls) and not for the surface of the outer periclinal walls. These walls were more curved in the mutant, already during the formation of the ridges. This points to the postulated relationship between the cuticular pattern and cell wall geometry (*Hypothesis 4*). The relationships between the cuticular pattern and cell wall curvature were captured in the three-dimensional simulations of *Hibiscus trionum* petal cuticles, where striation parameters depended on wall curvature and cuticular pattern emergence began in flatter regions (Lugo et al. 2023). The ridges generated in the model were, however, always straight. In Arabidopsis sepals, we found that the relationship between ridges orientation and directions of maximal or minimal curvature is much weaker than the relationship with maximal growth direction. Only in the shape group 1 of Col-0 (nearly isodiametric cells), the orientation of newly formed ridges is usually perpendicular to the direction of maximal curvature, while there is no relation in other Col-0 groups and in *mad5*. However, there seems to be a relation between the overall wall curvature and ridges waviness: as already mentioned, high waviness and complex pattern of ridges in *mad5* can be related to the fact that the outer periclinal walls of *mad5* cells are more curved than Col-0 already during the ridges formation, and the curvature in *mad5* is less homogeneous. These observations are in agreement with *Hypothesis 4*.

The sepals of *mad5* display a more complex cuticular pattern than wild type, despite no significant differences in cell wall and cuticle composition or in structural anisotropy of cuticle components, shown by Raman measurements. Only indirect effects can be proposed. In *mad5*, the altered structural anisotropy of cellulose arrangement, more curved cell walls and less elongated cell outlines may generate mechanical conditions that are much different from those in the wild type. The model by Lugo et al. (2023) shows that the cell wall mechanics affect the cuticular pattern formation. Another reason for the high complexity of the *mad5* ridges pattern may be in the overall shape of the mutant sepal. While ridge formation in wild type occurs over the still-closed bud surface, in *mad5*, the bud opens already during the ridge formation. Thus, the *mad5* sepals may be bent away (outward) by emerging inner flower organs, i.e. external forces may be applied to the abaxial sepal epidermis, additionally modifying the mechanical conditions.

The *mad5* mutant, with its altered growth dynamics, less elongated cells, and more complex ridge pattern, reinforces the idea that ridge patterning arises from the dynamic

interplay between cell geometry, growth behaviour, and mechanical properties of the wall – cuticle system during development. Although our data primarily focus on cell shape and growth direction, other mechanical factors, such as turgor pressure, cell wall and cuticle material properties, and overall organ geometry, may also contribute to ridge formation. Future studies combining mechanical measurements with growth and ridge formation analyses could help to test these possibilities. One more major question that remains open for further investigation is on adding the new material to the cuticle proper prior to the ridges formation (Skrzydeł et al. 2023). Buckling of a bilayer system is a mechanical instability that takes place when a threshold of compressive stress is surpassed in the stiff film. It means that prior to buckling, new material has to be added to the cuticle proper, such that it does not grow in thickness, but the cuticle is already under in-plane compressive stress, and the stress increases up to the threshold during the addition of the new material. Such addition of new material to the cuticle resembles an intussusception (Dumais 2013). However, intussusception requires the tensile rather than compressive in-plane stress, which is not expected in the cuticle proper at this particular developmental stage preceding the ridges formation. Thus, the mechanism of material addition and its role in buckling require further studies.

5.6 Pattern of cuticular ridges undergoes dynamic remodelling during the cell wall growth

When investigating sepal development in Arabidopsis *cus2* mutant, in which synthesis of cutin is affected, Hong et al. (2017) showed that cuticular ridges are normally initiated on the mutant sepal surface, but the cuticle smoothens during later expansion of epidermal cell walls. The normal initiation of ridges in the mutant is explained by the partly redundant functions of CUS2 and closely related CUS1. However, the observation of cuticle smoothening in *cus2* reveals that the maintenance of cuticular pattern requires continuous supply and incorporation of cutin precursors to the cuticle proper of expanding cell walls. Moreover, it implies that the structure and composition of the cuticular layer, which underlies the cuticle proper, folded to form cuticular ridges, is such that the wrinkled cuticle proper can flatten upon tension. Namely, the phenomenon of cuticle smoothening depends not only on the properties of the cuticle proper itself but also on the underlying cuticular layer that has to be soft enough to undergo such large

volumetric deformation. Noteworthy, a smoothening was also reported for the cuticle of *Hibiscus trionum* petals, in experiments where buckling of the cuticle was induced by stretching of petal samples from the striation region in the developmental stage prior to striation formation (Airoldi et al. 2021). Due to the Poisson effect, stretching in one direction leads to contraction and resulting compression in the orthogonal direction, which in turn leads to buckling. In some samples, such induced striation was to some extent or partly smoothened when the samples were left in a relaxed stage for a considerable time after the stretching force removal, and returned to their initial dimensions. The striation reversion after removal of compressive stress corresponds to the disappearance of cuticular ridges on the expanding surface of Arabidopsis sepal when expansion is not balanced by the addition of new cuticle material. Both phenomena depend on the mechanical properties of the cuticle proper and the underlying cuticular layer. The relatively long time required for reversion of the sample deformation is likely the osmoelastic behaviour (Hejnowicz 2011).

The above cases show that the cuticular pattern is not permanent. Accordingly, in the wild type and *mad5* Arabidopsis sepals, it may be expected that during expansion of the wall surface covered by ridges, the cuticular pattern is not simply scaled (magnified) to keep up with the expansion of the underlying primary wall, but that some modification of the pattern may take place because of the wall expansion (*Hypothesis 5*). Thus, our investigations focused on the changes of cuticular pattern in time and on what can be learnt on properties of cuticle layers on this basis.

Observations performed at the subcellular scale showed that ridges do not maintain their initial shape over time but tend to straighten as cells expand. Straightening may be a result of anisotropic scaling and implies that the cuticular layer is indeed a soft material that facilitates changes in the shape of ridges. This supports the idea that cuticular pattern is influenced by the mechanical properties of the bilayer system (Lugo et al. 2023, Airoldi et al. 2024). Importantly, the straightening is not homogeneous across the cell surface. Thus, it required following individual ridges over time to be observed. This points to a locally controlled mechanism of ridges deformation, possibly dependent on local growth heterogeneity of the underlying cell wall. Such growth heterogeneity of epidermal surface at the subcellular scale has been reported for Arabidopsis leaf epidermis (Elsner et al. 2025) and is likely a common feature of epidermal cells in leaf-like organs (Meyer and Roeder 2014, Hong et al. 2024).

In addition, the *in vivo* imaging of the expanding surface of Arabidopsis sepal covered with cuticular ridges revealed the appearance of new ridges between the existing ones. It was observed in regions of high local surface expansion where the surface area between the already existing ridges significantly increased. Some of the secondary ridges were oriented perpendicular to the pre-existing ridges, especially in Col-0, where new ridges were short and less distinct. In *mad5*, the new ridges were often longer than in Col-0 and parallel to the earlier formed ones. The formation of new ridges is most likely a manifestation of a secondary mechanical instability that takes place when the local compression generated by mismatch in cell wall and cuticle expansion between the already existing ridges, reaches the second buckling threshold (Lugo et al. 2023). It is yet another observation supporting the plastic behaviour of the relatively soft cuticular layer underlying the cuticle proper.

All the findings discussed above support *Hypothesis 5* that the pattern of cuticular ridges is changing over time. Dynamic remodelling of cuticular ridge patterns may play important roles in the physiology and mechanics of plant development (Lugo et al. 2013, Chen et al. 2025). These changes could influence the epidermal surface properties by modulating cuticle permeability and water retention, which are critical for controlling transpiration and preventing desiccation (Buschhaus and Jetter 2011, Whitney et al. 2009). Additionally, the changing pattern and elasticity of the cuticle might facilitate mechanical processes involved in flower opening, acting like “hydraulic cushions” that assist tissue expansion and deformation during organ maturation (Airoldi et al. 2021). A more complex, three-dimensional surface structure could also enhance water capture or interaction with small particles, similar to the function of trichomes (Buschhaus and Jetter 2011). Furthermore, ridges may provide protection for stomatal complexes, optimizing gas exchange while serving as a barrier against environmental stresses (Samuels et al. 2008). Although these potential functions align with known cuticle properties and mechanical behaviour, direct studies on how dynamic ridge remodelling contributes to these processes remain lacking. Therefore, this represents a promising area for future research integrating biomechanics, chemistry and physiology of the functional interface between plant surfaces and their environment.

6. CONCLUSIONS

- Raman spectroscopy revealed ontogenetic changes in primary cell wall composition during maturation of the *Arabidopsis thaliana* sepal epidermis. These changes, identified and quantified using the two-component MCR-ALS algorithm, are reflected in differences in signal intensity and contribution of the two Component spectra. They are quantitative rather than qualitative and indicate compositional remodelling of the cell wall during organ maturation. This confirms the first part of *Hypothesis 1*.

- In the Raman maps of superficial sepal walls, two regions with assigned spectra can be distinguished: one for the cell wall located between the cuticular ridges, and another for the wall covered by ridges. These two regions showed slight compositional differences, including additional bands in ridge-covered walls. Moreover, qualitative differences between the investigated mutants and the wild type were revealed. In the *csi1* mutant, one of the cuticle-related bands was absent from the wall region located between ridges, which is most likely an indirect mutation effect. In the *xyl1* mutant, a shift in the hemicellulose-related band was observed, which is probably related to the lack of α-xylosidase activity in the mutant. This partially confirms the second part of *Hypothesis 1*.

- Polarisation-sensitive bands were identified within the primary cell wall of Arabidopsis sepal, which were a manifestation of its structural anisotropy. The polarisation-dependent bands were related not only to cellulose but also to the cuticle components. Cellulose was aligned within primary cell walls to a similar extent in wild type and the investigated mutants, except for *mad5*. This *mad5* phenotype is similar to other katanin mutants in which microtubule dynamics is affected. Structural anisotropy of cuticle components of Arabidopsis sepal, similar in the wild type and all of the investigated mutants, is a novel observation. It suggests that even the thin cuticle of Arabidopsis sepal epidermis exhibits some degree of ordered organisation, although further investigations at higher resolution are needed to explain this organisation in a more detailed way. *Hypothesis 2* is confirmed.

- Comparison of the contribution to the spectra of Raman signals related to pectins, cellulose and hemicellulose facilitated indirect assessment of the relative contribution of the three main polysaccharides in individual wall samples of wild type and the investigated mutants. In mutants, a decrease in the signal assigned to one component was accompanied by an increase in others. This is likely a manifestation of a compensatory adjustment mechanism to maintain cell wall structure and mechanical properties despite compositional changes. *Hypothesis 3* is confirmed.

- Cuticular ridges that decorate the abaxial surface of Arabidopsis sepals are formed on initially smooth outer periclinal walls when the sepal surface is still expanding. The pattern formed by cuticular ridges depends on the anisotropy of the surface expansion and on its geometry. In agreement with models explaining the ridges formation as a mechanical buckling, the orientation of newly formed ridges was most often parallel to the principal direction of maximal growth at both the cellular and subcellular scales. The relation between ridges orientation and directions of surface curvature is much weaker. However, the unique complexity of ridges pattern on the surface of *mad5* sepals seems to be related to the high curvature of mutant epidermal cells. This confirms *Hypothesis 4*.

- The extent of alignment and morphology of cuticular ridges change during the sepal surface expansion. The anisotropy of the initial ridges patterns either increased or decreased over time. The decrease in anisotropy was often related to the formation of new short ridges that were sometimes perpendicular to the initially formed ones, while the anisotropy increase was associated with the straightening of already existing ridges. This supports *Hypothesis 5* that the pattern of cuticular ridges changes over time. Ridges alignment was often higher near cell borders and varied between cell wall regions, particularly in elongated cells, suggesting variation in the mechanical state of the wall regions. The changes in anisotropy of the cuticular pattern during wall expansion are likely a manifestation of stiffness heterogeneity, i.e. the stiff film formed by cuticle proper is covering the relatively soft cuticular layer, in agreement with models of ridges formation that assume buckling.

7. REFERENCES

Abdel-Massih RM, Baydoun EA-H, Brett CT. 2003. In vitro biosynthesis of 1,4-β-galactan attached to a pectin-xyloglucan complex in pea. *Planta*. **216**(3): 502–511. doi:10.1007/s00425-002-0861-y

Agarwal UP, Atalla RH. **1986**. In-situ Raman microprobe studies of plant cell walls: Macromolecular organization and compositional variability in the secondary wall of *Picea mariana* (Mill.) B.S.P. *Planta.* **169**: 325-332. doi: 10.1007/BF00392127

Agarwal UP, Ralph SA. **1997**. FT-Raman spectroscopy of wood: identifying contributions of lignin and carbohydrate polymers in the spectrum of black spruce *(Picea mariana)*. *Applied Spectroscopy.* **51**: 1648-1655. doi:10.1366/0003702971939316

Agarwal UP. 2006. Raman imaging to investigate ultrastructure and composition of plant cell walls: Distribution of lignin and cellulose in black spruce wood (*Picea mariana*). *Planta.* **224**: 1141–1153. doi:10.1007/s00425-006-0295-z

Agarwal UP. 2019. Analysis of Cellulose and Lignocellulose Materials by Raman Spectroscopy: A Review of the Current Status. *Molecules*. **24**(9): 1659. doi:10.3390/molecules24091659

Agarwal UP. 2022. Beyond crystallinity: using Raman spectroscopic methods to further define aggregated/supramolecular structure of cellulose. *Frontiers in Energy Research.* **10**: 857621. doi:10.3389/fenrg.2022.857621

Airoldi CA, Lugo CA, Wightman R, Glover BJ, Robinson S. 2021. Mechanical buckling can pattern the light-diffracting cuticle of *Hibiscus trionum*. *Cell Reports*. **36**(11): 1-14. doi:10.1016/j.celrep.2021.109715

Airoldi CA, Chen C, Herrera-Ubaldo H, Fu H. Lugo CA, Crosby AJ, Glover BJ. 2024. Characterisation of cuticle mechanical properties: analysing stiffness in layered living systems to understand surface buckling patterns. *BioRxiv*. doi:10.1101/2024.03.27.587033

Allen H, Wei D, Gu Y, Li S. 2021. A historical perspective on the regulation of cellulose biosynthesis. *Carbohydrate Polymers.* **252**: 117022. doi: 10.1016/j.carbpol.2020.117022

Armezzani A, Abad U, Ali O, Andres Robin A, Vachez L, Larrieu A, et al. 2018. Transcriptional induction of cell wall remodelling genes is coupled to microtubule-driven growth isotropy at the shoot apex in Arabidopsis. *Development*. **145**(11). doi:10.1242/dev.162255

Barbier de Reuille P. et al. 2015. MorphoGraphX: a platform for quantifying morphogenesis in 4D. *eLife*. **4**: 1-20. doi:10.7554/eLife.05864

Baskin TI. **2001**. On the alignment of cellulose microfibrils by cortical microtubules: a review and a model. *Protoplasma.* **215**: 150-170. doi:10.1007/BF01280311

Bauer WD, Talmadge KW, Keegstra K, Albersheim P. **1973**. The structure of plant cell walls II. The hemicellulose of the walls of suspension-cultured sycamore cells'. *Plant Physiology.* **1**: 174-187. doi:10.1104/pp.51.1.174

Benítez JJ, Guzmán-Puyol S, Vilaplana F, Heredia-Guerrero JA, Domínguez E, Heredia A. 2021. Mechanical Performances of Isolated Cuticles Along Tomato Fruit Growth and Ripening. *Frontiers in Plant Science*. **12**. doi:10.3389/fpls.2021.787839

Berglund J, Mikkelsen D, Flanagan BM, et al. 2020. Wood hemicelluloses exert distinct biomechanical contributions to cellulose fibrillar networks. *Nature Communications.* **11**: 4692 doi:10.1038/s41467-020-18390-z

Bernal-Gallardo JJ, González-Aguilera KL, de Folter S. 2024. *EXPANSIN15* is involved in flower and fruit development in Arabidopsis. *Plant Reproduction.* **37**: 259–270. doi:10.1007/s00497-023-00493-4

Bethke G, Grundman RE, Sreekanta S, Truman W, Katagiri F, Glazebrook J. **2014**. Arabidopsis PECTIN METHYLESTERASEs contribute to immunity against *Pseudomonas syringae*. *Plant Physiology.* **164**: 1093–1107. doi:10.1104/pp.113.227637

Bichara LC, Alvarez PE, Fiori Bimbi MV, Vaca H, Gervasi C, Brandán SA. **2016**. Structural and spectroscopic study of a pectin isolated from citrus peel by using FTIR and FT-Raman spectra and DFT calculations. *Infrared Physics and Technology.* **76**: 315–327. doi:10.1016/j.infrared.2016.03.009

Bock P, Felhofer M, Mayer K, Gierlinger N. **2021**. A guide to elucidate the hidden multicomponent layered structure of plant cuticles by Raman imaging. *Frontiers in Plant Science.* **12**. doi:10.3389/fpls.2021.793330

Bonaventure G, Beisson F, Ohlrogge J, Pollard M. **2004**. Analysis of the aliphatic monomer composition of polyesters associated with Arabidopsis epidermis: Occurrence of octadeca-cis-6, cis-9-diene-1,18-dioate as the major component. *Plant Journal.* **40**: 920–930. doi:10.1111/j.1365-313X.2004.02258.x

Borowska-Wykręt D, Dulski M. 2019. Raman Spectroscopy in Nonwoody Plants. In: Plant Cell Morphogenesis. Methods in Molecular Biology, Humana, New York, NY. **1992**(6): 83-107. doi:10.1007/978-1-4939-9469-4_6

Boudaoud A, Burian A, Borowska-Wykręt D. et al. 2014. FibrilTool, an ImageJ plug-in to quantify fibrillar structures in raw microscopy images. *Nature Protocols.* **9**: 457–463. doi:10.1038/nprot.2014.024

Bowie BT, Chase DB, Griffiths PR. 2000A. Factors affecting the performance of bench-top Raman spectrometers. Part I: instrumental effects. *Applied Spectroscopy*. **54**(5): 164a–73a. doi**:**10.1366/0003702001949924

Bowie BT, Chase DB, Griffiths PR. 2000B. Factors affecting the performance of bench-top Raman spectrometers. Part II: effect of sample. *Applied Spectroscopy*. **54**(6): 200a–7a. doi:10.1366/0003702001950175

Braybrook SA, Peaucelle A. 2013. Mechano-Chemical Aspects of Organ Formation in Arabidopsis thaliana: The Relationship between Auxin and Pectin. *PLOS One.* **8**(3): e57813. doi:10.1371/journal.pone.0057813

Bringmann M, Li E, Sampathkumar A, Kocabek T, Hauser MT, Perssona S. **2012**. POM-POM2/CELLULOSE SYNTHASE INTERACTING1 is essential for the functional association of cellulose synthase and microtubules in Arabidopsis. *The Plant Cell.* **24**: 163–177. doi:10.1105/tpc.111.093575

Brodersen P, Sakvarelidze-Achard L, Bruun-Rasmussen M, et al. 2008. Widespread translational inhibition by plant miRNAs and siRNAs. *Science.* **320**: 1185–1190. doi:10.1126/science.1159151

Burda I, Brauns F, Clark FK, Li CB, Roeder AHK. 2024. Robust organ size in Arabidopsis is primarily governed by cell growth rather than cell division patterns. Development. **151**(19). doi:10.1242/dev.202531

Buschhaus C, Jetter R. 2011. Composition differences between epicuticular and intracuticular wax substructures: How do plants seal their epidermal surfaces? *Journal of Experimental Botany.* **62**: 841–853. doi: 10.1093/jxb/erq366

Caffall KH, Mohnen D. 2009. The structure, function, and biosynthesis of plant cell wall pectic polysaccharides. *Carbohydrate Research*. **344**(14): 1879-900. doi: 10.1016/j.carres.2009.05.021

Carpita NC, Gibeaut DM. **1993**. Structural models of primary cell walls in flowering plants: consistency of molecular structure with the physical properties of the walls during growth. *The Plant Journal.* **3**: 1-30. doi:10.1111/j.1365-313X.1993.tb00007.x

Chen S, Burda I, Jani P, Bex P, Silberstein MN, Roeder AHK. 2025. Fibrous network nature of plant cell walls enables tunable mechanics for development. *Nature Communications.* **16**: 755. doi:10.1038/s41467-025-62844-1

Cheng G, Huang H, Zhou L, He S, Zhang Y, Cheng XA. 2019. Chemical composition and water permeability of the cuticular wax barrier in rose leaf and petal: A comparative investigation. *Plant Physiology and Biochemistry*. **135**: 404-410. doi:10.1016/j.plaphy.2019.01.006

Cho H, Cosgrove DJ. 2000. Altered expression of expansin modulates leaf growth and pedicel abscission in *Arabidopsis thaliana*. *The Proceedings of the National Academy of Sciences.* **97**(17): 9783-9788, doi:10.1073/pnas.160276997

Chylińska M, Szymańska-Chargot M, Zdunek A. **2014**. Imaging of polysaccharides in the tomato cell wall with Raman microspectroscopy. *Plant Methods.* **10**: 14 doi:10.1186/1746-4811-10-14

Cosgrove DJ, Jarvis MC. 2012. Comparative structure and biomechanics of plant primary and secondary cell walls. *Frontiers in Plant Science*. **22**: 204. doi:10.3389/fpls.2012.00204

Cosgrove DJ. 1993. How do plant cell walls extend? *Plant Physiology.* **102**(1): 1-6. doi:10.1104/pp.102.1.1

Cosgrove DJ. 2005. Growth of the plant cell wall. *Nature Reviews Molecular Cell Biology*. **6**(11): 850–861. doi:10.1038/nrm1746

Cosgrove DJ. 2015. Plant expansins: diversity and interactions with plant cell walls. *Current Opinion in Plant Biology*. **25**: 162–172. doi:10.1016/j.pbi.2015.05.014

Cosgrove DJ. 2016. Catalysts of plant cell wall loosening. *F1000Research*. **5**: 2045. doi:10.12688/f1000research.8733.1

Cosgrove DJ. 2018. Diffuse growth of plant cell walls. *Plant Physiology*. **176**: 16-27. doi:10.1104/pp.17.01541

Cosgrove DJ. **2022**. Building an extensible cell wall. *Plant Physiology.* **189**: 1246–1277. doi:10.1093/plphys/kiac184

Cosgrove DJ. 2024A. Structure and growth of plant cell walls. *Nature Reviews Molecular Cell Biology.* **25**: 340–358 doi:10.1038/s41580-023-00691-y

Cosgrove DJ. 2024B. Plant Cell Wall Loosening by Expansins. *Annual Review of Cell and Developmental Biology.* **40**(1): 329-352. doi:10.1146/annurev-cellbio-111822-115334.

Delgado-Cerezo M, Sánchez-Rodríguez C, Escudero V, et al. 2012. Arabidopsis heterotrimeric G-protein regulates cell wall defence and resistance to necrotrophic fungi. *Molecular Plant.* **5**: 98–114. doi:10.1093/mp/ssr082

Derbyshire P, Findlay K, McCann MC, Roberts K. 2007. Cell elongation in Arabidopsis hypocotyls involves dynamic changes in cell wall thickness. *Journal of Experimental Botany.* **58**: 2079–2089. doi:10.1093/jxb/erm074

Domínguez E, Heredia-Guerrero JA, Heredia A. 2017. The plant cuticle: old challenges, new perspectives. *Journal of Experimental Botany*. **68**(19): 5251-5255. doi:10.1093/jxb/erx389

Donaldson L. 2020. Autofluorescence in Plants. *Molecules*, **25**(10): 2393. doi:10.3390/molecules25102393

Dumais J. 2013. Modes of deformation of walled cells. *Journal of Experimental Botany*. **64**(15): 4681-95. doi: 10.1093/jxb/ert268

Echevin E, Le Gloanec C, Skowrońska N, Routier-Kierzkowska AL, Burian A, Kierzkowski D. 2019. Growth and biomechanics of shoot organs. *Journal of Experimental Botany.* **70**(14): 3573-3585. doi:10.1093/jxb/erz205

Elsner J, Kwiatkowska D, Borowska-Wykręt D. 2025. Three levels of heterogeneity – growth of Arabidopsis leaf epidermis. *BMC Plant Biology* **25**(291). doi:10.1186/s12870-025-06259-6

Faix O. 1991. Classification of lignins from different botanical origins by FT-IR spectroscopy. *Holzforschung. International Journal of the Biology, Chemistry, Physics and Technology of Wood* **45**: 21–28. doi:10.1515/hfsg.1991.45.s1.21

Faria-Blanc N, Mortimer JC, Dupree P. **2018**. A transcriptomic analysis of Xylan mutants does not support the existence of a secondary cell wall integrity system in Arabidopsis. *Frontiers in Plant Science.* **9**: 384. doi:10.3389/fpls.2018.00384

Felhofer M, Mayr K, Lütz-Meindl U, Gierlinger N. **2021**. Raman imaging of Micrasterias: new insights into shape formation. *Protoplasma.* **258**: 1323–1334. doi:10.1007/s00709-021-01685-3

Felten J, Hall H, Jaumot J, Tauler R, De Juan A, Gorzsás A. **2015**. Vibrational spectroscopic image analysis of biological material using multivariate curve resolution-alternating least squares (MCR-ALS). *Nature Protocols.* **10**: 217–240. doi:10.1038/nprot.2015.008

Fernández V, Bahamonde HA, Peguero-Pina JJ, et al. 2017. Physico-chemical properties of plant cuticles and their functional and ecological significance. *Journal of Experimental Botany.* **68**: 5293–5306. doi:10.1093/jxb/erx302

Festucci-Buselli RA, Otoni WC, Joshi CP. **2007**. Structure, organization, and functions of cellulose synthase complexes in higher plants. *Brazilian Journal of Plant Physiology.* **19**: 1–19. doi:10.1590/S1677-04202007000100001

Fry SC, Smith RC, Renwick KF, Martin DJ, Hodge SK, Matthews KJ. 1992. Xyloglucan endotransglycosylase, a new wall-loosening enzyme activity from plants. *Biochemical Journal* **282**: 821–828. doi:10.1042/BJ2820821

Fry SC, York WS, Albersheim P. et al. 1993. An unambiguous nomenclature for xyloglucan-derived oligosaccharides. *Physiologia Plantarum.* **89**: 1-3. doi:10.1111/j.1399-3054.1993.tb01778.x

Gierlinger N, Schwanninger M. **2006**. Chemical imaging of poplar wood cell walls by confocal Raman microscopy. *Plant Physiology.* **140**: 1246–1254. doi:10.1104/pp.105.066993

Gierlinger N, Schwanninger M. **2007**. The potential of Raman microscopy and Raman imaging in plant research. *Journal of Spectroscopy* **21**: 69-89. doi:10.1155/2007/498206

Gierlinger N, Sapei L, Paris O. **2008**. Insights into the chemical composition of Equisetum hyemale by high resolution Raman imaging. *Planta.* **227**: 969–980. doi:10.1007/s00425-007-0671-3

Gierlinger N, Luss S, König C, Konnerth J, Eder M, Fratzl P. **2010**. Cellulose microfibril orientation of Picea abies and its variability at the micron-level determined by Raman imaging. *Journal of Experimental Botany.* **61**: 587–595. doi:10.1093/jxb/erp325

Gierlinger N, Keplinger T, Harrington M. **2012**. Imaging of plant cell walls by confocal Raman microscopy. *Nature Protocols.* **7**: 1694–1708. doi:10.1038/nprot.2012.092

Gigli-Bisceglia N, Engelsdorf T, Hamann T. **2020**. Plant cell wall integrity maintenance in model plants and crop species-relevant cell wall components and underlying guiding principles. *Cellular and Molecular Life Sciences.* **77**: 2049–2077. doi:10.1007/s00018-019-03388-8

González Moreno A, Domínguez E, Mayer K, et al. 2022. 3D (x-y-t) Raman imaging of tomato fruit cuticle: Microchemistry during development. *Plant Physiology.* **191**: 219-232. doi:10.1093/plphys/kiac369

Green PB. 1962. Mechanism for Plant Cellular Morphogenesis. *Science*. **138**(3548): 1404-5. doi:10.1126/science.138.3548.1404

Günl M, Pauly M. **2011**. AXY3 encodes a α-xylosidase that impacts the structure and accessibility of the hemicellulose xyloglucan in Arabidopsis plant cell walls. *Planta.* **233**: 707–719. doi:10.1007/s00425-010-1330-7

Haas KT. 2020. Pectin homogalacturonan nanofilament expansion drives morphogenesis in plant epidermal cells. *Science* **367**: 1003-1007. doi:10.1126/science.aaz5103

Hager A. 2003. Role of the plasma membrane H+ -ATPase in auxin-induced elongation growth: historical and new aspects. *Journal of Plant Research*. **116**: 483–505. doi:10.1007/s10265-003-0110-x

Hejnowicz Z, Sievers A. 1997. Tissue stresses in plant organs: Their origin and importance for movements. In: Alt W, Deutsch A, & Dunn GA (eds.). *Dynamics of Cell and Tissue Motion.* Mathematics and Biosciences in Interaction. Birkhäuser, Basel. 319–328. doi:10.1007/978-3-0348-8916-2_28

Hejnowicz Z. 2002. Anatomia i histogeneza roślin naczyniowych. Organy wegetatywne. Warszawa: Wydawnictwo Naukowe PWN. 29-30, 267

Hejnowicz Z. 2011. Plants as Mechano-Osmotic Transducers. In: Wojtaszek P. (ed) Mechanical Integration of Plant Cells and Plants. Signaling and Communication in Plants, vol 9. Springer, Berlin, Heidelberg. Doi:10.1007/978-3-642-19091-9_10

Hejnowicz Z. 2012. Anatomia i histogeneza roślin naczyniowych. Organy wegetatywne. PWN Warszawa. 212-213, 220-223

Heredia-Guerrero JA, San-Miguel MA. Sansom MS. Heredia A. Benitez JJ. **2009.** Chemical reactions in 2D: Self-assembly and self-esterification of 9(10),16-dihydroxypalmitic acid on mica surface. *Langmuir*. **25**: 6869–6874. doi:10.1021/la9001412

Heredia-Guerrero JA, Benítez JJ, Domínguez E, et al. 2014. Infrared and Raman spectroscopic features of plant cuticles: A review. *Frontiers in Plant Science.* **5**: 305. doi:10.3389/fpls.2014.00305

Hervieux N, Dumond M, Sapala A, Routier-Kierzkowska AL, Kierzkowski D, Roeder AH, Smith RS, Boudaoud A, Hamant O. 2016. A Mechanical Feedback Restricts Sepal Growth and Shape in Arabidopsis. *Current Biology*. **26**: 1019-1028. doi: 10.1016/j.cub.2016.03.004

Hong L, Dumond M, Tsugawa S, Sapala A, Routier-Kierzkowska AL, Zhou Y, Chen C, Kiss A, Zhu M, Hamant O. et al. 2016. Variable cell growth yields reproducible organ development through spatiotemporal averaging. *Developmental Cell.* **38**: 15-32. doi:10.1016/j.devcel.2016.06.016

Hong L, Brown J, Segerson NA, Rose JKC, Roeder AHK. **2017**. CUTIN SYNTHASE 2 maintains progressively developing cuticular ridges in Arabidopsis sepals. *Molecular Plant.* **10**: 560–574. doi:10.1016/j.molp.2017.01.002

Hong L, Dumond M, Zhu M, Tsugawa S, Li CB, Boudaoud A, Hamant O, Roeder AHK. 2018. Heterogeneity and Robustness in Plant Morphogenesis: From Cells to Organs. *Annual Review of Plant Biology* . **69**: 469-495. doi:10.1146/annurev-arplant-042817-040517

Hongo S, Sato K, Yokoyama R, Nishitani K. **2012**. Demethylesterification of the primary wall by PECTIN METHYLESTERASE35 provides mechanical support to the Arabidopsis stem. *The Plant Cell.* **24**: 2624–2634. doi:10.1105/tpc.112.099325

Huang X, Hai Y, Xie WH. 2017. Anisotropic cell growth-regulated surface micropatterns in flower petals. *Theoretical and Applied Mechanics Letters.* **7**(3): 169-174 doi:10.1016/j.taml.2017.03.004

Jarvis MC. 2018. Structure of native cellulose microfibrils, the starting point for nanocellulose manufacture. *Philosophical Transactions of the Royal Society A: Mathematical, Physical and Engineering Sciences*. **376**. doi.org/10.1098/rsta.2017.0045

Jonsson K, Lathe RS, Kierzkowski D, Routier-Kierzkowska AL, Hamant O, Bhalerao RP. 2021. Mechanochemical feedback mediates tissue bending required for seedling emergence. *Current Biology.* **22**(6): 1154-1164. doi: 10.1016/j.cub.2020.12.016

Jenks MA, Eigenbrode SD, Lemieux B. 2002. Cuticular waxes of Arabidopsis. *The Arabidopsis Book.* E0016. doi: 10.1199/tab.0016

Juárez ID, Kurouski D. 2024. Contemporary applications of vibrational spectroscopy in plant stresses and phenotyping. *Frontiers in Plant Science.* **15**. doi:10.3389/fpls.2024.1411859

Juraniec M, Gajda B. **2020**. Cellulose biosynthesis in plants – The concerted action of CESA and non-CESA proteins. *Biologia Plantarum.* **64**: 363–377. doi:10.32615/bp.2020.065

Kacurakova M, Wellner N, Ebringerovaâ A, Hromaâ Dkovaâ Z, Wilson RH, Belton PS. **1999**. Characterisation of xylan-type polysaccharides and associated cell wall components by FT-IR and FT-Raman spectroscopies. *Food hydrocolloids.* **13**: 35-41. doi:10.1016/S0268-005X(98)00067-8

Kaczmarska A, Pieczywek PM, Cybulska J, Zdunek A. 2022. Structure and functionality of Rhamnogalacturonan I in the cell wall and in solution: A review. *Carbohydrate Polymers*. **278** : 118909. doi:10.1016/j.carbpol.2021.118909

Keegstra K., Talmadge KW. Bauer WD. Albersheim P. 1973. The structure of plant cell walls: III. A model of the walls of suspension-cultured sycamore cells based on the interconnections of the macromolecular components. *Plant Physiology*. **51**: 188–197. doi:10.1104/pp.51.1.188

Kerstens S, Decraemer WF, Verbelen JP. 2001. Cell Walls at the Plant Surface Behave Mechanically Like Fiber-Reinforced Composite Materials. *Plant Physiology*. **127**(2): 381–385. doi:10.1104/pp.010423

Kierzkowski D. et al. 2012. Elastic Domains Regulate Growth and Organogenesis in the Plant Shoot Apical Meristem. *Science.* **335**: 1096-1099. doi:10.1126/science.1213100

Koch K, Ensikat HJ. 2008. The hydrophobic coatings of plant surfaces: Epicuticular wax crystals and their morphologies, crystallinity and molecular self-assembly. *Micron*. **39**: 759–772. doi:10.1016/j.micron.2007.11.010

Komis G, Luptovčiak I, Ovečka M, Samakovli D, Šamajová O, Šamaj J. **2017**. Katanin effects on dynamics of cortical microtubules and mitotic arrays in Arabidopsis thaliana revealed by advanced live-cell imaging. *Frontiers in Plant Science.* **8**: 866. doi:10.3389/fpls.2017.00866

Kourounioti RLA, Band LR, Fozard JA, et al. 2013. Buckling as an origin of ordered cuticular patterns in flower petals. *Journal of the Royal Society Interface.* **80***:* 20120847. doi:10.1098/rsif.2012.0847

Kunst L, Samuels AL. 2003. Biosynthesis and secretion of plant cuticular wax. *Progress in Lipid Research*. **42**(1): 51-80. doi: 10.1016/s0163-7827(02)00045-0

Kunst L, Samuels L. 2009. Plant cuticles shine: advances in wax biosynthesis and export. *Current Opinion in Plant Biology*. **12**(6): 721-7. doi: 10.1016/j.pbi.2009.09.009

Le Gloanec C, Collet L, Silveira SR, Wang B, Routier-Kierzkowska AL, Kierzkowski D. 2022. Cell type-specific dynamics underlie cellular growth variability in plants. *Development.* **149**(14). doi: 10.1242/dev.200783

Lee SJ, Saravanan RS, Damasceno CMB, Yamane H, Kim BD, Rose JKC. **2004**. Digging deeper into the plant cell wall proteome. *Plant Physiology and Biochemistry.* **42**: 979–988. doi:10.1016/j.plaphy.2004.10.014

Li S, Bashline L, Lei L, Gu Y. 2014. Cellulose synthesis and its regulation. *The Arabidopsis Book / American Society of Plant Biologists*. **12.** e0169. doi:10.1199/tab.0169

Lipowczan M, Borowska-Wykręt D, Natonik-Białoń S, Kwiatkowska D. 2018. Growing cell walls show a gradient of elastic strain across their layers. *Journal of Experimental Botany.* **69**(18): 4349–4362. doi:10.1093/jxb/ery237

Lugo CA, Airoldi C, Chen C, Crosby AJ, Glover BJ. 2023. Morphoelastic modelling of pattern development in the petal epidermal cell cuticle. *Journal of the Royal Society Interface.* **20**. doi:10.1098/rsif.2023.0001

Lund CH, Stenbaek A, Atmodjo MA, Rasmussen RE, Moller IE, Erstad SM, Biswal AK, Mohnen D, Mravec J, Sakuragi Y. 2020. Pectin Synthesis and Pollen Tube Growth in Arabidopsis Involves Three GAUT1 Golgi-Anchoring Proteins: GAUT5, GAUT6, and GAUT7. *Frontiers in Plant Science.* **11**. doi:10.3389/fpls.2020.585774

Luptovčiak I, Komis G, Takáč T, Ovečka M, Šamaj J. **2017**. Katanin: A sword cutting microtubules for cellular, developmental, and physiological purposes. *Frontiers in Plant Science* **8**: 1982. doi: 10.3389/fpls.2017.01982

Makarem M, Lee CM, Kafle K, et al. 2019. Probing cellulose structures with vibrational spectroscopy. *Cellulose.* **26**: 35–79. doi:10.1007/s10570-018-2199-z

Marchessault RH, Sundararajan PR. **1983**. Cellulose. *The Polysaccharides,* **2**: 11-95. doi:10.1016/B978-0-12-065602-8.50007-8

Martens P. 1933. Recherches sur la cuticule. *Protoplasma*. **20**: 483–515. doi:10.1007/BF02674844.

Mateu BP, Hauser MT, Heredia A, Gierlinger N. **2016**. Waterproofing in Arabidopsis: Following phenolics and lipids in situ by Confocal Raman Microscopy. *Frontiers in Chemistry.* **4**: 10. doi:10.3389/fchem.2016.00010

Mazurek S, Mucciolo A, Humbel BM, Nawrath C. 2013. Transmission Fourier transform infrared microspectroscopy allows simultaneous assessment of cutin and cell-wall polysaccharides of Arabidopsis petals. *The Plant Journal*. **74**: 880-891. doi:10.1111/tpj.12164

Mazurek S, Garroum I, Daraspe J, et al. 2017. Connecting the molecular structure of cutin to ultrastructure and physical properties of the cuticle in petals of Arabidopsis. *Plant Physiology.* **173**: 1146–1163. doi:10.1104/pp.16.01637

Mazurek, S. Mucciolo, A. Humbel, B.M. Nawrath, C. 2013. Transmission Fourier transform infrared microspectroscopy allows simultaneous assessment of cutin and cell-wall polysaccharides of Arabidopsis petals. *The Plant Journal*. **74**: 880–891. doi:10.1111/tpj.12164

McQueen-Mason S, Durachko DM, Cosgrove DJ. 1992. Two endogenous proteins that induce cell wall extension in plants. *The Plant Cell*. **11**: 1425-33. doi:10.1105/tpc.4.11.1425

Meyer HM, Roeder AHK.2014. Stochasticity in plant cellular growth and patterning. *Frontiers in Plant Science*. **5**. doi:10.3389/fpls.2014.00420

Miller SJ. 2006. The method of least squares. *Mathematics Department Brown University*.
https://web.williams.edu/Mathematics/sjmiller/public_html/BrownClasses/54/handouts/MethodLeastSquares.pdf

Mollier C, Skrzydel J, Borowska-Wykret D, et al. 2023. Spatial consistency of cell growth direction during organ morphogenesis requires CELLULOSE SYNTHASE INTERACTIVE1. *Cell Reports.* **112689**: 1–21. doi:10.1016/j.celrep.2023.112689

Morel O, Gierlinger N. 2023. Chemical tissue heterogeneity of young Arabidopsis stems revealed by Raman imaging combined with multivariate data analysis. *Microchemical Journal*. **191**. doi:10.1016/j.microc.2023.108900

Mouille G, Ralet MC, Cavelier C, et al. 2007. Homogalacturonan synthesis in Arabidopsis thaliana requires a Golgi-localized protein with a putative methyltransferase domain. *The Plant Journal.* **50**: 605–614. doi:10.1111/j.1365-313X.2007.03086.x

Moyroud E, Airoldi CA, Ferria J, Giorio C, Steimer SS, Rudall PJ, Prychid CJ, Halliwell S, Walker JF, Robinson S, Kalberer M, Glover BJ. 2022. Cuticle chemistry drives the development of diffraction gratings on the surface of *Hibiscus trionum* petals. *Current Biology*. **32**(24): 5323-5334. doi:10.1016/j.cub.2022.10.065

Natonik-Białoń S, Borowska-Wykręt D, Mosca G, Grelowski M, Wrzalik R, Smith RS, Kwiatkowska D. 2019. Deformation of a cell monolayer due to osmotic treatment: a case study of onion scale epidermis. *Botany*. **98**(1): 21-36. doi:10.1139/cjb-2019-0027

Nawrath C, Schreiber L, Franke RB, Geldner N, Reina-Pinto JJ, Kunst L. 2013. Apoplastic Diffusion barriers in Arabidopsis. *The Arabidopsis Book.* **11**: e0167. doi:10.119/tab.0167

Nicolas W, Fäßler F, Dutka P, Schur F, Jensen G, Meyerowitz E. 2022. Cryo-electron tomography of the onion cell wall shows bimodally oriented cellulose fibers and reticulated homogalacturonan networks. *Current Biology*. **32**(11): 2375-2389. doi:10.1016/j.cub.2022.04.024

Obomighie I, Prentice IJ, Lewin-Jones P, Bachtiger F, Ramsay N, Kishi-Itakura C, Goldberg MW, Hawkins TJ, Sprittles JE, Knight H, Sosso GC. 2025. Understanding pectin cross-linking in plant cell walls. *Communications Biology* **8**: 72. doi:10.1038/s42003-025-07495-0

Ochoa-Villarreal M, Aispuro-Hernández E, Vargas-Arispuro I, Martínez-Téllez MA. 2012. Function, Structure and Biological Activity of Their Derivatives. *Plant Cell Wall Polymers.* doi:10.5772/46094

Panikashvili D, Shi JX, Schreiber L., Aharoni A. 2009. The Arabidopsis *DCR* Encoding a Soluble BAHD Acyltransferase Is Required for Cutin Polyester Formation and Seed Hydration Properties. *Plant Physiology*. **151**: 1773-1789. doi:10.1104/pp.109.143388

Park YB, Cosgrove DJ. 2012. Changes in Cell Wall Biomechanical Properties in the Xyloglucan-Deficient *xxt1/xxt2* Mutant of Arabidopsis. *Plant Physiology*. **158**(1): 465–475. doi:10.1104/pp.111.189779

Park YB, Cosgrove DJ. 2015. Xyloglucan and its interactions with other components of the growing cell wall. *Plant Cell Physiology*. **56**: 180-94. doi:10.1093/pcp/pcu204.

Peaucelle A, Braybrook SA, Le Guillou L, Bron E, Kuhlemeier C, Hofte H. 2011. Pectin-induced changes in cell wall mechanics underlie organ initiation in Arabidopsis. *Current Biology*. **21**: 1720–1726. doi:10.1016/j.cub.2011.08.057

Peaucelle A, Wightman R, Hofte H. 2015. The control of growth symmetry breaking in the arabidopsis hypocotyl. *Current Biology*. **25**: 1746–1752. doi:10.1016/j.cub.2015.06.032

Pelaz S, Ditta GS, Baumann E, Wisman E, Yanofsky MF. 2000. B and C floral organ identity functions require SEPALLATA MADS-box genes. *Nature*. **405**: 200–203. doi:10.1038/35012103

Pelloux J, Rustérucci C, Mellerowicz EJ. **2007**. New insights into pectin methylesterase structure and function. *Trends in Plant Science.* **12**: 267–277. doi:10.1199/tab.0167

Philippe G, Geneix N, Petit J, Guillon F, Sandt C, Rothan C, Lahaye M, Marion D, Bakan B. 2020. Assembly of tomato fruit cuticles: a cross-talk between the cutin polyester and cell wall polysaccharides. *New Phytologist*. **226**(3): 809-822. doi: 10.1111/nph.16402

Phyo P, Gu Y, Hong M. 2019. Impact of acidic pH on plant cell wall polysaccharide structure and dynamics: insights into the mechanism of acid growth in plants from solid-state NMR. *Cellulose* **26**: 291–304. doi:10.1007/s10570-018-2094-7

Pieczywek PM, Chibrikov V, Zdunek A. 2023. In silico studies of plant primary cell walls - structure and mechanics. *Biological Reviews of the Cambridge Philosophical Society*. **98**(3): 887-899. doi: 10.1111/brv.12935

Piqueras S, Duponchel L, Tauler R, de Juan A. 2011. Resolution and segmentation of hyperspectral biomedical images by Multivariate Curve Resolution-Alternating Least Squares. *Analytica Chimica Acta*. **705**(1–2): 182-192. doi:10.1016/j.aca.2011.05.020

Piqueras S, Füchtner S, Rocha de Oliveira R, Gómez-Sánchez A, Jelavić S, Keplinger T, de Juan A, Thygesen Lisbeth G, 2020. Understanding the Formation of Heartwood in Larch Using Synchrotron Infrared Imaging Combined With Multivariate Analysis and Atomic Force Microscope Infrared Spectroscopy. *Frontiers in Plant Science.* **10**. doi:10.3389/fpls.2019.01701

Probine MC, Barber NF. 1966. The Structure and Plastic Properties of the Cell Wall of Nitella in Relation to Extension Growth. *Australian Journal of Biological Sciences.* **19**: 439-458. doi:10.1071/BI9660439

Ralet MC, Cabrera JC, Bonnin E, Quéméner B, Hellìn P, Thibault JF. **2005**. Mapping sugar beet pectin acetylation pattern. *Phytochemistry.* **66**: 1832–1843. doi:10.1016/j.phytochem.2005.06.003

Ramirez FJ, Luque P, Heredia A, Bukovac MJ. **1992**. Fourier Transform IR study of enzymatically isolated tomato fruit cuticular membrane. *Biopolymers: Original Research on Biomolecules.* **32**: 1425-1429. doi:10.1002/bip.360321102

Reynoud N, Petit J, Bres C, Lahaye M, Rothan C, Marion D, Bakan B. 2021. The Complex Architecture of Plant Cuticles and Its Relation to Multiple Biological Functions. *Frontiers in Plant Science*. **12**. doi:10.3389/fpls.2021.782773

Reynoud N, Geneix N, D'Orlando A, Petit J, Mathurin J, Deniset-Besseau A, Marion D, Rothan C, Lahaye M, Bakan B. 2023. Cuticle architecture and mechanical properties: a functional relationship delineated through correlated multimodal imaging. *New Phytologist.* **238**: 2033–2046. doi:10.1111/nph.18862

Richter S, Müssig J, Gierlinger N. 2011. Functional plant cell wall design revealed by the Raman imaging approach. *Planta.* **233**: 763–772. doi:10.1007/s00425-010-1338-z

Riederer M, Müller C. 2006. Biology of the Plant Cuticle. *Annual Plant Reviews.* **23**. Blackwell Publishing Professional. doi:10.1002/9780470988718

Robinson DO, Coate JE, Singh A, Hong L, Bush M, Doyle JJ, Roeder AHK. 2018. Ploidy and Size at Multiple Scales in the Arabidopsis Sepal. *The Plant Cell.* **30**(10): 2308-2329. doi:10.1105/tpc.18.00344

Roeder AHK, Chickarmane V, Cunha A, Obara B, Manjunath BS, Meyerowitz EM. 2010. Variability in the Control of Cell Division Underlies Sepal Epidermal Patterning in Arabidopsis thaliana. *PLOS Biology*. **8**(5): e1000367. doi:10.1371/journal.pbio.1000367

Roeder AHK. 2021. *Arabidopsis* sepals: A model system for the emergent process of morphogenesis. *Quantitative Plant Biology*. **2**: e14. doi:10.1017/qpb.2021.12

Roelofsen PA. 1958. Cell-wall structure as related to surface growth some supplementary remarks on multinet growth. *Acta Botanica Neerlandica*. **7**: 77-89. doi:10.1111/j.1438-8677.1958.tb00609.x

Rongpipi S, Ye D, Gomez ED, Gomez EW. 2019. Progress and opportunities in the characterization of cellulose–an important regulator of cell wall growth and mechanics. *Frontiers in Plant Science*. doi: 10.3389/fpls.2018.01894

Routier-Kierzkowska AL, Runions A. 2018. Modeling Plant Morphogenesis: An Introduction. *In: Geitmann, A., Gril, J. (eds) Plant Biomechanics*. Springer, Cham. doi:10.1007/978-3-319-79099-2_8

Ruel K, Nishiyama Y, Joseleau JP. 2012. Crystalline and amorphous cellulose in the secondary walls of Arabidopsis. *Plant Science.* **193-194**: 48-61. doi:10.1016/j.plantsci.2012.05.008

Saletnik A, Saletnik B, Puchalski C. 2021. Overview of popular techniques of Raman spectroscopy and their potential in the study of plant tissues. *Molecules.* **26**: 1537. doi:10.3390/molecules26061537

Samalova M, et al. 2024. Hormone-regulated expansins: Expression, localization, and cell wall biomechanics in Arabidopsis root growth. *Plant Physiology*. **194**: 209–228. doi:10.1093/plphys/kiad228

Sampedro J, Pardo B, Gianzo C, Guitián E, Revilla G, Zarra I. **2010**. Lack of α-xylosidase activity in arabidopsis alters xyloglucan composition and results in growth defects. *Plant Physiology.* **154**: 1105–1115. doi:10.1104/pp.110.163212

Samuels L, Kunst L, Jetter R. 2008. Sealing plant surfaces: cuticular wax formation by epidermal cells. *Annual Review of Plant Biology*. **59**: 683-707. doi: 10.1146/annurev.arplant.59.103006.093219

Sapala A, Smith RS. 2020. Osmotic treatment for quantifying cell wall elasticity in the sepal of Arabidopsis thaliana. *Methods in Molecular Biology* **2094**: 101–112. doi:10.1007/978-1-0716-0183-9_11

Sasani N, Bock P, Felhofer M, Gierlinger N. **2021**. Raman imaging reveals in-situ microchemistry of cuticle and epidermis of spruce needles. *Plant Methods.* **17**: 1-15. doi:10.1186/s13007-021-00717-6

Schmidt M, Schwartzberg AM, Perera PN, et al. 2009. Label-free in situ imaging of lignification in the cell wall of low lignin transgenic Populus trichocarpa. *Planta.* **230**: 589–597. doi:10.1007/s00425-009-0963-x

Sechet J, Frey A, Effroy-Cuzzi D, et al. 2016. Xyloglucan metabolism differentially impacts the cell wall characteristics of the endosperm and embryo during Arabidopsis seed germination. *Plant Physiology* **170**: 1367–1380. doi:10.1104/pp.15.01312

Segado P, Heredia-Guerrero JA, Heredia A,, Domínguez E. 2020. Cutinsomes and CUTIN SYNTHASE1 Function Sequentially in Tomato Fruit Cutin Deposition. *Plant Physiology*. **183**(4): 1622–1637. doi:10.1104/pp.20.00516

Séné CFB, Mccann MC, Wilson RH, Crinter R. **1994**. Fourier-Transform Raman and Fourier-Transform lnfrared Spectroscopy ' An lnvestigation of Five Higher Plant Cell Walls and Their Components. *Plant Physiology.* **170**: 1367-1380. doi:10.1104/pp.15.01312

Shi JX, Malitsky S,De Oliveira S, Branigan C, Franke RB, Schreiber L, Aharoni A. 2011. SHINE Transcription Factors Act Redundantly to Pattern the Archetypal Surface of Arabidopsis Flower Organs. *PLOS Genetics.* **7**(5): e1001388. doi:10.1371/journal.pgen.1001388

Showalter AM. 2001. Arabinogalactan-proteins: structure, expression and function. *Cellular and Molecular Life Sciences.* **58**(10): 1399-417. doi:10.1007/PL00000784

Skrzydeł J, Borowska-wykręt D, Kwiatkowska D. **2021**. Structure, assembly and function of cuticle from mechanical perspective with special focus on perianth. *International Journal of Molecular Sciences* **22**: 4160. doi:10.3390/ijms22084160

Smyth DR, Bowman JL, Meyerowitz EM. 1990. Early flower development in Arabidopsis. *The Plant Cell*. **2**(8): 755-67. doi:10.1105/tpc.2.8.755

Smyth D.R. 2017. Wrinkles on Sepals: Cuticular Ridges Form when Cuticle Production Outpaces Epidermal Cell Expansion. *Molecular Plant.* **10**: 540–541. doi:10.1016/j.molp.2017.02.008

Stępiński D, Kwiatkowska M, Wojtczak A, Polit JT, Domínguez E, Heredia A, Popłońska K. 2020. The Role of Cutinsomes in Plant Cuticle Formation. *Cells*. **9**(8): 1778. doi:10.3390/cells9081778

Stephens RM. **1984**. Application of Infrared Raman and Resonance Raman Spectroscopy in biochemistry. *Biochemical Society Transactions.* **12**: 1155–1156. doi:10.1042/bst0121155

Stępiński D. Kwiatkowska M. Wojtczak A. Polit JT. Domínguez E. Heredia A. Popłońska K. 2020. The Role of Cutinsomes in Plant Cuticle Formation. *Cells*. **9**(8): 1778. doi:10.3390/cells9081778

Sterling JD, Quigley HF, Orellana A, Mohnen D. **2001**. The catalytic site of the pectin biosynthetic enzyme-1,4-galacturonosyltransferase is located in the lumen of the Golgi. *Plant Physiology.* **127**: 360-371. doi:10.1104/pp.127.1.360

Stratilová B, Šesták S, Mravec J, et al. 2020. Another building block in the plant cell wall: Barley xyloglucan xyloglucosyl transferases link covalently xyloglucan and anionic oligosaccharides derived from pectin. *The Plant Journal.* **104**: 752–767. doi:10.1111/tpj.14964

Strauss S. et al. 2022. Using positional information to provide context for biological image analysis with MorphoGraphX 2.0 *eLife.* **11**: e72601. doi:10.7554/eLife.72601

Synytsya A, Čopíková J, Matějka P, Machovič V. **2003**. Fourier transform Raman and infrared spectroscopy of pectins. *Carbohydrate Polymers.* **54**: 97–106. doi:10.1016/S0144-8617(03)00158-9

Szymańska-Chargot M, Cybulska J, Zdunek A. 2011. Sensing the structural differences in cellulose from apple and bacterial cell wall materials by Raman and FT-IR Spectroscopy. *Sensors*. **11**: 5543-5560. doi:10.3390/s110605543

Talbott LD, Ray PM. 1992. Molecular size and separability features of pea cell wall polysaccharides: implications for models of primary wall structure. *Plant Physiology.* **98**: 357–368. doi:10.1104/pp.98.1.357

Tauriello G, Meyer HM, Smith RS, Koumoutsakos P, Roeder AHK. 2015. Variability and Constancy in Cellular Growth of Arabidopsis Sepals. *Plant Physiology*. **169**(4): 2342–2358. doi:10.1104/pp.15.00839

Tiloca G, Neuner G, Jetter R, Gierlinger N. 2025. Raman micro-spectroscopy uncovers complex structural and chemical adaptations of alpine azalea leaf surface. *Microchemical Journal.* **213**: 113690. doi:10.1016/j.microc.2025.113690

Tolleter D, Smith EN, Dupont-Thibert C, Uwizeye C, Vile D, Gloaguen P, Falconet D, Finazzi G, Vandenbrouck Y, Curien G. 2024. The Arabidopsis leaf quantitative atlas: a cellular and subcellular mapping through unified data integration. *Quantitative Plant Biology.* **29**: 5. doi:10.1017/qpb.2024.1

Trinh DC, Melogno I, Martin M, et al. 2024. *Arabidopsis* floral buds are locked through stress-induced sepal tip curving. *Nature Plants.* **10**: 1258–1266 doi:10.1038/s41477-024-01760-6

Tsugawa S, Hervieux N, Kierzkowski D, Routier-Kierzkowska AL, Sapala A, Hamant O, Smith RS, Roeder AHK, Boudaoud A, Li CB. 2017. Clones of cells switch from reduction to enhancement of size variability in *Arabidopsis* sepals. *Development.* **144**(23): 4398-4405. doi: 10.1242/dev.153999

Tsuagawa S, Yamagishi Y, Watanabe U. et al. 2019. Dynamics of structural polysaccharides deposition on the plasma-membrane surface of plant protoplasts during cell wall regeneration. *Journal of Wood Science.* **65**: 47. doi:10.1186/s10086-019-1826-0

Uyttewaal M, Burian A, Alim K, et al. 2012. Mechanical stress acts via katanin to amplify differences in growth rate between adjacent cells in Arabidopsis. *Cell.* **149**: 439-51. doi:10.1016/j.cell.2012.02.048

Verger S, Long Y, Boudaoud A, Hamant O. 2018. A tension-adhesion feedback loop in plant epidermis. *eLife.* **7**: e34460. doi:10.7554/eLife.34460

Vincent JFV. 1992. Mechanical design in organisms. In: J.F.V. Vincent, (ed.), *Biomechanics*. Oxford: Oxford University Press. 57–74

Vogler H, Felekis D, Nelson BJ, Grossniklaus U. 2015. Measuring the mechanical properties of plant cell walls. *Plants.* **4**: 167–182. doi:10.3390/plants4020167

Wang T, Hong M. 2016. Solid-state NMR investigations of cellulose structure and interactions with matrix polysaccharides in plant primary cell walls. *Journal of Experimental Botany*. **67**(2): 503–514. doi:10.1093/jxb/erv416

Whitney HM, Kolle M, Andrew P, Chittka L, Steiner U, Glover BJ. 2009. Floral iridescence, produced by diffractive optics, acts as a cue for animal pollinators. *Science.* **323**: 130–133. doi: 10.1126/science.1166256

Williams MAK. 2020. Pectin gelation and its assembly into functional materials. In: Kontogiorgos V, (ed.) *Pectin: Technological and Physiological Properties*. Springer, Cham. 191–220. doi:10.1007/978-3-030-53421-9_7

Wojtaszek P, Woźny A, Ratajczak L. 2007. Biologia komórki roślinnej. Funkcja. T. 2. wydanie 1. Wydawnictwo Naukowe PWN. 368-378

Wolf S. 2022. Cell Wall Signaling in Plant Development and Defense. *Annual Review of Plant Biology*. **73**: 323-353. doi:10.1146/annurev-arplant-102820-095312

Wormit A, Usadel B. 2018. The Multifaceted Role of Pectin Methylesterase Inhibitors (PMEIs). *International Journal of Molecular Sciences*. **19**(10): 2878. doi:10.3390/ijms19102878

Wuyts N, Palauqui J-C, Conejero G, Verdeil JL, Granier C, Massonnet C. 2010. PLANT METHODS Open Access METHODOLOGY High-contrast three-dimensional imaging of the Arabidopsis leaf enables the analysis of cell dimensions in the epidermis and mesophyll. *Plant Methods.* **6**: 1-14. doi:10.1186/1746-4811-6-17

Xin X, Lei L, Zheng Y, Zhang T, Pingali SV, O'Neill H, Cosgrove DJ, Li S, Gu Y. 2020. Cellulose synthase interactive1- and microtubule-dependent cell wall architecture is required for acid growth in Arabidopsis hypocotyls. *Journal of Experimental Botany*. **71**(10): 2982–2994. doi:10.1093/jxb/eraa063

Xu Z, He Z, Song Y, et al. 2018. Topic review: Application of Raman spectroscopy characterization in micro/nano-machining. *Micromachines.* **9**: 361. doi:10.3390/mi9070361

Yadav AS, Roeder AHK. 2024. An optimized live imaging and multiple cell layer growth analysis approach using Arabidopsis sepals. *Frontiers in Plant Science*. **15**: 1449195. doi:10.3389/fpls.2024.1449195

Yapo BM, Lerouge P, Thibault JF, Ralet MCH. 2007. Pectins from citrus peel cell walls contain homogalacturonans homogenous with respect to molar mass, rhamnogalacturonan I and rhamnogalacturonan II. *Carbohydrate Polymers*. **69**(3): 426-435. doi:10.1016/j.carbpol.2006.12.024

Yu Y, Wu H. 2010. Significant differences in the hydrolysis behavior of amorphous and crystalline portions within microcrystalline cellulose in hot-compressed water. *Industrial & Engineering Chemistry Research.* **8**: 3902-3909. doi:10.1021/ie901925g

Zablackis E, Huang J, Müllerz B, Darvill AC, Albersheim P. 1995. Characterization of the cell-wall polysaccharides of Arabidopsis thaliana leaves. *Plant Physiology.* **107**: 1129-1138. doi:10.1104/pp.107.4.1129

Zeise I, Heiner Z, Holz S, Joester M, Büttner C, Kneipp J. 2018. Raman Imaging of Plant Cell Walls in Sections of *Cucumis sativus*. *Plants.* **7**(1). doi:10.3390/plants7010007

Zeng Y, Yarbrough JM, Mittal A, et al. 2016. In situ label-free imaging of hemicellulose in plant cell walls using stimulated Raman scattering microscopy. *Biotechnology for Biofuels.* **9**: 256. doi:10.1186/s13068-016-0669-9

Zhang H, Chen Z, Li T. et al. 2017. Surface-enhanced Raman scattering spectra revealing the inter-cultivar differences for Chinese ornamental *Flos Chrysanthemum*: a

new promising method for plant taxonomy. *Plant Methods.* **13**(92). doi:10.1186/s13007-017-0242-y

Zhang X, Li L, Xu F. **2023**. Polarized Raman spectroscopy for determining the orientation of cellulose microfibrils in wood cell wall. *Cellulose.* **30**: 75–85. Doi: 10.1007/s10570-022-04915-w

Zhu M, Chen W, Mirabet V. et al. 2020. Robust organ size requires robust timing of initiation orchestrated by focused auxin and cytokinin signalling. *Nature Plants.* **6**: 686–698. doi:10.1038/s41477-020-0666-7

8. SUMMARY

From the beginning of sepal development, the primary plant cell wall on the surface of the abaxial sepal epidermis (i.e. outer periclinal walls of epidermal cells) is the outermost barrier protecting the organ and the flower bud against environmental stresses, pathogens, mechanical damage, and participating in gas exchange. The dynamic remodelling of primary cell walls is essential for their expansion, allowing cells to grow, and for coordination of cell behaviour that is necessary to shape functional organs. While the wall composition has been extensively studied, a comprehensive approach to simultaneously detect all its major components and follow their changes during organ development are limited. In the present study, the primary cell walls on the surface of *Arabidopsis thaliana* sepals were chosen to investigate the primary cell wall composition and cuticular pattern formation in wild type and cell wall mutants during the sepal maturation. Raman microspectroscopy was used in these investigations because it facilitates assessment of overall cell wall composition during single measurements. *In vivo* confocal microscopy imaging of the epidermis surface during sepal maturation provided complementary information about the dynamics of the cell wall structure, with focus on the formation of the cuticular pattern. The objectives of the present investigations were to verify the following hypotheses: (i) Primary cell wall composition of Arabidopsis sepal epidermis changes during the sepal development and is affected by *csi1, mad5, pme32, xyl1* mutations; (ii) Primary cell wall of Arabidopsis sepal epidermis exhibits structural anisotropy resulting from alignment of its components; (iii) Deficiency of a cell wall component in Arabidopsis mutants activates a compensatory mechanism; (iv) The initial pattern of cuticular ridges appearing on the outer periclinal walls of Arabidopsis sepal is influenced by cell growth and geometry at the time of pattern formation; (v) The pattern of cuticular ridges is changing during the cell growth. Raman microspectroscopy measurements revealed ontogenetic changes in primary cell wall composition during maturation of Arabidopsis sepal epidermis, reflected in differences in signal intensity and contribution of two component spectra identified using multivariate curve resolution. These changes indicate compositional remodelling of the cell wall during organ maturation. Raman maps of superficial walls of the sepal enabled to distinguish two regions with assigned specific spectra: one for cell wall located between the cuticular ridges, and another for wall covered by ridges.

These two regions showed slight compositional differences, including additional bands in ridge-covered walls. Moreover, qualitative differences between investigated mutants and wild type were revealed. Polarisation-sensitive bands were identified in the Raman spectra. They are a manifestation of structural anisotropy of the wall. The polarisation-dependent bands were related not only to cellulose but also to the cuticle components. Cellulose was aligned within primary cell walls to the similar extent in wild type and the investigated mutants, except for *mad5*. This *mad5* phenotype is similar to other katanin mutants in which microtubule dynamics is affected. Structural anisotropy of cuticle components of Arabidopsis sepal, similar in the wild type and the investigated mutants, is a novel observation. It suggests that even the thin cuticle of Arabidopsis sepal epidermis exhibits some degree of ordered organisation, although further investigations at higher resolution are needed. Comparison of contribution to the spectra of Raman signals related to pectins, cellulose and hemicellulose facilitated indirect assessment of the relative contribution of three main polysaccharides in individual wall samples of wild type and the investigated mutants. In mutants, a decrease in the signal assigned to one component was accompanied by an increase in others or *vice versa*. This is likely a manifestation of compensatory adjustments mechanism to maintain cell wall structure and mechanical properties despite compositional changes. *In vivo* confocal imaging combined with quantification of sepal surface growth and curvature, showed that cuticular ridges that decorate the abaxial surface of Arabidopsis sepals are formed on an initially smooth outer periclinal walls when the sepal surface is still expanding. The pattern formed by cuticular ridges depends on the anisotropy of the surface expansion and on its geometry. In agreement with models explaining the ridges formation as a mechanical buckling, the orientation of newly formed ridges was most often parallel to the principal direction of maximal growth at both the cellular and subcellular scales. The relation between ridges orientation and directions of surface curvature was much weaker. However, the unique complexity of ridges pattern on the surface of *mad5* sepals seems to be related to the high curvature of mutant epidermal cells. The extent of alignment and morphology of cuticular ridges change during the sepal surface expansion. The anisotropy of the initial ridges patterns either increased or decreased over time. The decrease in anisotropy was often related to the formation of new short ridges that were sometimes perpendicular to the initially formed ones, while the anisotropy increase was associated with the straightening of already existing ridges. The changes in anisotropy of the cuticular pattern during wall expansion are likely a

manifestation of stiffness heterogeneity, i.e. the stiff film formed by cuticle proper is covering the relatively soft cuticular layer, in agreement with models of ridges formation that assume buckling.

9. STRESZCZENIE

Od początku rozwoju kwiatu pierwotne ściany komórkowe, znajdujące się na powierzchni epidermy działek kielicha (zewnętrzne ściany peryklinalne komórek epidermalnych) stanowią najbardziej zewnętrzną barierę chroniącą działki i kwiat przed stresem środowiskowym, patogenami, uszkodzeniami mechanicznymi i uczestniczą w wymianie gazowej. Dynamiczna przebudowa pierwotnych ścian komórkowych jest konieczna do ich ekspansji, umożliwiając wzrost komórek oraz koordynację między komórkami niezbędną do wykształcenia funkcjonalnego organu. Choć skład ściany komórkowej był szeroko badany, kompleksowe podejście pozwalające na jednoczesną analizę wszystkich jej głównych składników oraz śledzenie ich zmian podczas rozwoju organu jest ograniczone. W niniejszej pracy pierwotne ściany komórkowe epidermy działki kielicha *Arabidopsis thaliana* wykorzystano do analizy ich składu. Ponadto badano powstawanie wzoru kutykularnego w typie dzikim oraz u mutantów ściany komórkowej podczas dojrzewania działki kielicha. W badaniach wykorzystano mikrospektroskopię Ramana, która umożliwia ocenę ogólnego składu ściany komórkowej podczas pojedynczego pomiaru. Natomiast mikroskopię konfokalną wykorzystano do przeprowadzenia obserwacji *in vivo* powierzchni komórek epidermy w trakcie dojrzewania działki kielicha. Dzięki temu uzyskano dodatkowe informacje o dynamice ściany komórkowej, ze szczególnym uwzględnieniem powstawania wzoru kutykularnego. Cele badań obejmowały weryfikację następujących hipotez: (i) Skład pierwotnej ściany komórkowej epidermy działki kielicha *Arabidopsis* zmienia się podczas rozwoju działki a mutacje *csi1, mad5, pme32, xyl1* wpływają na zmiany w składzie; (ii) Pierwotna ściana komórkowa epidermy działki kielicha *Arabidopsis* wykazuje anizotropię strukturalną wynikającą z uporządkowania jej składników; (iii) Niedobór jednego składnika ściany komórkowej u mutantów *Arabidopsis* aktywuje mechanizm kompensacyjny; (iv) Początkowy wzór prążków kutykularnych pojawiających się na zewnętrznych ścianach peryklinalnych działki kielicha jest zależny od wzrostu i geometrii komórki w momencie powstawania wzoru; (v) Wzór prążków kutykularnych zmienia się w trakcie wzrostu komórek. Pomiary z wykorzystaniem mikrospektroskopii Ramana wykazały zmiany ontogenetyczne w składzie pierwotnej ściany komórkowej podczas dojrzewania epidermy działki kielicha *Arabidopsis*, przejawiające się różnicami intensywności sygnału i różnicami w udziale dwóch widm

składowych zidentyfikowanych przy użyciu metody rozdzielania krzywych wielowymiarowych. Zmiany te wskazują, że skład ściany komórkowej ulega przebudowie podczas dojrzewania organu. Analiza map Ramanowskich powierzchni ścian działki kielicha pozwoliła wyróżnić dwa regiony z przypisanymi specyficznymi widmami: ścianę komórkową znajdującą się pomiędzy prążkami kutykularnymi oraz ścianę pokrytą prążkami. Widma tych regionów wykazywały niewielkie różnice w składzie, w tym dodatkowe pasma w ścianach pokrytych prążkami. Ponadto ujawniono różnice jakościowe między badanymi mutantami a typem dzikim. W widmach Ramana zidentyfikowano pasma wrażliwe na polaryzację, które wskazują na anizotropię strukturalną ściany. Pasma zależne od polaryzacji były związane nie tylko z celulozą, ale również ze składnikami kutykuli. Celuloza była uporządkowana w pierwotnych ścianach komórkowych w podobnym stopniu zarówno u typu dzikiego, jak i u badanych mutantów, z wyjątkiem *mad5*. Fenotyp *mad5* jest podobny do innych mutantów kataniny, u których zmieniona jest dynamika mikrotubul. Anizotropia strukturalna składników kutykuli działki kielicha *Arabidopsis*, która była podobna w typie dzikim i badanych mutantach, nie była dotychczas opisywana. Sugeruje to, że nawet cienka kutykula epidermy kielicha *Arabidopsis* wykazuje pewien stopień uporządkowania. Dalsze badania o wyższej rozdzielczości są potrzebne, aby wyjaśnić tę cechę struktury kutikuli. Porównanie udziału sygnałów Ramana związanych z pektynami, celulozą i hemicelulozą w widmach ścian typu dzikiego i mutantów pozwoliło pośrednio ocenić względny udział trzech głównych polisacharydów w ścianie. U mutantów spadek sygnału przypisanego jednemu składnikowi był równoważony przez wzrost sygnałów innych składników. Jest to prawdopodobnie przejaw mechanizmu kompensacyjnego utrzymującego strukturę i właściwości mechaniczne ściany komórkowej pomimo zmian w składzie. Obserwacje z wykorzystaniem mikroskopii konfokalnej *in vivo*, połączone z ilościową analizą wzrostu powierzchni i krzywizny działki kielicha, wykazały, że prążki kutykularne dekorujące powierzchnię abaksjalną działki kielicha *Arabidopsis* powstają na początkowo gładkich ścianach peryklinalnych, gdy powierzchnia ścian nadal się powiększa. Wzór prążków kutykularnych zależy od anizotropii wzrostu i krzywizny powierzchni oraz jej geometrii. Zgodnie z modelami wyjaśniającymi formowanie prążków jako wyboczenie mechaniczne, orientacja nowo powstałych prążków była najczęściej równoległa do kierunku maksymalnego wzrostu zarówno na poziomie komórkowym, jak i subkomórkowym. Związek między orientacją prążków a kierunkami krzywizny powierzchni ściany był znacznie słabszy. Jednak unikalna

złożoność wzoru prążków na powierzchni działki kielicha *mad5* wydaje się być związana z dużą krzywizną komórek epidermalnych tego mutanta. Stopień uporządkowania i morfologia prążków kutykularnych zmieniają się podczas ekspansji powierzchni działki kielicha. Anizotropia wzoru prążków wzrastała lub malała w czasie wzrostu powierzchni komórek. Spadek anizotropii często wiązał się z powstawaniem nowych krótkich prążków, czasami prostopadłych do wcześniej utworzonych, natomiast wzrost anizotropii był związany z prostowaniem prążków już istniejących. Zmiany anizotropii wzoru kutykularnego podczas ekspansji ściany są prawdopodobnie przejawem zróżnicowania sztywności kutikuli: stosunkowo sztywny film utworzony przez właściwą kutykulę pokrywa stosunkowo miękką warstwę kutykularną, co jest zgodne z założeniami modeli powstawania prążków opartych na wyboczeniu.

10. SUPPLEMENTARY TABLE

Genotype	Sepal	Shape group	Cell PDGmax	Cell Growth Anisotropy	maxCurvT0 vs Cell PDGmax	maxCurvT24 vs Cell PDGmax	General ridges direction vs Cell PDGmax	General ridges direction vs maxCurvT24	Ridges direction vs local PDGmax	Ridges Waviness	
Col-0	1	1	1.10	1.13	parallel	oblique	parallel	oblique	parallel	++	Cell1
	1	1	1.32	1.36	orthogonal	orthogonal	parallel	orthogonal	parallel	++	
	1	1	1.26	1.25	orthogonal	orthogonal	parallel	orthogonal	parallel	+	
	1	1	1.17	1.07	parallel	parallel	orthogonal	orthogonal	mixed	+	Cell2
	2	1	1.34	1.12	orthogonal	orthogonal	parallel	orthogonal	parallel	+	
	3	1	1.17	1.07	N/A	N/A	parallel	N/A	mixed	++	
	1	2	1.26	1.10	oblique	oblique	oblique	orthogonal	mixed	++	
	1	2	1.27	1.19	parallel	parallel	N/A	N/A	N/A	+++	Cell1
	1	2	1.20	1.12	orthogonal	orthogonal	parallel	orthogonal	parallel	++	
	1	2	1.18	1.45	oblique	oblique	parallel	oblique	parallel	+	
	1	2	1.43	1.50	oblique	oblique	parallel	oblique	parallel	+	
	1	2	1.18	1.45	orthogonal	orthogonal	parallel	orthogonal	mixed	+	
	1	2	1.16	1.17	orthogonal	orthogonal	parallel	orthogonal	mixed	+	Cell2
	2	2	1.28	1.11	orthogonal	orthogonal	orthogonal	parallel	parallel	+	
	3	2	1.23	1.12	parallel	orthogonal	oblique	oblique	mixed	++	
	3	2	1.17	1.13	N/A	N/A	parallel	N/A	mixed	++	
	3	2	1.25	1.17	N/A	N/A	oblique	oblique	mixed	++	
	1	3	1.40	1.14	oblique	oblique	oblique	orthogonal	mixed	+	Cell4
	1	3	1.30	1.12	parallel	oblique	oblique	orthogonal	mixed	+	Cell3
	1	3	1.32	1.42	orthogonal	orthogonal	parallel	orthogonal	mixed	+	Cell1
	1	3	1.21	1.16	orthogonal	orthogonal	parallel	orthogonal	mixed	+	Cell2
	2	3	1.14	1.52	oblique	oblique	oblique	parallel	mixed	++	
	2	3	1.17	1.26	parallel	parallel	parallel	parallel	mixed	+	
	2	3	1.17	1.40	parallel	parallel	oblique	parallel	mixed	+	
	3	3	1.14	1.06	N/A	N/A	N/A	N/A	N/A	+++	

Genotype	Sepal	Shape group	Cell PDGmax	Cell Growth Anisotropy	maxCurvT0 vs Cell PDGmax	maxCurvT24 vs Cell PDGmax	General ridges direction vs Cell PDGmax	General ridges direction vs maxCurvT24	Ridges direction vs local PDGmax	Ridges Waviness	
mad5	1	1	1.16	1.10	N/A	orthogonal	N/A	N/A	N/A	+++	
	1	1	1.16	1.12	oblique	oblique	N/A	N/A	N/A	+++	
	1	1	1.29	1.19	orthogonal	orthogonal	N/A	N/A	mixed	+++	
	1	1	1.18	1.10	parallel	parallel	orthogonal	parallel	parallel	++	
	1	1	1.10	1.05	orthogonal	orthogonal	orthogonal	parallel	mixed	++	
	1	1	1.08	1.41	N/A	parallel	parallel	parallel	parallel	++	
	1	1	1.19	1.32	parallel	parallel	parallel	parallel	mixed	++	
	2	1	1.28	1.14	oblique	oblique	N/A	N/A	N.A	+++	
	2	1	1.32	1.31	oblique	parallel	oblique	parallel	oblique	++	
	2	1	1.23	1.06	oblique	parallel	parallel	parallel	parallel	++	
	2	1	1.27	1.36	orthogonal	orthogonal	parallel	orthogonal	parallel	++	
	3	1	1.30	1.05	parallel	N/A	N/A	N/A	N/A	+++	Cell1
	3	1	1.34	1.41	parallel	N/A	N/A	N/A	N/A	+++	
	3	1	1.10	1.16	oblique	N/A	N/A	N/A	N/A	+++	
	3	1	1.53	1.39	oblique	N/A	parallel	N/A	mixed	++	
	3	1	1.34	1.30	parallel	N/A	oblique	N/A	mixed	+	Cell2
	3	1	1.40	1.25	oblique	oblique	N/A	N/A	N/A	+++	
	3	1	1.36	1.18	orthogonal	orthogonal	parallel	orthogonal	mixed	++	
	1	2	1.11	1.07	parallel	orthogonal	parallel	orthogonal	parallel	++	
	1	2	1.17	1.07	orthogonal	orthogonal	oblique	orthogonal	mixed	++	
	1	2	1.14	1.07	orthogonal	orthogonal	oblique	oblique	mixed	++	
	2	2	1.21	1.03	N/A	N/A	N/A*	N/A	N/A	+++	
	2	2	1.37	1.35	oblique	oblique	N/A	N/A	N/A	+++	
	2	2	1.31	1.31	oblique	oblique	N/A	N/A	N/A	+++	
	3	2	1.46	1.42	oblique	parallel	parallel	parallel	mixed	++	Cell3
	3	2	1.46	1.42	parallel	parallel	oblique	oblique	mixed	++	Cell1
	3	2	1.37	1.29	oblique	N/A	N/A	N/A	N/A	+++	Cell2
	3	2	1.44	1.22	N/A	N/A	oblique	N/A	mixed	+	Cell4
	1	3	1.10	1.07	parallel	parallel	N/A	N/A	N/A	+++	
	3	3	1.26	1.12	oblique	orthogonal	N/A	N/A	mixed	+++	Cell1
	3	3	1.24	1.04	oblique	oblique	N/A	N/A	N/A	+++	Cell2

Supplementary Table 1 Growth, curvature, ridges parameters and their relations for individual cells. Cells shown in **Figs. 4.21-26** are highlighted in blue, their numbers given in the last column.